



VCU

Virginia Commonwealth University
VCU Scholars Compass

Theses and Dissertations

Graduate School

2018

MECHANISMS REGULATING AXON INITIAL SEGMENT STABILITY

Savannah D. Benusa
Virginia Commonwealth University

Follow this and additional works at: <https://scholarscompass.vcu.edu/etd>



Part of the [Molecular and Cellular Neuroscience Commons](#)

© The Author

Downloaded from

<https://scholarscompass.vcu.edu/etd/5357>

This Dissertation is brought to you for free and open access by the Graduate School at VCU Scholars Compass. It has been accepted for inclusion in Theses and Dissertations by an authorized administrator of VCU Scholars Compass. For more information, please contact libcompass@vcu.edu.

MECHANISMS REGULATING AXON INITIAL SEGMENT STABILITY

A dissertation submitted in partial fulfillment of the requirements for the degree of
Doctor of Philosophy at Virginia Commonwealth University.

by

Savannah Denise Benusa

Bachelor of Science

Texas A & M University – Commerce

May 2012

Director: Jeffrey L. Dupree, Ph.D.

Associate Professor

Department of Anatomy and Neurobiology

Virginia Commonwealth University

Richmond, Virginia

April 2018

ACKNOWLEDGEMENTS

I would first like to thank my mentor, Dr. Jeffrey Dupree, for his invaluable guidance and support. Jeff was, without fail, available to troubleshoot projects, discuss new ideas, and provide unending optimism through the many challenges of science. Thank you for pushing me to be a better scientist, to think more critically, and for giving me the confidence to step outside of my comfort zone. Also, thank you for the incredible support you provided this past year as I welcomed my twin daughters; this experience is not without challenges and I am grateful beyond words.

I would like to acknowledge the faculty members of my committee Dr. Babette Fuss, Dr. Kurt Hauser, Dr. Unsong Oh, and Dr. George DeVries for providing direction and feedback for my projects and collaboratively improving the quality of my science. A special thanks to Dr. Babette Fuss and her lab members for their willingness to help me through the challenges of my neurofascin project. Thank you for lending materials and reagents, for assistance in PCR techniques and DNA sequencing, and for guidance in my knockout animal studies. I would also like to acknowledge Frances White from the microscopy facility and Julie Farnsworth from the flow facility. Moreover, I would like to extend my sincere gratitude to the Neuroscience program director, Dr. John Bigbee, for his continuous support and encouragement through all facets of my graduate career. Dr. Bigbee is genuinely invested in the success of students and I truly felt that along the way.

I would like to acknowledge my fellow graduate students and lab mates. A special thanks to Jessie Yester, Logan Meyer, Kareem Clark, Natalie Wheeler, and Patrick MacKnight for your life-long friendships, shared knowledge, and for being pillars of strength. Thanks also to Sarah Izabel for her help with tissue sectioning, Nicholas George for his help in generating the automated method for AIS quantitation and assistance in the analysis of microglial contact, to Matthew Baer for his expertise in statistics, and to Brooke Sword for her care of our research animals.

To my friends and family, thank you from the bottom of my heart for your unconditional love and support. Thank you especially to my mother for teaching me that, with hard work and a positive attitude, you can conquer anything. Thank you always for championing me and being my biggest fan. To my husband, Kyle, and daughters, Willa and Ellis, thank you for making Richmond my home, for making each day brighter, and for inspiring me to be the best version of myself.

TABLE OF CONTENTS

	Page
List of Figures.....	iv
List of Tables.....	vii
List of Abbreviations.....	viii
Abstract.....	ix
Chapter 1 Introduction.....	1
Chapter 2 Acute Neuroinflammation Induces AIS Structural Plasticity in a NOX2- Dependent Manner.....	20
Chapter 3 Novel Expression of Neurofascin in Microglia: A Candidate for Microglia- AIS Interaction.....	99
Chapter 4 Discussion.....	156
List of References.....	165
Vita.....	187

LIST OF FIGURES

	Page
1.1 Schematic of Neuronal domain organization.....	4
1.2 Schematic of Neurofascin domain organization.....	18
2.1 LPS-induced Inflammation Disrupts AISs.....	55
2.2 LPS-induced Inflammation Disrupts AIS Nav1.6 Functional Sub-domains.....	57
2.3 LPS-induced Inflammation Disrupts AIS Kv1.2 Functional Sub-domains.....	59
2.4 LPS-induced Inflammation Disrupts AIS Functional Sub-domains.....	61
2.5 Microglial-AIS contact does not coincide with AIS disruption in LPS-injected mice.....	63
2.6 AIS Integrity Coincides with Microglial Reactivity.....	65
2.7 AIS Integrity Coincides with Microglial Inflammatory Response	67
2.8 Treatment with Didox Reverses AIS Disruption.....	69
2.9 Treatment with Didox Reverses AIS Distal Shortening.....	71
2.10 Treatment with Didox Alters Microglial NOX2 Levels	73
2.11 Ablation of NOX2 Prevents AIS Disruption.....	75
2.12 Treatment with Calpain Inhibitor Prevents AIS Disruption.....	77
S2.1 Automated AIS Counts Using FIJI is an Accurate Method for Quantifying AISs.....	89

S2.2	Heat map of Differentially Expressed Genes in Microglia of LPS-Injected Mice.....	91
S2.3	AISs Spontaneously Recovered 2wks post-LPS Injection	93
S2.4	NOX2–Deficient Mice Mount a Pro-Inflammatory Response after LPS Injection.....	95
S2.5	LPS 10mg/kg Injection does not Result in Sustained Disruption of AISs 2wks Post-injection.....	97
3.1	Microglial Nfasc Clusters at the Microglia-AIS Interface.....	130
3.2	Microglial Nfasc is up-regulated in EAE	132
3.3	Microglia Express Nfasc mRNA, Contain Nfasc Binding domains Ig 5 and 6, and Generation of Microglia-specific <i>Nfasc</i> null Mice Confirms Presence of Microglial Nfasc Gene Product.....	134
3.4	Microglial Nfasc Maintains Conserved FNIII and Cytoplasmic Domains and Excludes the Alternatively Spliced mucin and 5th FNIII Repeat.....	136
3.5	PCR Amplification and Sequencing Reveals Microglial Nfasc Transcript is Unique from Nfasc 186 and Nfasc 155.....	138
3.6	Proposed Domain Composition of Microglial Nfasc.....	140
3.7	RT-qPCR Analysis using Microglial <i>Nfasc</i> null Mice Confirms that Microglial Nfasc has the Conserved Cytoplasmic and 1st FNIII Repeat and the Alternatively Spliced 3rd FNIII Repeat.....	142

3.8	Protein levels are not reduced 45 days post-4-HT induction in <i>CX3CR1^{creER+/-}</i> <i>/Nfasc^{f/f}</i> mice	144
S3.1	Sequence Alignment of Translated Nucleotide Sequence of Microglial Nfasc with Published Sequences from NCBI.....	148
S3.2	Microglia are Distinguished from Macrophages and Isolated by FACS.....	152
S3.3	Isolated Microglia are Enriched for Microglial Markers but not Oligodendrocyte or Neuronal Markers.....	154

LIST OF TABLES

	Page
2.1 Neuronal Density and Cortical Volume Measurements from Saline and LPS- Injected Mice.....	79
2.2 Oligonucleotide Primer Pairs Used for RT-qPCR.....	80
2.3 AnkG Start and End positions and Length Measurements.....	81
2.4 Nav1.6 Start and End positions and Length Measurements.....	82
2.5 Kv1.2 Start and End positions and Length Measurements.....	83
2.6 Functional Clustering of Genes Up-regulated: LPS 6h vs. Saline.....	84
2.7 Functional Clustering of Genes Down-regulated: LPS 6h vs. Sal.....	85
2.8 Functional Clustering of Genes Up-regulated: LPS 1wk vs. Sal.....	86
2.9 Functional Clustering of Genes Down-regulated: LPS 1wk vs. LPS 6h.....	87
2.10 Functional Clustering of Genes Up-regulated: LPS 1wk vs. LPS 6h.....	88
3.1 Oligonucleotide Primer Pairs Used for RT-qPCR and end-point PCR.....	146

LIST OF ABBREVIATIONS

AD	Alzheimer's disease	Hprt	Hypoxanthine Phosphoribosyltransferase
AP	Action Potential		
AIS	Axon Initial Segment	Iba-1	Ionized Ca ²⁺ -Binding Adapter molecule 1
AnkG	Ankyrin G	Ig	Immunoglobulin
BLAST	Basic Local Alignment Search Tool	IL	Interleukin
CAM	Cell Adhesion Molecule	iNOS	Inducible Nitric Oxide Synthase
CamKII	Calcium/calmodulin-dependent protein Kinase type II	K _v	Voltage-gated Potassium
Caspr-2	Contactin Associated Protein-2	LPS	Lipopolysaccharide
CNP	Cyclic Nucleotide Phosphodiesterase	MOG	Myelin Oligodendrocyte Glycoprotein
CNS	Central Nervous System	Mrc1	Mannose Receptor, C type 1
CSF1r	Colony Stimulating Factor 1 Receptor	mRNA	Messenger Ribonucleic Acid
COX-2	Cyclooxygenase-2	MS	Multiple Sclerosis
CX3CR1	Chemokine Fractalkine Receptor	Na _v	Voltage-Gated Sodium
EAE	Experimental Autoimmune Encephalomyelitis	NeuN	Neuronal Nuclei
ECM	Extracellular Matrix	Nfasc	Neurofascin
FACS	Fluorescence activated cell sorting	NF- κB	Nuclear Factor Kappa-light-chain- Enhancer of Activated B cells
FGFR1	Fibroblast Growth Factor Receptor1	NOX2	Nicotinamide Adenine Dinucleotide Phosphate Oxidase 2
Fizz-1	Resistin like beta	NO	Nitric Oxide
FNIII	Fibronectin type III	Pgk1	Phosphoglycerate Kinase 1
GABA	Gamma-Aminobutyric Acid	RbFox3	RNA binding Fox-1 homolog 3
GAPDH	Glyceraldehyde-3-Phosphate Dehydrogenase	ROS	Reactive Oxygen Species
GO-BP	Gene Ontology-Biological Process	TBI	Traumatic Brain Injury
Gusb	Glucuronidase Beta	TGF-β	Transforming Growth Factor beta
4-HT	4-Hydroxytamoxifen	Tnfa	Tumor Necrosis Factor alpha
		TRPM	Transient Receptor Potential <i>M</i>
		Tubb5	Tubulin Beta Class 5

ABSTRACT

MECHANISMS REGULATING AXON INITIAL SEGMENT STABILITY

By Savannah Benusa, B.S.

A dissertation submitted in partial fulfillment of the requirements for the degree of Doctor of Philosophy at Virginia Commonwealth University.

Virginia Commonwealth University, 2018

Director: Jeffrey L. Dupree, Ph.D.
Associate Professor
Department of Anatomy and Neurobiology

Axon initial segment (AIS) disruption has been described in a number of pathological environments where neuroinflammation is a contributing factor; however, whether this disruption is reversible remains to be determined. To address the principle of AIS structural recovery, we employed an acute neuroinflammatory model induced by peripheral stimulation. Acute neuroinflammation induced disruption of AIS structural and functional domains and, importantly, upon resolution of neuroinflammatory conditions, AIS disruption was reversed. This work provides the first in vivo evidence the AIS disruption is reversible following a neuroinflammatory event.

Consistent with other studies, we observed a close interaction of microglia with AISs, and utilized this acute neuroinflammatory model to investigate the relationship between reactive microglia and AIS integrity. Gene expression analysis of the microglial inflammatory transcription profile identified reactive oxygen species (ROS)-producing enzymes as candidates in AIS pathogenesis. Therapeutic intervention, utilizing a free-radical scavenger, and experiments employing mice lacking the major ROS-producing

enzyme NOX2, identified ROS as mediators of AIS disruption. Furthermore, we established calcium-dependent protease calpain as a disruptor of AIS protein clustering in inflammation-induced disruption.

Since we observed an intimate interaction between reactive microglia and the AIS, we next conducted studies designed to identify a novel candidate in microglia that may regulate microglial-AIS contact. During chronic inflammatory conditions, microglia enhance their contact with AISs often completely surrounding the domain. This contact is distinct from the process alignment and process touching exhibited by surveying microglia suggesting that a more elaborate type of interaction occurs during neuroinflammation. Concomitant with this morphological change, neurofascin (Nfasc) expression increased in microglia. Nfasc is a cell adhesion molecule with cell-specific isoforms known to mediate glial-neuronal interactions, but until now, was not reported to be expressed by microglia. Here, I characterize the unique Nfasc isoform expressed by microglia and present evidence that suggests that microglial Nfasc may mediate microglial-AIS contact, a potentially pivotal interaction in the induction of AIS disruption by pro-inflammatory factors.

CHAPTER ONE

INTRODUCTION

1.1 Cells of the Central Nervous System

The establishment, maintenance, and function of the central nervous system (CNS) is dependent on the bi-directional communication between neurons and supporting glia. Neurons are highly specialized cells of the nervous system that receive, process, and transmit electrical signals. Neurons are organized and connected into functional circuits by axons that conduct action potentials (AP), allowing for the transmission of information throughout the nervous system. Signaling among neurons is influenced and regulated by the surrounding glial cells, which in the CNS can be primarily classified into 3 cell types: astrocytes, oligodendrocytes and microglia (for review see (von Bernhardi et al., 2016a). Glial cells facilitate numerous functions in the CNS including establishment of CNS architecture, brain metabolism, neuronal survival, development and modulation of synaptic transmission, and propagation of nerve impulses (von Bernhardi et al., 2016a).

Briefly, astrocytes regulate synaptic transmission and neuronal signaling by contacting synaptic elements present between communicating neurons (Vesce et al., 1999, Newman2003; Croftetal.2015; Gittis and Brasier 2015). At neuronal synapses, astrocytes remove or release ions, neurotransmitters, and metabolic factors (Pellerin et al., 2007; Santello et al., 2012; Schousboe et al., 2014; Wallraff et al., 2006). Astrocytes also contribute to the maintenance of blood–brain barrier integrity by forming a secondary barrier that further restricts the entry of peripheral immune cells into the CNS (Giannoni et al., 2018). Additionally, astrocytes extend processes to both neurons and local blood

vessels to coordinate neuronal activity and metabolic demands with local blood flow (Giannoni et al., 2018; Pellerin et al., 2007; Takano et al., 2006; Zonta et al., 2003).

Oligodendrocytes also form direct contacts with the neuron; however, these cells regulate speed and efficiency of neuronal signal propagation. Oligodendrocytes extend processes that surround axons forming a lipid-rich myelin sheath, which insulates axons facilitating nerve conduction (Bercury and Macklin, 2015; von Bernhardi et al., 2016a; Xu and Terakawa, 1999). Oligodendrocytes also signal to neurons to provide trophic support, affect axon structure, and influence axonal ion channel clustering (Frühbeis et al., 2013; Krämer-Albers et al., 2007; Lappe-Siefke et al., 2003; Lee et al., 2012; Rasband and Peles, 2015; Rasband et al., 2005; Wilkins et al., 2003). Importantly, communication is not one-way since myelin production is regulated by neuronal activity (Gibson et al., 2014; Hines et al., 2015; Mensch et al., 2015; Mitew et al., 2018). Thus, oligodendrocytes and neurons are active partners in the propagation of information.

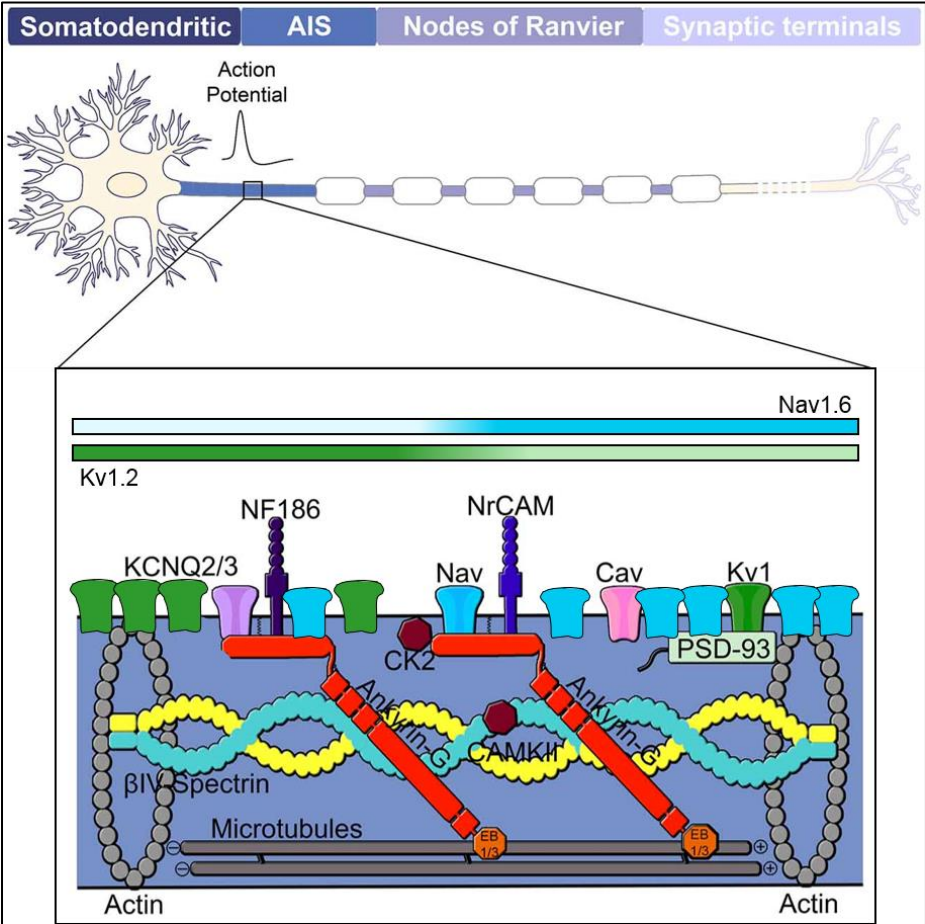
Microglia are the resident macrophages of the CNS and mediate immune-related functions. Microglia are highly mobile cells that rapidly extend and retract their processes to survey the environment (Nimmerjahn et al., 2005; Sierra et al., 2015; Wake et al., 2009). Upon detection of a change, microglia undergo a complex series of alterations including changes in expression of enzymes, receptors, and immune factors as well as altered morphology, and migration (von Bernhardi et al., 2016b; Wolf et al., 2017). Microglia facilitate the clearance of pathogens or cellular debris, synaptic removal in development and disease, phagocytosis of apoptotic and necrotic cells, inflammation, and tissue repair (von Bernhardi et al., 2016b; Block et al., 2007; Schafer and Stevens, 2013; Trapp et al., 2007; Wolf et al., 2017). Recently, studies have identified direct interactions

between microglia and neurons suggesting that microglia play a role in modulating neural activity as well (Baalman et al., 2013; Clark et al., 2016; Kato et al., 2016; Li et al., 2012; Schafer and Stevens, 2013; Zhan et al., 2014). The crosstalk between neurons and glia is critical for maintenance of CNS homeostasis and CNS function, and disruptions in the interactions between these cells is implicated in the development and progression of numerous CNS diseases (von Bernhardi et al., 2016a; Domingues et al., 2016; Salter and Stevens, 2017).

1.2 Neuronal Signaling: The Axon and its Excitable Domains

Neurons are divided into distinct structural and functional domains including the dendrites and soma, axon, and nerve terminal (Figure 1.1). The dendrites and soma receive signals from upstream synaptic inputs and transmit this information to the axon. If the summation of synaptic inputs is sufficient, an action potential is generated at the axon initial segment (AIS) (Kole and Stuart, 2012a). The action potential is then propagated down the axon to the axon terminal where neurotransmitters are released to propagate the signal across the synaptic cleft to the next cell. Many vertebrate axons are myelinated and further subdivided into excitable domains that include the nodes of Ranvier, myelin deficient regions of the axon that regenerate and propagate action potentials in a saltatory fashion along the axon (Nelson and Jenkins, 2017; Rasband, 2010; Yamada and Kuba, 2016). It is the directional propagation of action potentials among neurons that is critical for the transmission of information throughout neuronal circuitry.

Figure 1.1



(Modified from (Nelson and Jenkins, 2017))

Figure 1.1. Neuronal Domain Organization. The neuron is comprised of a somatodendritic domain, the axon initial segment (AIS), nodes of Ranvier, and the axon terminal. Action potentials are generated at the AIS and propagated down the myelinated axon to the pre-synaptic terminals by the nodes of Ranvier. AnkyrinG (red) controls the establishment and localization of membrane-associated proteins including cell adhesion molecules Nfasc 186 and NrCAM and voltage-gated sodium (Na_v) and potassium (K_v) channels. $\text{Na}_v1.6$ and $\text{K}_v1.2$ channels are clustered at the distal and proximal AIS, respectively, of cortical pyramidal neurons.

1.2.1 *Nodes of Ranvier*

Myelination divides the axon into distinct domains including nodes of Ranvier, paranodes, juxtaparanodes and internodes (Rasband and Peles, 2015). The nodes of Ranvier are located between adjacent myelin sheaths, and are characterized by a dense clustering of voltage-gated ion channels, cell adhesion molecules, and scaffolding proteins (Rasband and Peles, 2015). The high density of voltage gated sodium (Na_v) channels allows for action potential regeneration, while voltage gated potassium (K_v) channels are responsible for membrane repolarization (Nelson and Jenkins, 2017). Voltage-gated ion channels and cell adhesion molecules such as neurofascin (Nfasc) 186 and neural cell adhesion molecule (NrCAM) are anchored to the underlying cytoskeleton by ankyrinG (ankG) and β IV-spectrin scaffolding proteins (Gasser et al., 2012; Susuki et al., 2013). Located on either side of the node of Ranvier is the region of the myelin sheath that maintains the closest apposition to the axon. This region, known as the paranode, is the site where myelinating glia form septate-like junctions, between the terminal loops of myelin and the axonal membrane, that tether the myelin sheath to the axon (Banerjee et al., 2006). The paranodal complex is formed through binding of the glial cell adhesion molecule Nfasc 155 with the axonal contactin/Caspr (contactin-associated protein) heterodimer (Banerjee et al., 2006; Charles et al., 2002; Tait et al., 2000). The paranodal complex segregates the densely clustered Na_v channels at the node from the densely clustered K_v channels present in the adjacent juxtaparanodes. Finally, the internodes are the portions of the axon beneath the compacted myelin sheath that spans between juxtaparanodal regions. The internodal region constitutes the majority of the myelinated axon.

1.2.2 *The Axon Initial Segment*

In addition to the four domains that are created based on myelin deposition, all axons, whether myelinated or not, also contain the functional domain known as the axon initial segment (AIS). As implied by the name, the AIS spans the initial segment of the axon immediately adjacent to the neuronal soma. It functions in action potential initiation and modulation (Buffington and Rasband, 2011; Goldberg et al., 2008; Kole et al., 2007, 2008; Ogawa and Rasband, 2008), and is critical for maintaining neuronal polarity by providing a barrier for the diffusion or transport of lipids, cytoplasmic and membrane proteins, and transport vesicles to distinct compartments of the neuron (Kobayashi et al., 1992; Nakada et al., 2003; Rasband, 2010; Song et al., 2009). Similar to the nodes of Ranvier, the AIS is composed of a dense clustering of voltage-gated ion channels, cell adhesion molecules, and scaffolding proteins including ankG and β IV-spectrin (Ogawa and Rasband, 2008). However, unlike the nodes of Ranvier, the AIS is established mainly through intrinsic mechanisms regulated by ankG (Ogawa and Rasband, 2008). AIS proteins are recruited to and maintained at the AIS via the cytoskeletal linking protein ankG (Bennett and Baines, 2001; Jenkins and Bennett, 2002; Leterrier et al., 2015). Genetic deletion of ankG prevented clustering of other AIS proteins and disrupted neuronal polarity (Hedstrom et al., 2008; Jenkins and Bennett, 2001; Pan et al., 2006; Zhou et al., 1998). Furthermore, silencing of ankG using short hairpin RNA disrupted AIS protein clustering, axonal identity, and, consequently, neuronal function (Hedstrom et al., 2008; Zhou et al., 1998). Similar consequences have been observed in pathological conditions where loss of ankG was detected (Buffington and Rasband, 2011; Harty et al.,

2013; Vascak et al., 2017). These studies underscore the importance of ankG in regulating AIS assembly and maintenance.

1.2.3 AIS Functional subdomains

AIS proteins are recruited to the AIS via an ankG-dependent mechanism; however, the distribution of some AIS proteins does not parallel ankG distribution and is not ubiquitous throughout the domain (Clark et al., 2009). Instead, some proteins, such as Nav and Kv channel subtypes, exhibit segregated expression forming functional subdomains within the AIS. Numerous ion channels and ion channel subtypes have been identified at the AIS and the expression of these can be cell-type and region specific (Clark et al., 2009; Yamada and Kuba, 2016). I have focused my studies on pyramidal neurons in the somatosensory cortex. In these neurons, a differential clustering of Nav channel subtypes in the proximal or the distal region of the AIS underlies two distinct functions of the AIS: spike initiation and action potential back-propagation (Hu et al., 2009). Nav1.6 sodium channels are the major ion channel subtype present in AISs and are densely clustered in the distal portion of the AIS (Van Wart et al., 2007; Hu et al., 2009, Kole et al., 2008; Colbert and Pan, 2002). It is the high density of low-threshold Nav1.6 channels in the distal portion of the domain that determines the lowest threshold for spike initiation defining this region as the “trigger zone” (Baranauskas et al., 2013; Hu et al., 2009; Kole et al., 2008; Palmer and Stuart, 2006). On the other hand, Nav1.2 sodium channels are high-threshold channels and their clustering in the proximal AIS controls action potential back-propagation, an important component for synaptic scaling and long-term potentiation (Clark et al., 2009; Hu et al., 2009; Yamada and Kuba, 2016;

Yin et al., 2017). K_v1.2 potassium channels have low activation thresholds and produce the repolarization phase of action potentials, controlling action potential half-width and neuron firing frequency (Clark et al., 2009; Kole et al., 2007; Shu et al., 2007). The segregation and distribution of AIS ion channel sub-domains regulates action potential initiation and modulation, key functions of the AIS. Thus, a change in the length or distribution of AIS functional subdomains alters biophysical properties of the AIS and consequently, neuronal function.

1.3 AIS Plasticity

Within the last ten years, studies have shown that the AIS is a dynamic domain capable of undergoing structural and functional changes in response to alterations in the neuronal environment. These changes allow for the modulation of action potentials and, thus, fine-tuning of excitability in response to altered neuronal input, a process known as AIS plasticity. Types of AIS plasticity include alterations in AIS length (Evans et al., 2015; Kuba et al., 2010; Kuba Hiroshi and Ohmori Harunori, 2009), AIS relocation (Evans et al., 2013; Grubb and Burrone, 2010; Harty et al., 2013; Kuba et al., 2014), and changes in ion channel expression and activity (Bender et al., 2010; Benned-Jensen et al., 2016; Del Puerto et al., 2015; Kuba et al., 2010; Yin et al., 2017).

Kuba and colleagues (Kuba et al., 2006, 2010, 2014; Kuba Hiroshi and Ohmori Harunori, 2009) utilized avian auditory neurons to demonstrate activity-dependent AIS plasticity. In nucleus laminaris neurons, AISs exhibited a universal lengthening at the onset of hearing. However, at embryonic day (E) 15, the activity in the auditory nerve

triggered a differential retraction of AISs, such that neurons responding to high sound frequencies had a shorter, more distal AIS and neurons responding to lower frequencies had a longer, more proximal AIS (Kuba et al., 2014; Kuba Hiroshi and Ohmori Harunori, 2009). Similarly, an activity-dependent change in AIS structure was observed in the visual cortex where AISs shortened upon opening of the eyes (Gutzmann et al., 2014).

Activity-dependent AIS plasticity is not restricted to development but also occurs through sensory deprivation or excitotoxic environments. When auditory neurons were deprived of input by removal of the cochlea, the AIS length increased significantly and K^+ channel expression was altered (Kuba et al., 2010). After 1 week, $Kv1.1$ channels were replaced by slow-activating $Kv7.2$ channels (Kuba et al., 2015a). The increased length and switch in ion channel expression corresponded with increased neuronal excitability, a homeostatic response to lack of activity (Kuba et al., 2010). Utilizing dissociated neurons in culture, it was demonstrated that excitotoxic environments (Evans et al., 2013; Grubb and Burrone, 2010) or prolonged depolarization (Evans et al., 2015; Muir and Kittler, 2014) induced AIS relocation or shortening through increased intracellular Ca^{2+} concentrations mediated through activation of L-type (Clark et al., 2017; Evans et al., 2015) and T-type Ca^{2+} channels (Grubb and Burrone, 2010), or calcium-permeable P2X7 receptors (Del Puerto et al., 2015). Calcium-regulated proteins have been implicated in AIS structural changes including calpain (Bened-Jensen et al., 2016; Clark et al., 2017; Del Puerto et al., 2015; Schafer et al., 2009), calcium/calmodulin-dependent protein kinase type II (CamKII) (Evans et al., 2013), and calcineurin (Evans et al., 2013, 2015) suggesting changes in intracellular calcium concentrations is a converging factor in AIS plasticity.

AIS structural alterations also occur in neuropathological environments. Initial studies using a stroke model, reported irreversible proteolysis of AIS structural proteins after oxygen/glucose deprivation (Schafer et al., 2009). Since then, numerous studies have investigated the vulnerability of the AIS in CNS disease. Our laboratory demonstrated that AIS clustering of ankG is progressively disrupted with disease severity in experimental autoimmune encephalomyelitis (EAE), a mouse model of multiple sclerosis (MS) (Clark et al., 2016). Furthermore, AIS ankG and Nav1.6 sub-domains were disrupted in post-mortem human tissue from MS patients (Lubetzki and Davenne, personal communication), which also presented with disrupted synaptic input and cisternae organelle structure (Clark and Dupree, unpublished data), an organelle restricted to the AIS.

In models of traumatic brain injury (TBI), modest AIS shortening was reported; however, this corresponded with significant behavioral (Baalman et al., 2013) and functional (Vascak et al., 2017) impairments. In a model of Alzheimer's disease (AD), amyloid-beta plaques significantly decreased AIS density and AIS length within and surrounding amyloid-beta plaques (Marin et al., 2016). Furthermore, loss of AIS proteins ankG and β IV-spectrin was observed in human AD brains (Sohn et al., 2016). In aged marmoset monkeys, AISs were significantly shortened concomitant with a loss of GABAergic synapses (Atapour and Rosa, 2017). Alterations in AIS structure has been observed in a number of pathological conditions implicating the AIS as a potential therapeutic target; however, initial characterization of AIS pathology suggested that loss or disruption of AIS protein clustering was irreversible (Schafer et al., 2009). Since then, reversibility of AIS changes in length and location *in vitro* have been demonstrated (Evans

et al., 2015; Grubb and Burrone, 2010), and decreased AIS length was reversed in EAE after therapeutic intervention with an anti-inflammatory compound (Clark et al., 2016). However, reversal of AIS ankG loss *in vivo* has not been demonstrated, though a study investigating AIS stability after stroke reported axon-sprouting in the peri-infarct area suggesting the AIS has reparative potential (Hinman et al., 2013).

1.4 Neuroinflammation

A common factor in the disease pathogenesis where AIS disruption occurs is neuroinflammation. Neuroinflammation is inflammation within the brain or spinal cord and is a means by which signals are communicated to or within the CNS (DiSabato et al., 2016). Neuroinflammation is mediated by the production of chemokines and cytokines as well as reactive oxygen species (ROS) and nitric oxide (NO) (Cherry et al., 2014). These mediators are produced by resident CNS glia, endothelial cells, and peripherally derived immune cells (DiSabato et al., 2016). Sustained activation of inflammatory cascades or aberrant production of inflammatory factors can lead to recruitment of peripheral immune cells, edema, tissue damage, and potentially neuronal death. Inflammation-induced neuronal damage is implicated in a number of neuropathological conditions including MS, AD, TBI, stroke, and aging (von Bernhardi et al., 2016a; Crotti and Ransohoff, 2016a; DiSabato et al., 2016; Ransohoff and Khoury, 2016)

1.5 Microglia Mediate Neuroinflammation and Regulate Neuronal Stability

Microglia, the resident immune cells of the CNS, are important mediators of the neuroinflammatory response. Microglia function in immune surveillance, synaptic pruning, axon guidance, and regulation of neuronal activity (Kato et al., 2016; Klupal et al., 2016; Li et al., 2012; Schafer and Stevens, 2013; Schafer et al., 2012; Squarzoni et al., 2014; Stellwagen and Malenka, 2006; Tremblay et al., 2011). Microglia exhibit a variety of morphologies ranging from small cell bodies with long highly-branched processes to enlarged cell bodies with short, thick processes, reminiscent of the characteristic amoeboid macrophage morphology (Wolf et al., 2017). The spectrum of microglial morphologies is indicative of their numerous functions. For example, surveying microglia exhibit long, highly-branched processes that rapidly extend and sample the surrounding environment; however, upon activation, microglia retract their processes and increase cell body size, exhibiting a morphology consistent with phagocytosis or migration (Tay et al., 2017; Wolf et al., 2017).

Following injury or disease, microglia are rapidly recruited to sites of damage where they phagocytose debris and dying cells. Additionally, activated microglia exhibit extensive changes in the expression of their inflammatory profile (Crotti and Ransohoff, 2016a). While some of these secreted factors may provide neurotrophic functions, pro-inflammatory factors exhibit deleterious effects (Chen et al., 2016; Ransohoff and Khoury, 2016). For example, pro-inflammatory microglia up-regulate enzymes that produce reactive oxygen species (ROS) (Chen et al., 2016). Activation of microglial nicotinamide adenine dinucleotide phosphate (NADPH) oxidase (NOX2) results in the extracellular production of ROS (Kumar et al., 2016). ROS alters the function of calcium-permeable

ion channels (Hool, 2008; Hool and Arthur, 2002; Hudasek et al., 2004) and, consequently, alters intracellular calcium levels (Hudasek et al., 2004; Mossakowski et al., 2015), which have been implicated in AIS disruption (Bened-Jensen et al., 2016; Clark et al., 2017; Del Puerto et al., 2015; Evans et al., 2013; Schafer et al., 2009).

In addition to regulating neuronal function through secreted factors, microglia also regulate neurons through physical contact (von Bernhardi et al., 2016b; Bilimoria and Stevens, 2015; Kato et al., 2016; Li et al., 2012; Nimmerjahn et al., 2005; Wake et al., 2009). In the developing and adult brain, microglia contact pre- and postsynaptic neuronal elements in an activity-dependent manner, and synapses that are contacted more frequently are subsequently removed (Schafer et al., 2012; Tremblay et al., 2010; Wake et al., 2009). In pathological conditions, microglia participate in synaptic stripping altering the neuronal excitatory/inhibitory balance (Kettenmann et al., 2013). Microglia also preferentially contact cell bodies and axons of highly active neurons decreasing neuronal activity and preventing excitotoxic cell death (Kato et al., 2016; Li et al., 2012). These studies underscore the importance of microglial contact in the regulation of neural signaling.

1.6 Cell Adhesion Molecule Nfasc Regulates Glial-Neuronal Interactions

Recently, it was found that microglia may also regulate neuronal function through contact at the AIS. Baalman et al. (2015) provided convincing evidence that microglia establish contact with the AIS early in development and maintain this contact through adulthood strongly suggesting that microglia play a role in regulating AIS structure and

function. In addition, findings from our laboratory have shown that microglia also contact the AIS and the extent of contact is enhanced in chronic inflammatory environments (Clark et al., 2016). However, the nature of microglial-AIS interactions and the molecules that mediate it remain undefined.

A molecule that is known to mediate glial-axonal interactions is the cell adhesion molecule neurofascin (Nfasc). Nfasc is a member of the L1 family of CAMs, a subgroup in the immunoglobulin (Ig) superfamily. The L1 family of CAMs is comprised of transmembrane glycoproteins that mediate cell-cell adhesion through homo- or heterophilic binding at the cell surface (Hortsch et al., 2014). Nfasc isoforms are implicated in a wide spectrum of functions including process extension and outgrowth, stability of axonal domains, stability of GABAergic AIS input, and axo-glial contact (Ango et al., 2004; Charles et al., 2002; Pillai et al., 2009; Pruss et al., 2004; Rathjen et al., 1987; Sherman et al., 2005; Tait et al., 2000; Zhang et al., 2015). Nfasc has also been implicated in inflammatory demyelinating disorders including MS and Guillain Barré syndrome, where Nfasc is an autoimmune target implicating Nfasc in immune-mediated axonal injury (Levin, 2013; Devaux et al., 2012; Kawamura et al., 2013; Mathey et al., 2007; Ng et al., 2012). As a member of the L1 family, Nfasc contains an extracellular region of six immunoglobulin-like domains, three to five fibronectin type III repeats (FNIII), followed by a single-pass transmembrane domain and a short, highly conserved cytoplasmic tail (Davis and Bennett, 1993; Hassel et al., 1997) (Figure 1.2). The Nfasc transcript undergoes extensive alternative splicing resulting in numerous developmentally regulated cell specific isoforms (Hassel et al., 1997; Kriebel et al., 2012).

Four Nfasc polypeptides of 186, 155 high and 155 low, and 140 kDa have been described in the rodent nervous system (Davis et al., 1993; Hassel et al., 1997; Pomicter et al., 2010; Rathjen et al., 1987; Zhang et al., 2015). Nfasc 186 and 140 are neuronal specific isoforms and Nfasc 155 high and low have been described in myelinating glial cells. These isoforms differ primarily in the combination of FNIII domains and inclusion of hinge domains located in the extracellular domain (Hassel et al., 1997; Kriebel et al., 2012). Nfasc 186 excludes the 3rd FNIII domain and includes the mucin and 5th FNIII domains. Nfasc 186 is expressed at the AIS and nodes of Ranvier, where it is implicated in clustering of Na_v channels and stabilization of axo-axonic synapses (Desmazieres et al., 2014; Lonigro and Devaux, 2009; McEwen and Isom, 2004). Nfasc 140 excludes the mucin and 5th FNIII domains, and is present at the node of Ranvier during embryonic development where it is thought to complement the function of Nfasc 186 in initial stages of assembly and stabilization of the nodal complex (Zhang et al., 2015). Nfasc 155 includes a small hinge domain located between Ig2 and Ig3 domains and includes the 3rd FNIII domain, but excludes the Nfasc 186-specific mucin domain (Tait et al., 2000). Nfasc155 is found in oligodendrocytes and Schwann cells where it plays an important role in mediating axo-glial contact by forming paranodal septate-like junctions (Pillai et al., 2009; Sherman et al., 2005; Zonta et al., 2008). In this study we investigate the expression of Nfasc in another glial cell, microglia, and characterize its novel expression.

1.7 Chapter Summary

AIS disruption has been described in a number of pathological environments where neuroinflammation is an underlying factor; however, the mechanisms driving AIS

disruption in inflammatory conditions and whether this disruption is reversible remains to be determined. Furthermore, during chronic inflammatory conditions, microglia enhance contact with the AIS concomitant with increased AIS disruption (Clark et al., 2016); however, the molecules which mediate this contact are not yet defined. I employed an acute neuroinflammatory model to investigate the relationship between reactive microglia and the AIS throughout the inflammatory response. Additionally, I identified a novel candidate in microglia that may regulate microglial-AIS contact.

Figure 1.2

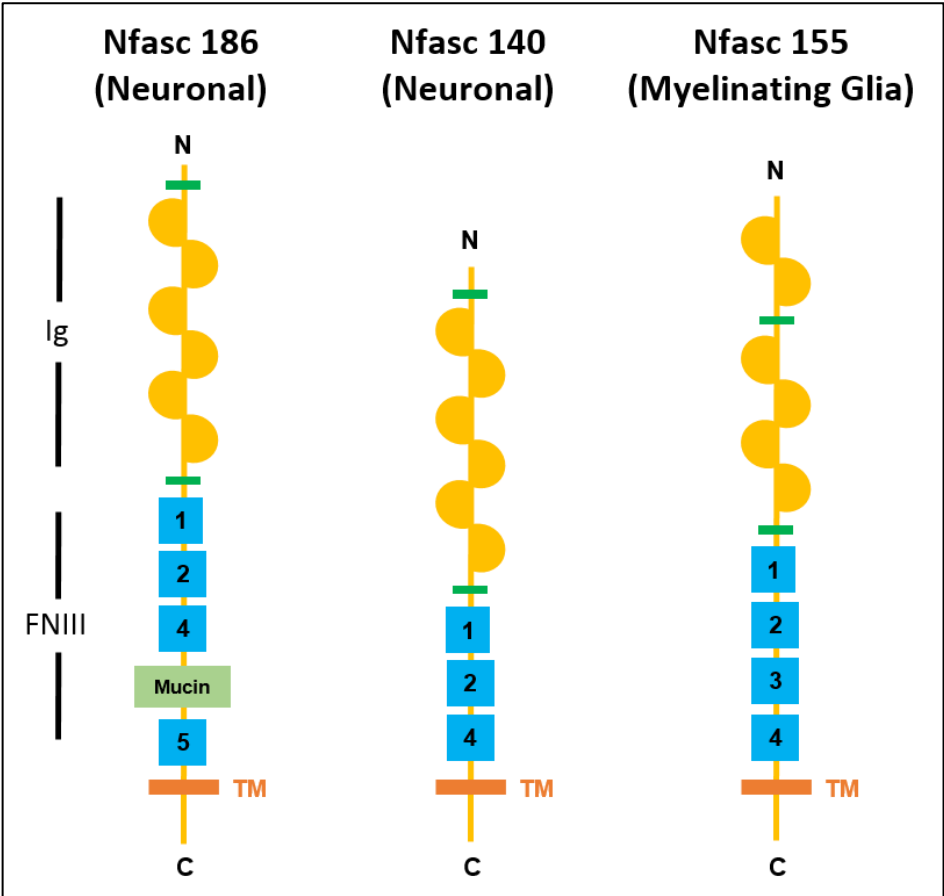


Figure 1.2. Neurofascin Domain Composition. The extracellular domain is comprised of 6 Ig-like domains (yellow half-circles), three to five fibronectin type III domains (FNIII), a mucin domain, and alternatively spliced regions (green bars). Nfasc isoforms contain a single-pass transmembrane domain (TM, orange bar) and a conserved cytoplasmic tail.

CHAPTER TWO

ACUTE NEUROINFLAMMATION INDUCES AIS STRUCTURAL PLASTICITY IN A NOX2-DEPENDENT MANNER

Some of these results have been published in
Benusa et al., 2017. *Journal of Neuroinflammation*

2.1 Abstract

BACKGROUND: Chronic microglia-mediated inflammation and oxidative stress are well characterized underlying factors in neurodegenerative disease, whereby reactive inflammatory microglia enhance ROS production and impact neuronal integrity. Recently, it has been shown that during chronic inflammation, neuronal integrity is compromised through targeted disruption of the axon initial segment (AIS), the axonal domain critical for action potential initiation. AIS disruption was associated with contact by reactive inflammatory microglia which wrap around the AIS with increased association coincidental with disease progression. While it is clear that chronic microglial inflammation and enhanced ROS production impact neuronal integrity, little is known how acute microglial inflammation influences AIS stability. Here, I demonstrate that acute neuroinflammation induces AIS structural plasticity in a ROS-mediated and calpain dependent manner.

METHODS: C57BL/6J and NOX2^{-/-} mice were given a single injection of LPS (5 mg/kg) or vehicle (0.9% saline, 10 mL/kg) and analyzed at 6h - 2wks post-injection. Anti-inflammatory Didox (250 mg/kg) or vehicle (0.9% saline, 10 mL/kg) was administered beginning 24h post-LPS injection and continued for 5 days; animals were analyzed 1wk

post-injection. Microglial inflammation was assessed using immunohistochemistry (IHC), Nanostring nCounter® mRNA analysis, and RT-qPCR. AIS integrity was quantitatively analyzed using ankyrinG, Nav1.6, and Kv1.2 immunolabeling. Data were statistically compared by one-way or two-way ANOVA where mean differences were significant as assessed using Tukey's post hoc analysis or, where applicable, data were statistically compared using a mixed-effects regression model.

RESULTS: LPS-induced neuroinflammation, characterized by enhanced microglial inflammation and increased expression of ROS-producing enzymes, altered AIS functional sub-domain clustering and induced loss of ankG-positive AISs. Importantly, inflammation-induced AIS changes were reversed following resolution of microglial inflammation. Modulation of the inflammatory response using anti-inflammatory Didox, even after significant AIS disruption occurred, increased the rate of AIS recovery. RT-qPCR and IHC analysis revealed that expression of microglial NOX2, a ROS-producing enzyme, was significantly increased correlating with AIS disruption. Furthermore, ablation of NOX2 prevented inflammation-induced AIS plasticity suggesting that ROS drive AIS structural plasticity.

CONCLUSION: In the presence of acute microglial inflammation, the AIS undergoes an adaptive change that is capable of spontaneous recovery. Moreover, recovery can be therapeutically accelerated. Together, these findings underscore the dynamic capabilities of this domain in the presence of a pathological insult and provide evidence that the AIS is a viable therapeutic target.

2.2 Introduction

The axon initial segment (AIS) is a highly specialized axonal domain responsible for action potential initiation and modulation (Yoshimura and Rasband, 2014). The AIS is characterized by a unique assembly of cytoskeletal and scaffold proteins (Grubb and Burrone, 2010) and densely packed voltage-gated ion channels, which are recruited to and clustered at the AIS via the scaffolding protein ankyrinG (ankG) (Yang et al., 2007). Properties of the AIS such as length, position and ion channel sub-domain composition determine the firing properties of individual neurons (Kole et al., 2007; Van Wart et al., 2007; Yamada and Kuba, 2016). Accumulating evidence suggests that the AIS is a dynamic domain capable of structural plasticity, undergoing changes in length (Kuba et al., 2010), location (Evans et al., 2013; Grubb and Burrone, 2010; Wefelmeyer et al., 2015), and ion channel clustering (Bened-Jensen et al., 2016; Del Puerto et al., 2015; Kuba et al., 2015) in response to neuronal pathology and altered activity.

AIS plasticity is characterized by the relocation of cytoskeletal-associated proteins such as ankG, β IV spectrin, neurofascin, and voltage gated Na^+ and K^+ channels (Chand et al., 2015; Evans et al., 2015; Grubb and Burrone, 2010; Muir and Kittler, 2014; Wefelmeyer et al., 2015). These structural changes have various functional consequences which are neuron type and region specific (Jamann et al., 2017; Yamada and Kuba, 2016). In layer 5 cortical pyramidal neurons, decreased length of AIS $\text{Na}_v1.6$ or $\text{K}_v1.2$ ion channel sub-domains reduced neuronal excitability, conversely, increased length enhanced neuronal excitability (Jamann et al., 2017; Yamada and Kuba, 2016). Through these mechanisms, neurons adapt to changes in circuit activity and fine-tune excitability.

Although plasticity can be triggered by both pathologic and non-pathologic stimuli, the mechanisms and cell types that drive plasticity remain largely unknown. Schafer et al. (2009) were the first to implicate the calcium dependent protease calpain as a mediator of AIS structural changes with recent studies confirming these findings (Del Puerto et al., 2015; Stoler and Fleidervish, 2016). Consistent with calpain activation, Evans et al. (2013) reported that AIS plasticity is triggered by calcium channel activation with downstream activation of calcineurin. These studies implicate calcium as a converging factor in AIS plasticity. Recently, microglia were also implicated in mechanisms driving AIS structural changes through direct contact with AISs. Microglial-AIS contact occurs early in development and is maintained through adulthood in the uninjured brain (Baalman et al., 2015) and during chronic inflammation present in an animal model of MS known as experimental autoimmune encephalomyelitis (EAE) (Clark et al., 2016). These studies suggest an important interaction between microglia and neurons that may influence AIS integrity.

Microglia, the resident immune cells of the central nervous system (CNS), are dynamic cells that survey, respond, and shape neuronal networks through neuronal contact and synaptic pruning (Crotti and Ransohoff, 2016b; Kettenmann et al., 2013; Miyamoto et al., 2016; Schafer and Stevens, 2013). Microglia are critical for maintaining tissue homeostasis in the CNS, rapidly activating and eliminating pathogens and cellular debris in response to infection or insult (Kierdorf and Prinz, 2013; Ransohoff and Perry, 2009; Tremblay et al., 2011). Upon activation, microglia display an enhanced pro-inflammatory response and a dampened resolving phenotype (Aguzzi et al., 2013; Prinz et al., 2014; Wong, 2013). This is typified by increased expression of inflammatory

mediators such as tumor necrosis factor alpha (Tnfa), cyclooxygenase-2 (COX-2), and NADPH oxidase 2 (NOX2), elevated production of reactive oxygen species (ROS), and reduced expression of resolving factors such as transforming growth factor beta (TGF- β), mannose receptor, C type 1 (Mrc1), and resistin like beta (Fizz-1), (Block et al., 2007; Cherry et al., 2014; Sierra et al., 2013). Though reactive microglia play an important role in pathogen clearance and CNS homeostasis, amplified ROS production or aberrant activation of the inflammatory phenotype has been implicated in a number of neuronal pathologies (Edison et al., 2008; Gomez-Nicola and Perry, 2015; Johnson et al., 2013; Ohl et al., 2016; Russo and McGavern, 2016) where AIS disruption is observed (Baalman et al., 2015, 2013; Clark et al., 2016; Marin et al., 2016; Schafer et al., 2009). Previous studies from our lab demonstrated that chronic neuroinflammation in EAE resulted in changes in AIS length and protein clustering and this disruption corresponded with increased microglial reactivity and production of pro-inflammatory factors (Clark et al., 2016). Furthermore, AIS disruption corresponded with increased contact between reactive microglia and the AIS, suggesting that in a chronic inflammatory environment, pro-inflammatory microglia may drive AIS disruption (Clark et al., 2016).

The microglial inflammatory response is amplified by the enzyme NOX2, which is responsible for the microglial respiratory burst and extracellular production of ROS (Wang et al., 2013b). NOX2 activity has been implicated in the chronic activation of microglia and its deleterious effects through both the production of extracellular ROS and through amplification of the pro-inflammatory response (Kumar et al.; Pawate et al., 2004; Qin et al., 2004). Inhibition of NOX2 reduced microglial ROS production and reduced microglia-mediated neurotoxicity (Choi et al., 2012; Qin et al., 2004, 2013). Here, I investigate the

role of microglial inflammation and the ROS-producing enzyme NOX2 on AIS integrity. Using a lipopolysaccharide (LPS)-induced model of neuroinflammation, I demonstrate that in the presence of acute microglial inflammation, AIS ankG and ion channel clustering is disrupted and upon resolution of inflammation, AIS changes are reversed. Furthermore, ablation of NOX2 preserved AIS integrity. These data underscore the dynamic capabilities of the AIS in the presence of a pathological insult.

2.3 Methods

Animals

6-8 weeks (wks) old C57BL/6J mice and NOX2 deficient (B6.129S-Cybb^{tm1Din}/J, NOX2^{-/-}) mouse breeding pairs were purchased from Jackson Laboratories (Bar Harbor, ME). All animals were maintained in the AAALAC accredited McGuire Veterans Affairs Medical Center (VAMC) vivarium with access to food and drink *ad libitum*. NOX2^{-/-} mice have a targeted mutation of the 91kD subunit of the oxidase cytochrome b and lack phagocyte superoxide production (Pollock et al., 1995). NOX2^{-/-} mice are maintained on a C57BL/6J background; therefore, age-matched C57BL/6J mice (NOX2^{+/+}) were used as controls. All procedures were conducted in accordance with the National Institutes of Health guidelines for the care and use of laboratory animals and were approved by the McGuire VAMC Institutional Animal Care and Use Committee.

LPS treatment

Lipopolysaccharide (LPS; O111:B4, lot: 2728527) was purchased from Calbiochem (San Diego, CA). Female C57BL/6J and NOX2^{-/-} mice (8-12 wks) were given a single intraperitoneal (IP) injection of LPS (5 mg/kg or 10mg/kg (Sup. Fig. 2.3), 10 mL/kg) or vehicle (0.9% saline). The LPS dose was based on the previously established neuroinflammation model (Qin et al., 2007; Taetzsch et al., 2015) where peripheral inflammation rapidly transfers to the brain, resulting in elevated microglial cytokines and ROS production (Taetzsch et al., 2015). Saline- and LPS-treated mice were analyzed at 6 hours (h), 24h, 3 days (d), 1wk, and 2wks post-injection to assess the effects of microglial reactivity and AIS integrity throughout the course of neuroinflammation.

Didox Administration

Didox (3,4-dihydroxybenzohydroxamic acid) was obtained from Molecules for Health, Inc. (Richmond, VA). Didox, a ribonucleotide reductase inhibitor and free radical scavenger, is a multifunctional compound that inhibits DNA replication, suppresses NF- κ B activation, reduces oxidative injury and attenuates microglia/macrophage production of inflammatory cytokines and ROS producing enzymes (Matsebatlela et al., 2015; Shah et al., 2015; Turchan et al., 2003). An initial Didox paradigm was used to investigate reversibility of AIS disruption: Didox (250 mg/kg solubilized in 0.9% saline) or vehicle (0.9% saline, 10 mL/kg) was administered intraperitoneally beginning at 1 week post-LPS injection and continued for 6 days. Animals were taken for analysis 2 weeks post-LPS injection (Sup. Fig. 2.2). These data revealed spontaneous AIS recovery in the LPS 2wk vehicle controls (Sup. Fig. 2.2). Additionally, a second paradigm was used to address the

question of reversibility (Fig. 2.7). For this study, Didox or vehicle was administered intraperitoneally beginning at 24 hours post-LPS injection and continued for 6 days. Animals were taken for analysis 1 week post-LPS injection.

Calpain Inhibitor Administration

Calpeptin was obtained from Calbiochem (San Diego, CA). Calpeptin is a cell-permeable inhibitor of calcium-activated proteases calpain-1 and calpain-2, which have been implicated in targeted cleavage of AIS proteins and alterations in AIS structure (Bened-Jensen et al., 2016; Del Puerto et al., 2015; Schafer et al., 2009). Based on previous studies (Das et al., 2013; Guyton et al., 2010; Smith et al., 2011), Calpeptin (50ug/kg) or vehicle (0.1% dimethyl sulfoxide in saline, 10mL/kg) was administered subcutaneously 30 minutes prior to injection of LPS (5 mg/kg, 10 mL/kg, IP) or vehicle (0.9% saline, 10 mL/kg, IP). On Days 1 and 2 post LPS injection, mice received a second and third dose of Calpeptin (calpain inhibitor), respectively. Vehicle, LPS + vehicle, or LPS + Calpeptin treated mice were analyzed at 3d post-LPS injection to assess the effects of calpain activity on AIS integrity.

Tissue Preparation and Immunohistochemistry

Mice were deeply anesthetized using 0.016 mL/gm body weight of a 2.5% solution of avertin (2, 2, 2 tribromoethanol; Sigma-Aldrich; St. Louis, MO) in 0.9% sodium chloride (Sigma-Aldrich, St. Louis, MO), and transcardially perfused with 4% paraformaldehyde (Ted Pella, Redding, CA) (Clark et al., 2016; Dupree et al., 1999). Following perfusion,

brains were removed and immersed in 0.1 M PBS containing 30% sucrose for 48 h and frozen in Optimal Cutting Temperature compound (Sakura, Tokyo, Japan). Brains were serially sectioned into 40 µm thick coronal sections spanning 1.1 mm anterior to Bregma to 2.5 mm posterior to Bregma using a Leica CM 1850 cryostat. Fifteen sets of six sections were collected and placed on ProbeOn Plus slides (Fisher Scientific, Loughborough, UK) and stored at -80°C.

Sections were immunostained using the following antibodies: mouse monoclonal anti-ankyrin G (AnkG; NeuroMab, Davis, CA; N106/36, 1:500), rabbit polyclonal anti-Iba1 (Wako Chemicals, Richmond, VA; 019-19741; 1:1,000), mouse monoclonal anti-NeuN (Millipore; Billerica, MA; MAB377; 1:1,000), rabbit monoclonal anti-NeuN (Abcam, Cambridge, MA; ab177487; 1:500), mouse monoclonal anti-gp91-phox (Santa Cruz; Dallas, TX; sc-130543; 1:500), mouse monoclonal anti-Nav1.6 (Nav1.6; NeuroMab, Davis, CA; K87A/10, 1:200), mouse monoclonal anti-Kv1.2 (Kv1.2; NeuroMab, Davis, CA; K14/16, 1:200). All secondary antibodies were obtained from Invitrogen Life Technologies (Grand Island, NY; Alexa™ Fluor) and used at a dilution of 1:500. Immunolabeling was performed as previously described (Clark et al., 2016; Pomicter et al., 2010) with some modifications: 0.5% Triton X-100 and 10mM sodium-citrate buffer oven retrieval (30 minutes at 80°C) was used for antigen retrieval. Nuclear stain BisBenzimide (Sigma-Aldrich, St. Louis, MO, 1:1000) was used to identify cortical layers. Slides were mounted with Vectashield™ (Vector Laboratories, Burlingame, CA); and imaged using confocal microscopy.

Imaging and Analysis

Imaging was performed on a Zeiss LSM 710 confocal laser scanning microscope (Carl Zeiss Microscopy, LLC, Thornwood, NY) housed in the VCU Department of Anatomy and Neurobiology Microscopy Facility. For AIS number analysis, images were collected as previously described (Clark et al., 2016). Briefly, confocal z-stacks spanning an optical thickness of 25 μ m, using a pinhole of 1 Airy disc unit and Nyquist sampling (optical slice thickness, 0.48 μ m) were collected from neocortical layer V for each of six sections per mouse. For AIS ankG counts, 12 images per animal ($n=4-6$ animals per treatment group) were collected and images were blinded then processed and analyzed using FIJI (NIH ImageJ software). Settings were optimized by comparing manual AIS tracings (previously described by Clark et al., 2016) , and FIJI automated counts; no significant difference was found between methods (Sup. Fig. 2.1). Once established, settings remained constant throughout analysis. Thresholds of maximum intensity projections of ankG labeling were automatically set using the Otsu threshold method (Otsu, 1979) and AISs were quantified using the *Analyze Particles* plugin (FIJI) (size: 0-infinity μ m²; circularity: 0-0.5; objects touching edges excluded). AnkG positive structures measuring <10 μ m were excluded from analysis consistent with previous studies (Baalman et al., 2013; Clark et al., 2016; Marin et al., 2016).

For AIS ion channel sub-domain analysis, confocal z-stacks spanning an optical thickness of 20 μ m from neocortical layer V were collected from triple-labeled tissue sections (NeuN, ankG, and Nav1.6 or Kv1.2). Images were blinded and detailed AIS sub-domain analysis was performed on 60 AISs per experimental group ($n=3$ animals per experimental group). Z-stacks were collapsed into single maximum intensity projections

and imported into FIJI (NIH ImageJ software). Using the maximum intensity projection of the merged channels, an axonal profile was traced starting at the edge of the soma (identified by NeuN), continuing distally along the axon (identified by ankG), through and past the region of the AIS. This region of interest was then superimposed onto each individual channel (AnkG and Nav1.6 or Kv1.2) and a fluorescent intensity profile for each pixel along the region of interest was generated. From each AIS histogram, the proximal position (start) and distal position (end) relative to the soma edge as well as total domain length of ankG, Nav1.6, or Kv1.2 labeling was determined (Fig. 2.2, 2.3). These positions were calculated where fluorescent intensity profiles rose above background. Background levels were calculated per image as the mean intensity density along a 20 μm region of interest traced through a region absent of labeling. Averages of start position, end position, and length of AIS sub-domains were quantified and compared among experimental groups.

For analysis of microglial NOX2 immunoreactivity, confocal z-stacks spanning an optical thickness of 25 μm , were collected from neocortical layer V per mouse ($n=3$ animals per treatment group). Images were blinded and NOX2 immunoreactivity in Iba-1⁺ cells was quantified using Volocity™ 3D Image Analysis Software version 6.3 allowing 3D confirmation of double immunolabeling in each Iba-1⁺ cell. The total number of microglia and the number of NOX2⁺ microglia were counted manually for each double immunolabeled z-stack. Data are presented as the percent of NOX2⁺ microglia (Iba-1⁺) per field of view.

For microglia-AIS contact analysis, confocal z-stacks spanning an optical thickness of 25 μm were collected from triple-labeled tissue sections (NeuN, ankG, and

Iba-1) as described above. Images were blinded and contact between microglia and AISs was quantified using Volocity™ 3D Image Analysis Software version 6.3 allowing each confocal z-stack to be observed in three dimensions. The number of microglia, AISs, and contact points in each triple immunolabeled z-stack were quantified in a semi-automated manner. Using Volocity™ a protocol was generated to find co-localized pixels between Iba-1 and ankG in three dimensions using the confocal z-stack, creating a bounding rectangle around each co-localization. Only contact points in which the microglial cell body and the full AIS could be identified were quantified. Contact points along the six edges of the z-stacks were excluded from analysis. To obtain the number of microglia per image, Iba-1 positive cell bodies were identified using volume restrictions and objects touching the six edges of the z-stacks were excluded. Likewise, the number of AISs was obtained by quantifying ankG positive objects using shape and volume exclusion criteria to distinguish AIS ankG labeling from nodal ankG labeling. AIS numbers were compared to values obtained through automated ankG analysis using FIJI (described above) to validate the Volocity™ method. Data are reported as the number of microglial contacts, number of microglial cells, percent of microglia making contact, and percent of AISs contacted per FOV for each experimental group.

For neuronal nuclei analysis (NeuN labeling), four confocal images per mouse were collected using a 20X objective with a numerical aperture of 1.4 and a pinhole of 1 Airy disc unit. Images were processed and analyzed using FIJI ($n=3$ mice per treatment group). Settings were optimized by comparing manual NeuN counts (previously described (Clark et al., 2016)) and FIJI automated counts; no significant difference was found between methods (data not shown). Thresholds of maximum intensity projections of

NeuN labeling were automatically set using the Otsu threshold method (Otsu, 1979), and neuronal nuclei were quantified using the *Analyze Particles* plugin (size: 10-150 μm^2 ; circularity: 0-1; objects touching edges excluded). No differences in NeuN⁺ cell counts were detected among any treatment groups (NOX2^{+/+} Saline, NOX2^{+/+} LPS-injected, NOX2^{-/-} Saline, or NOX2^{-/-} LPS-injected, Table 2.1).

Cortical volume analysis was performed using the Cavalieri principle as previously described (modified from (Hahn et al., 2015; Mouton, 2013)). Briefly, unbiased stereology was performed using every fifteenth section from the total sections spanning the cortical region 1.1 mm anterior to Bregma to 2.5 mm posterior to Bregma and analyzed to estimate cortical volume. Each reference space was outlined with a 2X objective and analyzed using a point-grid analysis, sampling 100% of the regions of interest. Samples were counted in a blind manner and volumes calculated using an Olympus BX51 microscope (Center Valley, PA) and newCAST software (Visiopharm, Hoersholm, Denmark). ($n=3-4$ mice per treatment group). No differences in cortical volumes were detected among any treatment groups (NOX2^{+/+} Saline, NOX2^{+/+} LPS-injected, NOX2^{-/-} Saline, or NOX2^{-/-} LPS-injected, Table 2.1).

Microglial Isolation

Adult cortical microglia were isolated using MACS magnetic bead separation (Miltenyi Biotec, San Diego, CA) as described previously (Clark et al., 2016; Taetzsch et al., 2015). Briefly, saline treated and LPS treated mice were deeply anesthetized with 2.5% avertin and transcardially perfused with 50mL ice-cold PBS. After removal of the meninges, cerebral cortices of two mice were harvested and pooled per sample (2

mice = 1 *n*) and suspended in Hank's Balanced Salt Solution (HBSS) without CaCl₂ and MgCl₂ (Corning, Corning, NY). A single-cell suspension was prepared using the Miltenyi Neural Tissue Dissociation Kit according to manufacturer's instructions. The cells were depleted of myelin by suspension in 3 mL of 30% isotonic Percoll™ (GE Healthcare Life Sciences, Pittsburgh, PA) followed by a 10 min centrifugation at 700 x *g* at 4°C. The cell pellet was washed in 5 mL HBSS without CaCl₂ and MgCl₂ and isolation of microglia was performed with magnetic CD11b microbeads (Miltenyi) and MACS magnetic separator (Miltenyi) according to manufacturer's instructions.

RNA isolation and gene expression analysis

To assess microglial phenotype throughout the LPS-mediated response I used a multiplexed assay to quantify messenger RNA (mRNA) expression of 248 inflammation-associated genes. The Nanostring nCounter gene expression analysis system allows for direct labeling of mRNAs with molecular barcodes called nCounter Reporter Probes without the use of reverse transcription or amplification (Geiss et al., 2008). Total RNA was extracted from isolated CD11b⁺ cells using a Qiagen RNeasy mini kit (Qiagen, Germantown, MD) and treated with Ambion DNase I (Invitrogen Life Technologies, Grand Island, NY) (*n*=3 samples per experimental group). RNA concentrations were determined using a NanoPhotometer (Implen, Los Angeles, CA) and purity was assessed by the ratio of absorbance at 260 and 280 nm ($OD_{260/280} > 1.8$). Extracted RNA (40 ng/μl) was sent for analysis to the J.S. and Bobbi Allen Gene Expression Analysis Laboratory at the University of Tennessee Health Science Center (Memphis, Tennessee). The nCounter® Mouse Inflammation v2 Panel (NanoString Technologies, Seattle, WA) was used to

profile 254 genes; 248 inflammation-related genes + 6 internal reference (housekeeping) controls. Background subtraction was performed using the maximum value across samples of the negative controls and data normalization was performed using the geometric mean expression of 6 internal reference genes: Clathrin Heavy Chain (CLTC), Glyceraldehyde-3-Phosphate Dehydrogenase (GAPDH), Glucuronidase Beta (Gusb), Hypoxanthine Phosphoribosyltransferase (Hprt), Phosphoglycerate Kinase 1 (Pgk1), Tubulin Beta Class (Tubb5). Reporter probe counts reflecting the numbers of mRNA transcript in the RNA sample, were analyzed and quantified using the nSolver™ Analysis Software (Version 2.5, NanoString Technologies). Normalized data were used to calculate differentially expressed genes which were up-regulated or down-regulated at least 2-fold or greater among experimental groups. Differentially expressed genes were used for Gene Ontology-Biological Process (GO-BP) enrichment analysis using the Database for Annotation, Visualization and Integrated Discovery (DAVID software v6.8, Frederick, MD) (Huang et al., 2009a, 2009b). The GO-BP term, percentage, and Benjamini score is presented. A GO-BP term is presented if that biological process (function) was enriched within the list of genes input for analysis. The percentage represents the sample frequency or the number of genes annotated to that GO term from the input list. The Benjamini score is a globally corrected enrichment *P*-value. This is an indicator of the significance of gene-term enrichment such that genes which were input are significantly more enriched than by random chance. The smaller the *P*-value, the more significant it is; default cutoff was set to 0.1 as suggested by DAVID (Huang et al., 2009b).

RT-qPCR was used to confirm mRNA expression changes detected by the Nanostring system for a subset of genes. Oligo-dT-primed cDNAs were synthesized from 0.25 µg of RNA for each sample using the iScript Reverse Transcription Supermix (BioRad) according to the manufacturer's guidelines. RT-qPCR reactions with at least two technical replicates per sample were performed on a CFX96 real-time PCR detection system (BioRad) using 1 µL of cDNA, SsoFast Evagreen Supermix (BioRad), and forward and reverse primers (500 nM). Cycling parameters were one cycle at 95°C (5 min), 40 cycles of 95°C (5 s) and 56°C (5 s) followed by a melt curve measurement consisting of 5 s 0.5°C incremental increases from 65°C to 95°C. Relative changes in gene expression were calculated by the $2^{-\Delta\Delta C_t}$ method (Livak and Schmittgen, 2001) using cyclophilin A and PGK1 as internal reference controls. Gene-specific primers were designed and checked for specificity using National Center for Biotechnology Information/Primer-BLAST (basic local alignment search tool; (Ye et al., 2012)) (Primer sequences are presented in Table 2.2). Primers were generated by Integrated DNA Technologies (San Diego, CA).

Calpain Activity Assay

To quantify the levels of calpain activity and to determine the effect of Calpeptin on inhibition of calpain activity, vehicle, LPS + vehicle, or LPS + Calpeptin treated mice were deeply anesthetized and transcardially perfused with 50mL ice-cold 0.9% saline at 3d post-LPS injection. Cerebral cortices (10mg) were harvested and immediately homogenized in ice-cold extraction buffer (Calpain activity kit- ab65308, Abcam, Cambridge, MA). Samples were centrifuged for 5 minutes at 4°C at 15,000 x g to remove

insoluble material. Calpain activity was quantified using a fluorometric calpain activity assay kit according to manufacturer's protocol. All samples were analyzed in triplicate and calpain activity was measured using a Tecan M1000 PRO microplate reader (Männedorf, Switzerland). Changes in calpain activity were normalized to saline control levels and expressed as Relative Fluorescent Units (RFU).

Statistical Analysis

For AIS counts and gene expression data, graphing and statistical analyses were performed using GraphPad Prism version 6.03 (GraphPad Software, San Diego, CA). Data were analyzed by a one-way or two-way analysis of variance and where mean differences were significant, assessed using Tukey's Honest Significance Difference post hoc analysis. Treatment groups were presented as percent of saline control (% Control \pm SEM) and $p < 0.05$ was considered statistically significant.

For AIS ion channel sub-domain quantitation, graphing was performed using GraphPad Prism version 6.03 and statistical analyses were performed using JMP Pro version 12.2.0 (a distribution of SAS). To determine statistically significant differences among AIS Nav1.6 and Kv1.2 structure in ankG-positive neurons between saline or LPS-injected groups, I employed multilevel modeling (Aarts et al., 2014; Vascak et al., 2017). Multilevel modeling was constructed using the experimental condition at the animal level (saline- or LPS-injected), where the outcome variable (e.g., AIS domain length) consists of multiple measurements per animal (i.e., nested data). This modeling accounts for both intra-animal variability (variability among independent AIS measurements) and the variability between animals (outcome measure as a function of each animal) to preserve

Type I error rate ($\alpha = 0.05$) (Aarts et al., 2014). To conduct multilevel modeling, an *F* test was used to determine if the multilevel model accounted for the variability in the data set. If the *F* test yielded $p < 0.05$, I concluded that the model fit the data and continued our analysis. Next, multiple contrasts were used to compare the least squares mean of each experimental group to that of saline control with the threshold for significance set at $\alpha < 0.05$. AIS summary statistics (*t* ratio, degrees of freedom, and *p*-value) and outcome measures (mean \pm SEM) were calculated from nested data sets (e.g., $N = 60$ AISs total, 20 AISs nested per animal, $n = 3$ mice). Treatment groups were presented as mean \pm SEM.

2.4 Results

LPS-induced inflammation disrupts AIS ankG clustering

Studies from our laboratory (Clark et al., 2016) and others (Baalman et al., 2015; Hinman et al., 2013; Schafer et al., 2009) have shown that AIS protein clustering is disrupted during chronic inflammation and disease. To determine if acute neuroinflammation alters AIS integrity, I used a LPS-induced neuroinflammatory model and assessed AIS ankG protein clustering (Fig. 2.1). AISs were immunolabeled for ankG in saline- and LPS-treated mice at 6h, 24h, 3d, and 1wk post-injection. Disruption of ankG labeling was first observed 24h post-LPS injection ($71.6\% \pm 3.7$, $p < 0.01$) compared to saline controls ($100\% \pm 5.8$) (Fig. 2.1C&G). The number of AISs detected in LPS-injected mice remained significantly decreased at both 3d and 1wk post-injection ($72.7\% \pm 2.5$, $p < 0.01$ and $65.3\% \pm 5.1$, $p < 0.0001$, respectively) compared to saline controls (Fig. 2.1D,E,G). To determine if loss of ankG-positive AISs was a consequence of neuronal

loss or changes in cortical volume, I quantified NeuN immunolabeling and cortical volume and found no difference among saline or LPS treated groups (Table 2.1). These data suggest that acute neuroinflammation caused a significant disruption in AIS structural organization, but altered ankG detection was not associated with neuronal loss.

AIS structural disruption is reversible

The AIS is the site of action potential initiation and thus is critical for neuronal function (Buffington and Rasband, 2011). Studies have shown that the AIS can undergo structural plasticity in development and in response to pathological insults to sustain proper signaling within neuronal networks (Grubb and Burrone, 2010; Gutzmann et al., 2014; Kuba et al., 2010, 2015b). To determine *in vivo* if inflammation-induced AIS disruptions are reversible, ankG clustering of AISs in saline- and LPS-treated mice was assessed 2wks post-injection (Fig. 2.1). AnkG immunolabeling revealed that the number of AISs in LPS-treated mice 2wks post-injection returned to baseline and was not significantly reduced compared to saline controls ($91.3\% \pm 2.8$) (Fig. 2.1F-G). Furthermore, AISs at 2wks post-LPS injection were significantly increased compared to LPS 1wk treated mice (mean difference: $25.9\% \pm 5.7$, $p < 0.01$) (Fig. 2.1E-G). Thus, LPS-induced disruption of AIS ankG clustering is reversible.

LPS-induced inflammation disrupts AIS functional domains

AnkG is not only critical for the molecular organization but also for proper function of the AIS, as loss of ankG disrupts action potential initiation and axonal identity

(Hedstrom et al., 2008; Jenkins and Bennett, 2001; Zhou et al., 1998). However, to investigate whether neurons, which maintain AIS ankG clustering ($71.6\% \pm 3.7$, Fig. 2.1), are also affected during inflammation, I assessed the integrity of AIS functional sub-domains. The polarized distribution of ion channel subtypes within the AIS are important for the initiation and modulation of APs (Baranauskas et al., 2013; Hu et al., 2009; Kole et al., 2008; Palmer and Stuart, 2006; Van Wart et al., 2007). Nav1.6 channels are distally clustered at the AIS and are the primary ion channels contributing to spike initiation at the AIS (Colbert and Pan, 2002; Hu et al., 2009; Kole et al., 2008; Van Wart et al., 2007); thus, a change in density or distribution of these channels alters neuronal firing properties. Similarly, Kv1.2 channels influence neuron firing frequency and action potential half-width, and thus a change in their distribution can also impact neuronal signaling (Dodson et al., 2002; Goldberg et al., 2008; Kole et al., 2007; Kuba et al., 2015b). The length and location relative to soma of Nav1.6 and Kv1.2 ion channel sub-domains were quantified in ankG-positive neurons from saline- and LPS-treated mice at 6h, 3d, 1wk, and 2wks post-injection (Fig. 2.2 - 2.4)(Table 2.3-5). At 6h post-LPS injection, AIS ankG length is significantly decreased compared to saline controls ($20.36 \mu\text{M} \pm 0.6$ and $22.5 \mu\text{M} \pm 0.6$, respectively, $p < 0.05$, Fig. 2.4A-C). This shortening remains at both 3d and 1wk post-injection ($19.9 \mu\text{M} \pm 0.6$, $p < 0.05$ and $18.5 \mu\text{M} \pm 0.6$, $p < 0.0001$, respectively); however, ankG length is restored and significantly increased at 2wks post-LPS injection ($24.5 \mu\text{M} \pm 0.6$, $p < 0.05$) compared to saline controls (Fig. 2.4A-C). For Nav1.6 AIS sub-domain, a significant decrease in length was first detected at 3d post-LPS injection ($15.5 \mu\text{M} \pm 1.1$, $p < 0.01$) compared to saline controls ($20.4 \mu\text{M} \pm 1.1$) (Fig. 2.4D-F). This length was recovered by 1wk post-injection and maintained at 2wks post-LPS injection ($17.3 \mu\text{M} \pm$

1.1, $p = 0.07$ and $19.4 \mu\text{M} \pm 1.1$, $p = 0.51$, respectively, Fig. 2.4D-F). Similarly, a significant decrease in Kv1.2 domain length was observed in LPS injected mice at 6h ($14.9 \mu\text{M} \pm 1.0$, $p < 0.05$) and 3d ($14.2 \mu\text{M} \pm 1.0$, $p < 0.05$) compared to saline controls ($18.1 \mu\text{M} \pm 1.0$). This reduction was recovered by 1wk post-injection and maintained at 2wks post-LPS injection ($16.6 \mu\text{M} \pm 1.0$, $p = 0.31$ and $17.3 \mu\text{M} \pm 1.0$, $p = 0.61$, respectively)(Fig. 2.4G-I). No significant changes were detected in the start position of ankG, Nav1.6 or Kv1.2 domains in any of the experimental groups (Fig. 2.4A,D,G); however, a significant shift in the end positions of domain labeling was observed (Fig. 2.4B,E,H) demonstrating the overall decrease in domain length occurred from the distal end of the AIS. These data show that acute inflammation drives changes in both structural and functional AIS domains and, importantly, these disruptions are reversible.

Increased Inflammatory Insult does not Prevent AIS Recovery

To better understand the level of insult after which the AIS cannot recover, I performed a small study with an LPS dose (10mg/kg) that is reported in the literature to be a lethal dose (LD) 50 (von Drygalski et al., 2013; Ma et al., 2017; Warren et al., 2010). Mice received a single IP LPS 10mg/kg or saline injection and AISs were quantified 2 wks post-injection (Sup. Fig. 2.3), a time point that showed reversibility with the lower LPS dose (5mg/kg)(Fig. 2.1). No difference in AIS number was found between saline and LPS 10mg/kg mice (Sup. Fig. 2.3) demonstrating that an increase in initial inflammatory insult is not sufficient to prevent AIS recovery.

AIS Disruption Coincides with Microglial Inflammatory Response

Previous studies demonstrated that chronic neuroinflammation in EAE resulted in disruption of the AIS, and this disruption coincided with microglial reactivity and increased microglial/AIS contact (Clark et al., 2016). Quantitation of microglial/AIS contact during acute neuroinflammation revealed that while microglia make contact with AISs, there were no differences in the number of microglial/AIS contacts or percent of microglia making contact in LPS-injected mice (Fig. 2.5) suggesting that rather the microglial phenotype, at the time of contact, may contribute to AIS disruption. Therefore, to better understand how microglial inflammation contributes to AIS integrity in LPS-induced neuroinflammation, I examined microglial reactivity and gene expression of inflammatory mediators in saline- and LPS-treated mice. AIS disruption was first observed 6h post-LPS injection and remained significantly disrupted until recovery 2wks post-injection. Therefore, I assessed microglial reactivity 6h, 24h, 3d, 1wk, and 2wks post-injection. Iba-1 immunostaining revealed that at 6h post-LPS injection microglia display a reactive phenotype that is maintained 1wk post-LPS injection (Fig. 2.6B-E). By 2wks post-LPS injection (Fig. 2.6F) microglia morphology returned to a surveying phenotype similar to that of saline-injected mice (Fig. 2.6A).

To characterize microglial gene expression throughout the LPS-mediated response, I used Nanostring gene array technology to quantify mRNA expression of 248 inflammation-associated genes from saline- and LPS-injected mice. This revealed that 55 genes were significantly altered at 6h in LPS-injected mice (LPS 6h vs. saline). 42 of these genes were significantly up-regulated and GO-BP function analysis revealed that these genes were involved in functions related to positive regulation of the inflammatory

response, production of Tnf α , nitric oxide biosynthetic process, chemotaxis and chemokine signaling (Table 2.6). Conversely, 13 inflammation-associated genes were down-regulated at 6h post-LPS injection and the associated functions involved regulation of TGF- β receptor signaling, cell proliferation, cell migration, and regulation of transcription (Table 2.7). While the 13 genes were associated with these pathways, Benjamini values suggest that these functions are not significantly enhanced for the input list ($p > 0.1$). A gene expression pattern reflecting resolution of inflammation was detected at 1wk post-LPS injection, a time-point preceding recovery of AIS and G loss. At 1wk post-LPS injection, 17 genes were significantly up-regulated compared to saline controls and those genes are involved in functions similar to those seen at 6h (positive regulation of the inflammatory response, Tnf α production, and chemotaxis) (Table 2.8); however, 74 genes were significantly down-regulated at 1wk post-LPS injection compared to the LPS 6h time point. These genes were also associated with pathways involving immune response, chemokine-mediated signaling, NF- κ B activity, and response to Tnf α (Table 2.9). Thus, while some genes associated with the pro-inflammatory response remained elevated compared to saline controls, the majority of gene expression changes at 1wk revealed a down-regulation of those involved in the pro-inflammatory response suggesting a resolution of this phenotype. Consistent with this premise, functions related to growth factor production were significantly increased at 1wk compared to 6h (Table 2.10). Furthermore, microglial gene expression at LPS 2wks is similar to saline controls demonstrating that a return to baseline expression is consistent with recovery of AIS disruption. These data demonstrate that at 6h post-LPS injection, microglia mount a pro-inflammatory response characterized by increased NF- κ B activity and increased

chemokine and reactive species-producing pathways while downregulating functions involved in production of neurotrophic factors and migration. These changes in microglial phenotype were concomitant with induction of AIS disruption.

qPCR analysis confirmed changes in gene expression of a subset of inflammatory mediators. Gene expression of *Tnfa*, *COX-2*, and *NOX2* was significantly upregulated 6h post-LPS injection ($p < 0.05$, Fig. 2.7G-I). mRNA expression of *NOX2*, the enzyme responsible for extracellular release of ROS and amplification of microglial pro-inflammatory response (Wang et al., 2013b), was significantly increased at 6h ($p < 0.01$) and remained elevated 3d post-LPS injection ($p < 0.05$), returning to control levels prior to AIS recovery (Fig. 2.7I). Furthermore, gene expression of resolving factors *Mrc1*, *TGF- β* , and *Fizz-1* was significantly decreased by 24h post-LPS injection and returned to control levels by 1 week post-injection, coincident with AIS disruption and recovery, respectively ($p < 0.05$, Fig. 2.7J-L). Thus, the microglial inflammatory response coincided with the disruption and recovery of AIS clustering.

Treatment with the Anti-inflammatory Didox Reverses AIS Disruption

In LPS-induced inflammation microglia rapidly respond, displaying dramatic morphological alterations and significantly increasing expression of pro-inflammatory genes while significantly downregulating expression of pro-resolution factors (Fig. 2.8). mRNA expression of microglial inflammatory markers remained elevated and was not resolved until 1wk post-LPS injection. However, 35% of neurons maintain a loss of ankG clustering at the AIS and neurons, which are positive for ankG clustering, remain significantly shortened at 1wk post-injection and these disruptions do not recover until

2wks post-injection (Fig. 2.1 -2.4). To determine if AIS recovery could be accelerated by a therapeutic approach, I treated LPS-injected mice with the anti-inflammatory and free-radical scavenger Didox (Inayat et al., 2002, 2010; Matsebatalela et al., 2015; Mayhew et al., 2002). Didox administration was initiated 24h post-LPS injection (Fig. 2.8E), when microglia were reactive and there was a significant loss of AIS ankG clustering. Following treatment of saline- and LPS- injected mice, neurons, which maintained AIS ankG labeling at 24h and 1wk post-injection, were quantified. At 24h post-injection, ankG clustering in LPS-treated mice ($71.6\% \pm 3.7$, $p < 0.01$, Fig. 2.8B,F) was significantly disrupted compared to saline controls. The number of AISs in LPS-injected mice remained significantly decreased 1wk post-injection ($65.3\% \pm 5.1$, $p < 0.001$, Fig. 2.8C,F) compared to saline controls. However, in LPS+Didox mice, the number of neurons with AISs was significantly higher compared to LPS 1wk untreated mice ($96.3\% \pm 2.8$, $p < 0.01$) and was not significantly different from saline controls (Fig. 2.8D,F). Thus, treatment with Didox reversed loss of AIS ankG and increased the rate of AIS recovery.

AIS sub-domain analysis was performed in neurons that remained ankG-positive (Fig. 2.9); LPS+Didox mice had a significant distal shift in AIS ankG end position ($22.4 \mu\text{M} \pm 0.62$, $p < 0.01$) and overall ankG length ($21.2 \mu\text{M} \pm 0.62$, $p < 0.01$) compared to LPS 1wk untreated mice (18.9 ± 0.61 and $18.5 \mu\text{M} \pm 0.61$, respectively). Interestingly, a distal shift in the ankG start position of LPS+Didox treated mice was also detected compared to LPS 1wk untreated mice ($1.1 \mu\text{M} \pm 0.14$ and $0.43 \mu\text{M} \pm 0.14$, respectively, $p < 0.01$)(Fig. 2.9A-C). Initial ion channel sub-domain analysis of Nav1.6 and Kv1.2 revealed a significant shortening of domain lengths in LPS mice and this length was recovered to saline control levels by 1wk post-injection (Fig. 2.9F,I). Likewise, when these domains were quantified

in ankG-positive neurons of LPS+Didox mice, no significant changes in length ($18.4 \mu\text{M} \pm 1.1$, $p = 0.49$) or location ($3.2 \mu\text{M} \pm 1.0$, $p = 0.18$) was detected with Didox treatment at 1wk post-LPS injection (Fig. 2.9D-I). These data demonstrate that AIS structural disruptions are reversible and can be therapeutically modulated.

Treatment with Didox Alters Microglial NOX2 Expression

Didox is a ribonucleotide reductase inhibitor that modulates the inflammatory response through inhibition of NF- κ B activation, reduction of ROS producing enzymes, and reduction of oxidative injury (Elford et al., 2007; Matsebatlela et al., 2015; Turchan et al., 2003). To determine the effect of the treatment of anti-inflammatory and free-radical scavenger Didox on microglial inflammatory response and AIS integrity following LPS treatment, I analyzed microglial NOX2 expression, which is dependent on, and induced by, NF- κ B (Anrather et al., 2006; Morgan and Liu, 2011). NOX2 is a ROS-producing enzyme primarily expressed by microglia and has been implicated as the primary producer of extracellular ROS and oxidative stress in the CNS (Guemez-Gamboa et al., 2011; Kumar et al.; Nayernia et al., 2014; Qin et al., 2004). Quantitation of NOX2 immunolabeling (Fig. 2.10A-D) in cortical microglia from saline and LPS-treated mice with or without Didox treatment revealed that NOX2 immunoreactivity was significantly enhanced in microglia 24h post-LPS injection (Fig. 2.10B, E) and remained significantly elevated 1wk post-LPS injection (Fig. 2.10C, E) compared to saline controls ($p < 0.0001$, Fig. 2.10A, E). However, NOX2 immunoreactivity was decreased in LPS-injected mice treated with the anti-inflammatory and free-radical scavenger Didox ($p < 0.0001$, Fig.

2.10D, E). Thus, Didox treatment significantly decreased microglial NOX2 back to saline control levels, and this decrease corresponded with the reversal of AIS disruption.

Ablation of NOX2 Prevents AIS Disruption

Although Didox is a known free radical scavenger and the data demonstrate a reduction in NOX2 expression resulting from Didox treatment, it is possible that Didox targets other inflammatory factors and that the observed AIS recovery was only coincidental with inhibition of NOX2 expression. Therefore, to more specifically investigate the role that NOX2 plays in AIS disruption, I exploited NOX2^{-/-} mice. I injected NOX2^{+/+} and NOX2^{-/-} mice with saline or LPS and assessed AIS integrity 24h and 1wk post-injection. AnkG clustering in NOX2^{+/+} LPS-injected mice was significantly disrupted at 24h (Fig. 2.11B) and 1wk (Fig. 2.11C) post-injection resulting in an ~30% loss of AISs, compared to saline controls ($p < 0.01$, Fig. 2.11G). Strikingly, ankG clustering in LPS-injected NOX2^{-/-} mice was not significantly different at either 24h or 1wk post-injection compared to saline-injected NOX2^{-/-} mice (Fig. 2.11E, F). However, ankG clustering was significantly higher at both 24h and 1wk compared to NOX2^{+/+} LPS-injected mice ($p < 0.01$, Fig. 2.11G). To confirm that NOX2^{-/-} mice still exhibit a pro-inflammatory response after LPS injection, IHC and quantitative RT-PCR was used (Sup. Fig. 2.4). Analyses revealed that microglia from LPS-injected NOX2^{-/-} mice displayed reactive morphologies, enhanced contact with AISs, and up-regulated mRNA expression of Tnfa and COX2 (Sup. Fig. 2.4). Thus, ablation of NOX2-derived ROS prevented inflammation-induced AIS disruption.

Inhibition of Calpain Prevents AIS Disruption

To further elucidate the mechanism of inflammation-induced AIS disruption, I investigated the calcium-activated protease calpain. Calpain activity has been implicated in AIS structural changes and the targeted proteolysis of AIS proteins (Bened-Jensen et al., 2016; Del Puerto et al., 2015; Schafer et al., 2009). To determine if calpain activity is involved in inflammation-induced loss of AIS ankG clustering, I treated LPS-injected mice with the calpain inhibitor Calpeptin. Calpeptin administration was initiated 30 minutes prior to LPS injection and continued once daily for two days (Fig. 2.12D). Following treatment, AISs were immunolabeled for ankG at 3d post-LPS injection. AnkG clustering in LPS-treated mice ($72.7\% \pm 2.5$, $p < 0.01$, Fig. 2.12B,E) was significantly disrupted compared to saline controls ($100\% \pm 5.8$, Fig. 2.12A,E). However, in LPS + Calpeptin treated mice the number of AISs was significantly greater compared to LPS 3d vehicle treated mice ($90.2\% \pm 2.3$ and $72.8\% \pm 2.5$, respectively, $p < 0.05$, Fig. 2.12C,E) and was not significantly different from saline controls. Inhibition of calpain activity by Calpeptin was determined by a fluorometric calpain activity assay on mouse cortical homogenates 3d post-LPS injection (Fig. 2.12F). Calpain activity was significantly increased in LPS 3d mice ($132.9\% \pm 3.0$, $p < 0.01$, Fig. 2.12F) compared to saline controls ($100\% \pm 5.3$) and treatment with Calpeptin significantly reduced calpain activity in cortical homogenates ($84.1\% \pm 3.1$, $p < 0.001$, Fig. 2.12E). Thus, inhibition of calpain activity prevents inflammation-induced disruption of AIS ankG clustering in cortical neurons.

2.5 Discussion

In this study, I demonstrate that LPS-induced neuroinflammation disrupts protein clustering at the AIS concomitant with the microglial inflammatory response resulting in a loss of AIS detection in ~30% of cortical neurons. Additionally, neurons that maintain ankG labeling also exhibit disrupted AIS Nav1.6 and Kv1.2 functional sub-domains. Importantly, I found that inflammation-induced AIS disruptions were reversed concomitant with resolution of microglial inflammation and loss of AIS ankG clustering is NOX2-mediated and dependent on calpain activity. Thus, in the presence of acute microglial inflammation, AIS structural and functional domains undergo an adaptive change which is reversible, underscoring the dynamic capabilities of this domain in the presence of a pathological insult.

The AIS has the Capacity to Adapt and Recover

The AIS is targeted for disruption in injury and disease emphasizing its need for homeostatic adaptations. Indeed, many studies (Baalman et al., 2015, 2013; Clark et al., 2016; Hamada and Kole, 2015; Harty et al., 2013; Kaphzan et al., 2011) have shown that the AIS is plastic, undergoing change in response to various stimuli. However, few studies have demonstrated that these changes are reversible. Alterations in AIS length (Evans et al., 2015) and location (Grubb and Burrone, 2010) caused by changes in neural activity were reversible *in vitro*; however, loss of AIS protein clustering due to ischemic insults *in vitro* were not, even in the absence of cell death (Schafer et al., 2009). A previous study examining AIS integrity after stroke observed axonal sprouting resulting in an increase of small, immature AISs demonstrating reparative potential of this domain (Hinman et al.,

2013). Furthermore, our laboratory previously reported that shortening of AIS length is reversible following treatment with the anti-inflammatory Didox (Clark et al., 2016). Here, I provide evidence that loss of AIS protein clustering is spontaneously reversible, independent of axonal sprouting. Moreover, I show that by modulating the neuroinflammatory response using therapeutic intervention, the rate of AIS recovery can be increased, even after significant AIS disruption has occurred. These data suggest that while insults at the AIS, such as ischemia (Schafer et al., 2009), can cause irreversible damage, the AIS has the capacity to adapt and recover after insult. The mechanism by which this occurs or what the extent of injury is after which the AIS cannot recover, remains to be determined.

Functional Consequences of Inflammation-induced AIS Disruptions

The intricate structural-functional architecture of the AIS determines the firing properties of an individual neuron that can then influence circuit activity among its many cortical connections. Here, I show that in the presence of acute neuroinflammation, ~30% of cortical neurons lose detection of AIS ankG (24h →1wk). The remaining neurons maintain ankG detection; however, their ion channel sub-domains Nav1.6 and Kv1.2 are altered and these changes are detected preceding loss of ankG (6h →1wk). These data provide indirect evidence that LPS-induced inflammation may drive initial changes in neuronal activity, as early as 6h post-injection, inducing changes to the AIS structural-functional architecture. While it has been established that dramatic loss of ankG disrupts spike initiation (Hedstrom et al., 2008; Jenkins and Bennett, 2001; Zhou et al., 1998), recent studies have shown that more subtle changes in AIS architecture also have

significant functional consequences (Harty et al., 2013; Vascak et al., 2017). Vascak et al. (2017) found that in a model of mild traumatic brain injury (mTBI) a 1.9 μ m decrease in ankG from the distal AIS coincided with a significant disruption in AIS AP acceleration measured by whole-cell patch clamp. Furthermore, they detected a change in AP threshold reflecting a disruption in Nav1.6 clustering, though using immunofluorescence they did not detect a structural change. Consistent with these findings, I report a significant shortening of AIS ankG; however, I also detected a significant change in the Nav1.6 domain. Importantly, I found that these changes occurred from the distal AIS. Nav1.6 channels set AP threshold and these channels are densely clustered at the distal AIS, forming the site of AP spike initiation (“trigger zone”) (Kole and Stuart, 2012b; Kole et al., 2008); therefore, a reduction in Na⁺ conductance at the distal AIS would suggest decreased AP generation. Additionally, I found a significant distal shortening of Kv1.2 channels. Kv1.2 channels control AP waveform and can suppress AP generation by counteracting Nav channels (Dodson et al., 2002; Goldberg et al., 2008; Kole et al., 2007). While a reduction in available Kv1 channels could, therefore, lower AP threshold and increase AP generation (Kole et al., 2007; Kuba et al., 2015b), I observed a proportional change in Kv1.2 and Nav 1.6 sub-domains. Based on this data, I posit that the effect of the overall shortening of the AIS could dominate leading to a reduction in excitability. This could occur because the overall decrease in Na⁺ conductance reduces the ability of the AIS to overcome the effects of somato-dendritic loads making it difficult to depolarize the AIS above the AP threshold (reviewed in (Kuba et al., 2015b; Yamada and Kuba, 2016).

Here, I show that as early as 6h after peripheral LPS injection layer 5 cortical neurons alter AIS functional sub-domains by shifting their distal clustering closer to the

soma. These data suggest that in the presence of acute neuroinflammatory insults the AIS displays plasticity, undergoing rapid structural-functional remodeling as a potential means to modulate excitability. While the alteration and return of AIS structural-functional domains suggests a mechanism of homeostatic plasticity, whether these changes are adaptive or maladaptive remains to be determined. Furthermore, immunofluorescent analysis provides indirect evidence of functional plasticity at the AIS; however, electrophysiological recordings are needed to determine the true functional consequences and potential recovery both on the level of individual neurons and throughout the circuit.

Microglial Phenotype Influences AIS Integrity

Although AIS plasticity can be triggered by both pathological and non-pathological stimuli, the events that drive plasticity remain largely unknown. Recently, Baalman et al. (2015) established a relationship between microglia and the AIS, revealing that microglia contact AISs early in development and throughout adulthood in the uninjured brain suggesting an important interaction that may influence neuronal excitability. In a model of chronic neuroinflammation, reactive microglia increased contact with AISs, and this contact both preceded AIS disruption and increased with disease progression suggesting that in a chronic inflammatory environment increased microglial contact may drive AIS disruptions (Clark et al., 2016). Consistent with previous findings, I found that reactive microglia contact the AISs during LPS-induced neuroinflammation. However, contrary to findings in the chronic inflammatory model, the amount of contact made by microglia did not increase throughout the course of inflammation and did not correlate with AIS

disruption (Fig. 2.5). The microglial inflammatory profile, however, did correspond with AIS disruption and recovery. The expression of numerous pro-inflammatory factors by microglia peaked at 6h, a time point prior to loss of ankG-positive AISs but concomitant with decreased length in ankG-positive AISs and distal shortening in ion channel subdomains, and remained elevated until 3d post-LPS injection. These data show that in the presence of peak inflammation ankG clustering is initially shortened but sustained exposure results in loss of ~30% of ankG-positive AISs. Furthermore, as microglial genes associated with reparative functions return to control levels, AIS ion channel clustering recovers (1wk) and ankG loss recovers (2wks). Additionally, modulation of the inflammatory profile using anti-inflammatory treatment increased the rate of AIS recovery. Though my findings suggest that changes in microglial inflammation correspond with AIS alterations, it is possible that these changes do not directly influence AIS integrity. However, the direct association of microglia with the AIS suggests that this axonal domain may be particularly vulnerable to changes in microglial reactivity. Thus, my findings suggest that AIS integrity may be influenced by microglial phenotype, with a pro-inflammatory phenotype driving AIS disruption while a resolving phenotype hastens repair.

Consistent with this premise, Klupal et al. (2016) showed that incubation of hippocampal cultures with activated microglia or the pro-inflammatory cytokine Tnf α increased neuronal excitability. In contrast, incubation with the pro-resolution factor TGF- β decreased Na⁺ current density to control levels. Together, these findings suggest that neuroactive factors released by microglia augment neuronal excitability, which drives AIS structural changes (Evans et al., 2015; Grubb and Burrone, 2010; Kuba et al., 2010).

Here, I demonstrate that AIS structure is altered following significant increases in microglial expression of Tnf α . Furthermore, this AIS alteration is reversed after expression of microglial TGF- β is enhanced. Thus, my findings are consistent with microglial neuroactive factors driving changes in neuronal activity and AIS structural plasticity.

NOX2-mediated ROS, Calpain, and AIS Changes

During insult, pro-inflammatory microglia increase expression of inflammatory mediators and ROS producing enzymes (Block et al., 2007; Bordt and Polster, 2014; Qin et al., 2004; Taetzsch et al., 2015). ROS are highly reactive and diffuse signaling molecules that regulate cell functions through redox modification of target proteins. ROS can result in further production of reactive species (Feissner et al., 2009; Peng and Jou, 2010) and elevated calcium levels (Hudasek et al., 2004), which have been implicated in AIS disruption. In this study, I show that changes in microglial expression of ROS-producing enzymes corresponds with AIS disruption and recovery suggesting a role for microglial ROS in inflammation-driven AIS disruption. Consistent with this premise, ablation of NOX2 prevented AIS disruption. Though NOX2 is primarily expressed by microglia, NOX2 is also present in cortical neurons where it plays a role in ROS regulation and calcium dynamics (Wang et al., 2013a). Therefore, NOX2 ablation may preserve AIS integrity through both the prevention of microglial ROS release and neuronal NOX2 ROS production both of which may converge on pathways resulting in AIS changes.

Reactive species such as hydrogen peroxide and nitric oxide influence calcium-permeable channels including L-type calcium (Hool, 2008; Hool and Arthur, 2002; Hudasek et al., 2004) and transient receptor potential *M* (TRPM) ion channels (Aarts and

Tymianski, 2005; Wehage et al., 2002). Upon activation, intracellular calcium concentrations rise, resulting in the subsequent activation of calcium-regulated proteins such as calpain (Bened-Jensen et al., 2016; Del Puerto et al., 2015; Schafer et al., 2009), calcium/calmodulin-dependent protein kinase type II (CamKII) (Evans et al., 2013), and calcineurin (Evans et al., 2013, 2015), which have been implicated in AIS disruption. Consistent with previous studies (Bened-Jensen et al., 2016; Del Puerto et al., 2015; Schafer et al., 2009), my data implicate the calcium-dependent protease calpain as a mediator of AIS structural changes. In this study, I demonstrate that acute neuroinflammation increases calpain activity consistent with disruption of AIS ankG clustering and inhibition of calpain prevents inflammation-induced disruptions. Together, my data suggest that NOX2-derived ROS and calpain activity are drivers of AIS structural disruption during acute neuroinflammation.

Conclusion

In conclusion, I demonstrate that in the presence of acute neuroinflammation protein clustering at the AIS is altered. I reveal that inflammation-driven plasticity at the AIS is mediated by NOX2 and calpain activity. Importantly, my data demonstrate that this AIS disruption is reversible and that the AIS has the capacity to adapt and spontaneously recover.

Figure 2.1

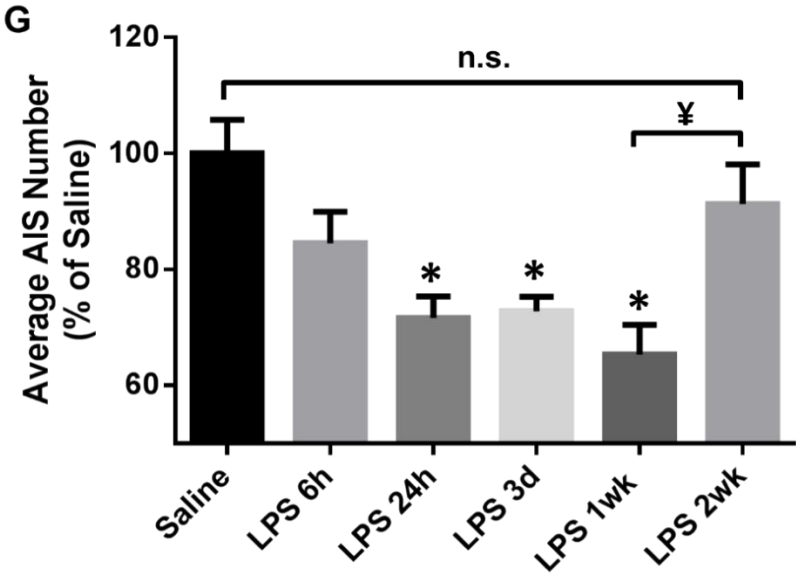
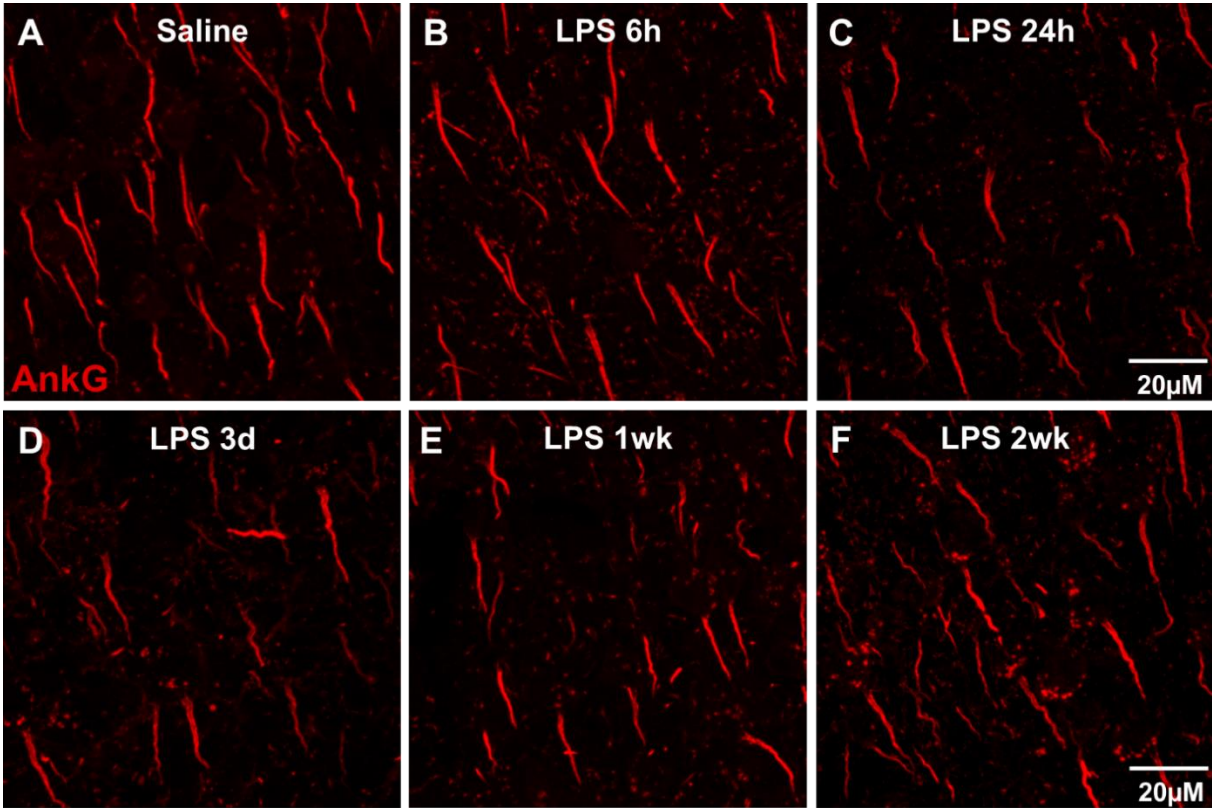


Figure 2.1. LPS-induced Inflammation Disrupts AISs. A-E, AISs in layer V of the cerebral cortex identified by ankG immunolabeling in saline- (A) and LPS-treated (B-E) mice. AIS detection is lost with time in LPS treated mice through 1wk post injection. However, by 2 weeks post injection (F), AIS number returns to control levels demonstrating a reversibility of AIS disruption. Scale bar = 20 μ M. G, The mean \pm SEM of AISs/FOV in saline- and LPS-treated mice as a percent of saline controls. An asterisk indicates significant difference ($p < 0.05$) from saline, and a \yen indicates a difference between time points.

Figure 2.2

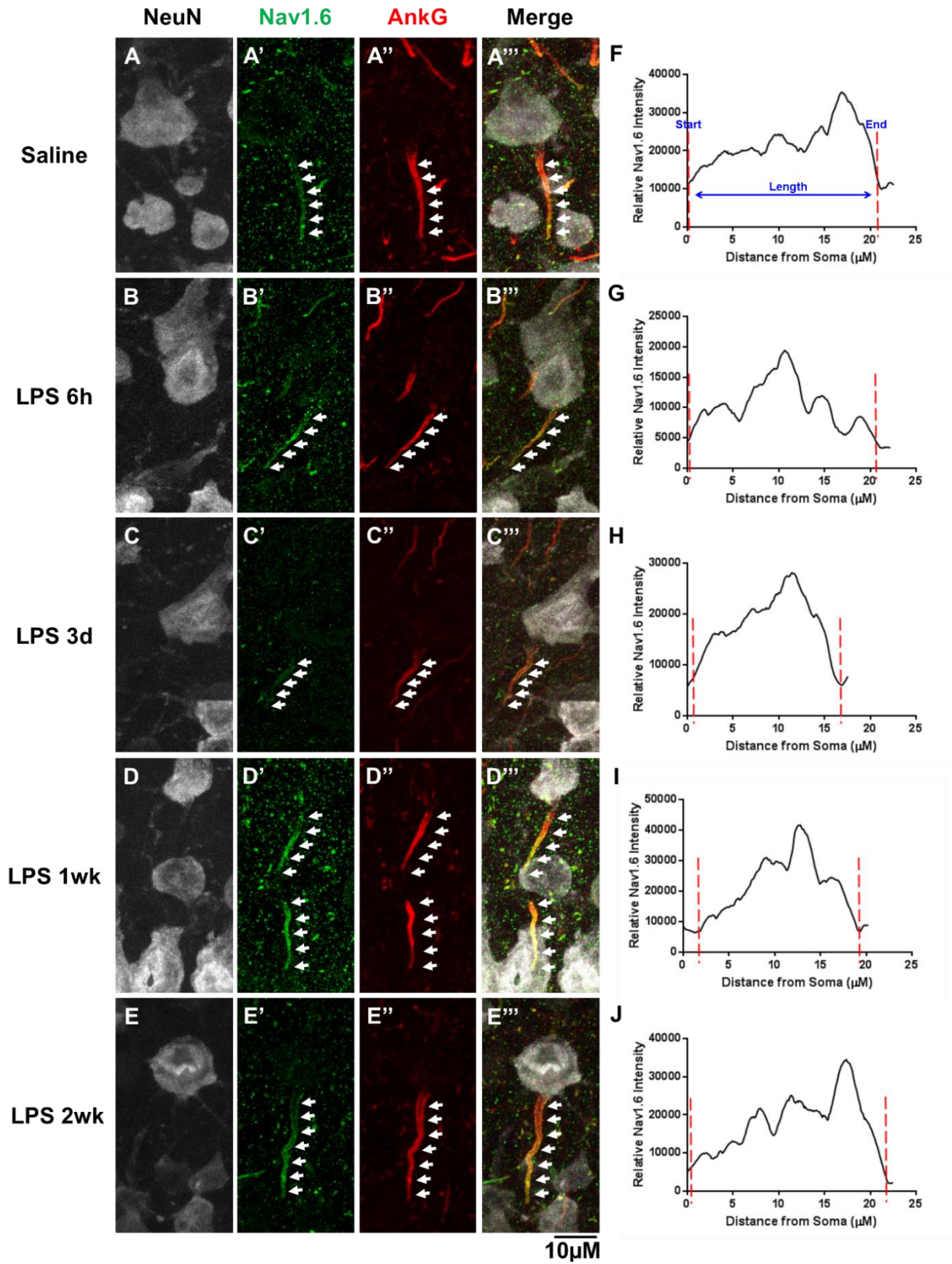


Figure 2.2. LPS-induced Inflammation Disrupts AIS Nav1.6 Functional Sub-domains. A-E, Representative images of AISs in layer V of the cerebral cortex identified by ankG and Nav1.6 immunolabeling in saline- (A) and LPS-injected mice (B-E). F-J, representative fluorescent intensity profiles of Nav1.6 labeling (A'-E') demonstrate a proximal shift in the Nav1.6 end position towards the NeuN⁺ soma 6h (B'', G), 3d (C'', H), and 1wk (D'', I) post-LPS injection revealing an overall shortening of the Nav1.6 functional sub-domain.

Figure 2.3

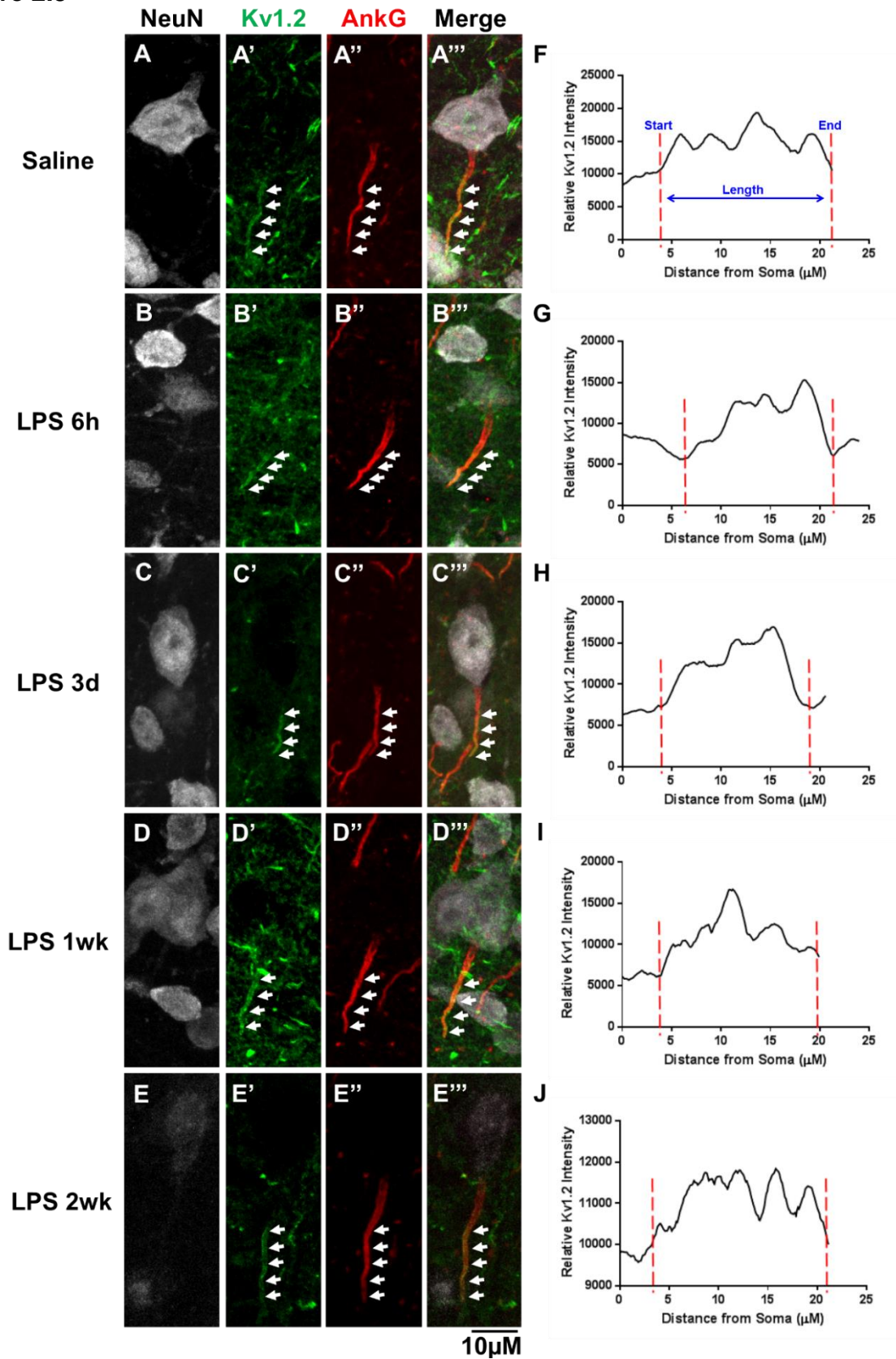


Figure 2.3. LPS-induced Inflammation Disrupts AIS Kv1.2 Functional Sub-domains.

A-E, Representative images of AISs in layer V of the cerebral cortex identified by ankG and Kv1.6 immunolabeling in saline- (A) and LPS-injected mice (B-E). F-J, representative fluorescent intensity profiles of Kv1.6 labeling (A'-E') demonstrate a proximal shift in the Kv1.6 end position towards the NeuN⁺ soma 6h (B''', G) and 3d (C''', H) post-LPS injection revealing an overall shortening of the Kv1.6 functional sub-domain.

Figure 2.4

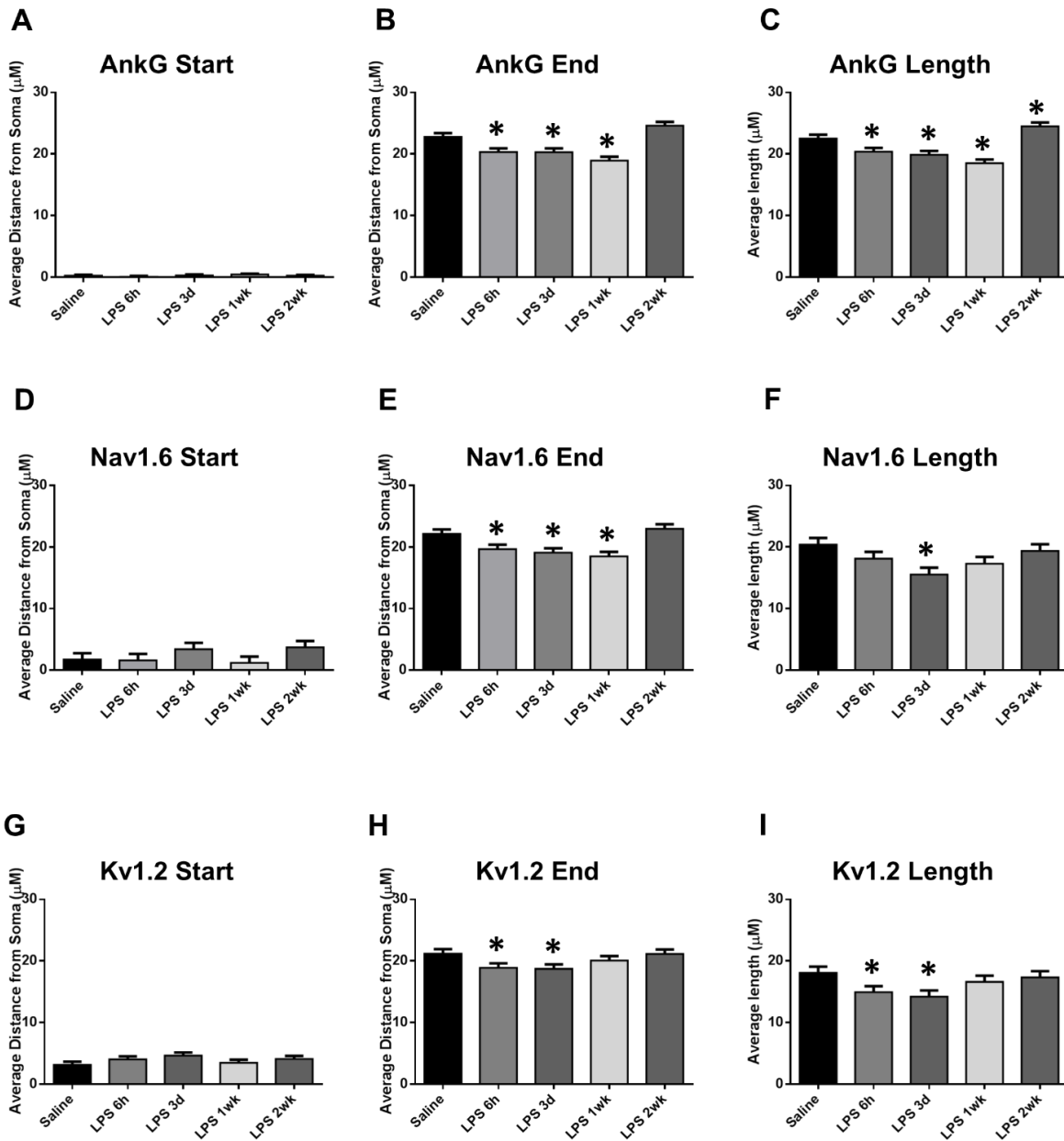


Figure 2.4. LPS-induced Inflammation Disrupts AIS Functional Sub-domains. The mean \pm SEM of ankG (A-C), Nav 1.6 (D-F), and Kv1.2 (G-I) start and end positions relative to soma edge and total length are presented. A significant shift in the distal location of ankG, Nav1.6, and Kv1.2 was detected at both 6h and 3d post-LPS injection; however, the distal location of these proteins returned to control positions by 2wks post injection (B,E,H). No differences in the start position of ankG, Nav 1.6, or Kv1.2 were detected (A,D,G) demonstrating that significant shortening of AIS sub-domain lengths (C,F,I) occurs from the distal AIS. An asterisk indicates significant difference ($p < 0.05$) from saline.

Figure 2.5

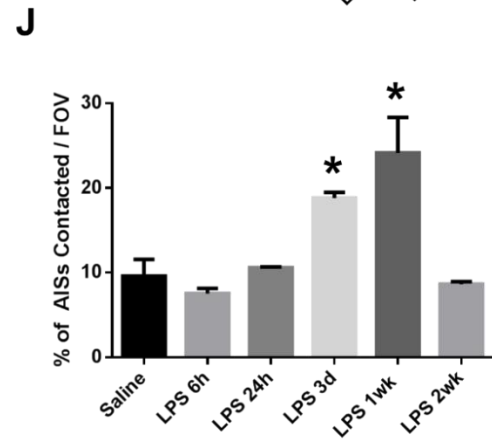
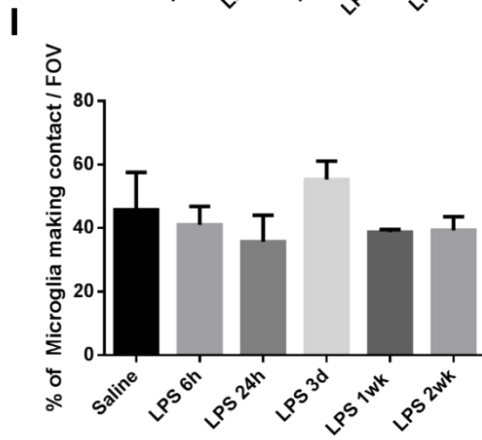
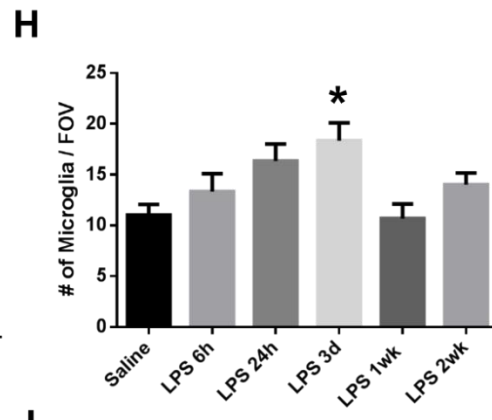
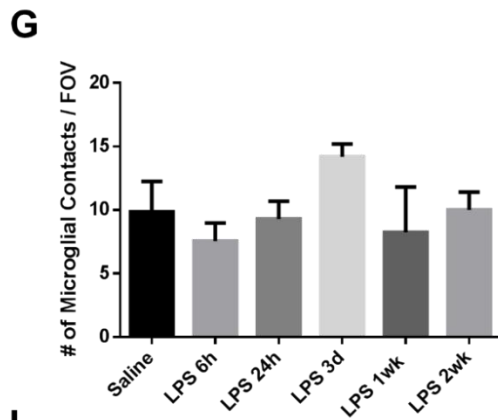
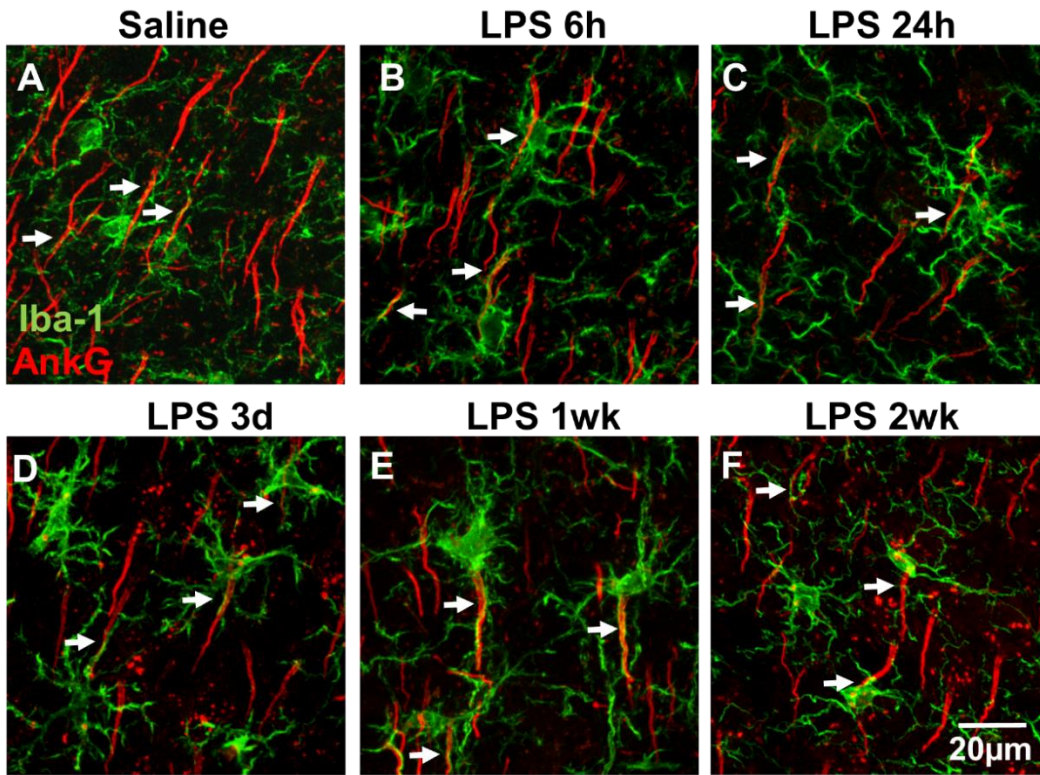


Figure 2.5. Microglial-AIS Contact does not coincide with AIS Disruption in LPS-Injected mice. A-F, Double immunolabeling of Iba-1 and AnkG revealed that microglia (Iba-1, green) contact AISs (AnkG, red) (white arrows) in saline and LPS injected mice. No change in the number of microglial contacts (A) or percent of microglia making contact (C) per field of view was observed. A significant increase in the number of microglia was observed at 3d post-LPS injection (B) and a significant increase in the percent of AISs contacted at 3d and 1wk post-LPS injected was detected (D). However, these were at time points where a significant decrease in the number of AISs was detected (Fig. 2.1); thus, since the amount of total contact did not change (A), it is unlikely that the amount microglia-AIS contact alone was responsible for disruption. An asterisk indicates significant difference ($p < 0.05$) from saline.

Figure 2.6

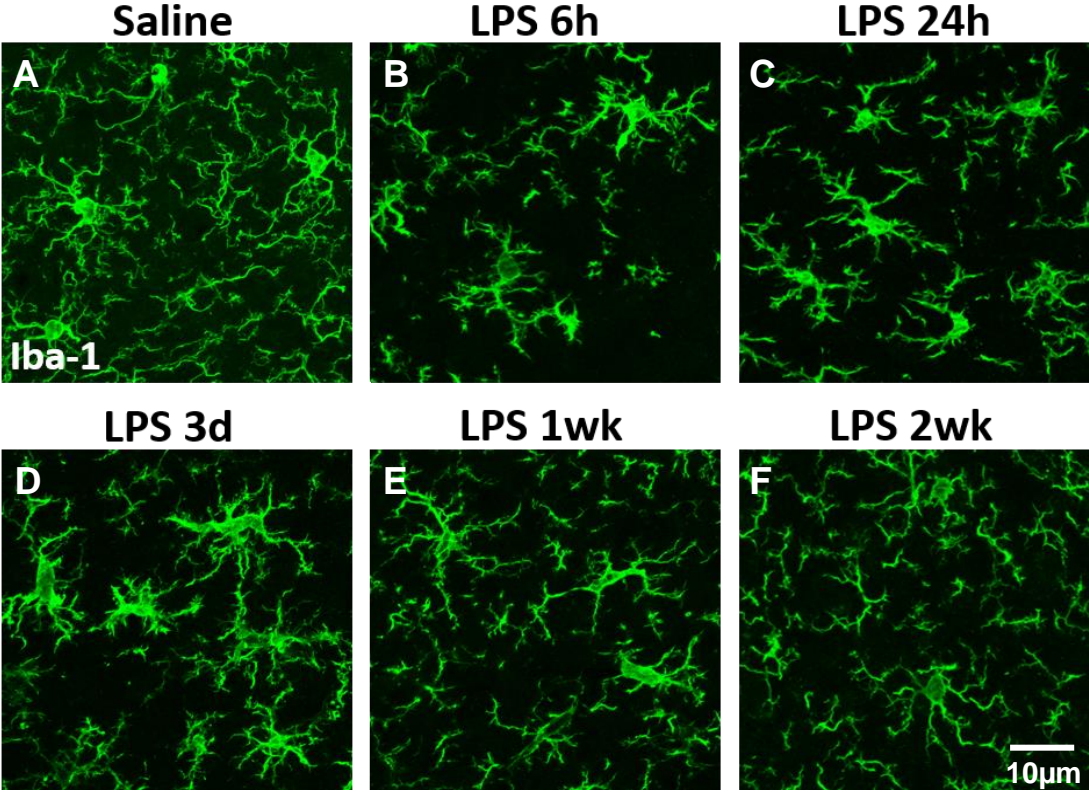


Figure 2.6. AIS Integrity Coincides with Microglial Reactivity. A-F, Microglia, visualized by Iba-1 immunolabeling, displayed a surveying phenotype with long, highly branched processes in saline-treated mice (A). As early as 6 hr post LPS injection, microglia displayed a reactive morphology with retracted, thickened processes (B), this morphology was maintained at 24h (C), 3d (D), and 1wk (E) post-LPS injection. Microglia returned to a surveying morphology at 2wk (F) post-LPS. Scale bar = 10 μ M.

Figure 2.7

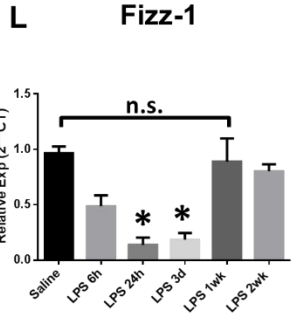
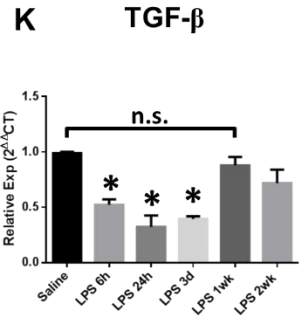
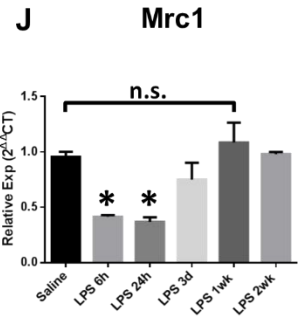
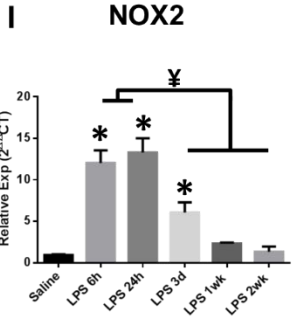
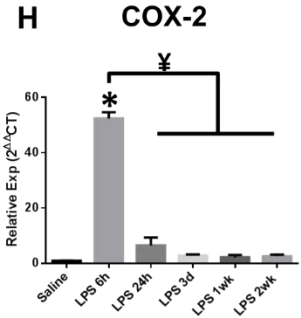
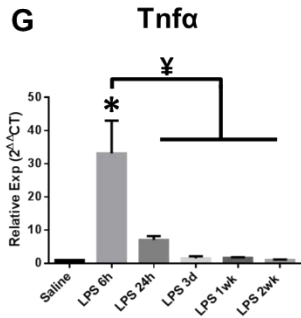
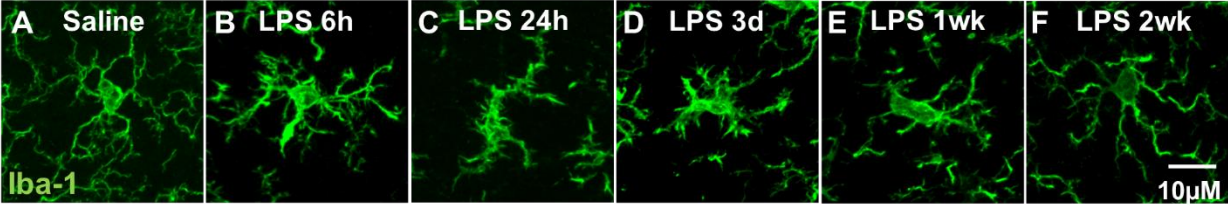


Figure 2.7 AIS Integrity Coincides with Microglial Inflammatory Response. A-F, In addition to the morphologic changes presented by microglia following LPS injection (compare A to B-F), mRNA expression was used to further analyze inflammatory mediators in isolated cortical microglia from saline- and LPS-treated mice (G-L). Consistent with microglial morphologies, inflammatory markers were significantly upregulated at 6 hours post LPS injection (G-I). Maintenance of this pro-inflammatory phenotype was supported by the persistence of significantly elevated NOX2 expression, which did not return to baseline levels until 1 week post injection (I). Similarly, markers associated with resolution of inflammation were reduced following LPS injection and expression of these markers did not return to control levels until 1 week post injection (J-L). mRNA expression was evaluated by quantitative RT-PCR, values were normalized using the $2^{-\Delta\Delta CT}$ method and were reported as mean expression \pm SEM. An asterisk indicates significant difference ($p < 0.05$) from saline, and a \neq indicates a difference between time points post-LPS injection.

Figure 2.8

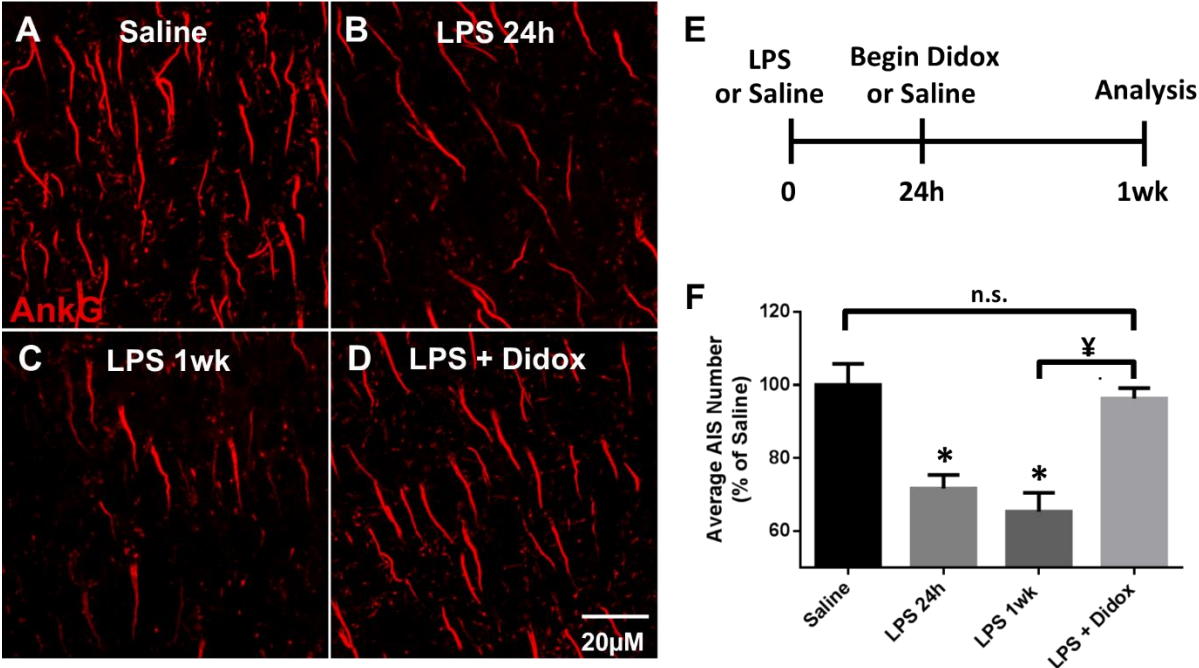


Figure 2.8. Treatment with Didox Reverses AIS Disruption. A-D, the number of AISs, as identified by immunolabeling for ankG, was reduced through 1wk post injection. LPS-injected mice that received Didox treatment beginning at 24 h post injection and continued for 5 subsequent days, displayed no loss in ankG+ labeled AISs (D). Scale bar = 20 μ M. E, schematic of LPS and anti-inflammatory Didox administration. F, the mean \pm SEM of AISs/FOV in saline-, LPS-treated, and LPS+Didox mice as a percent of saline controls. An asterisk indicates significant difference ($p < 0.05$) from saline, and a \yen indicates a difference between treatment groups.

Figure 2.9

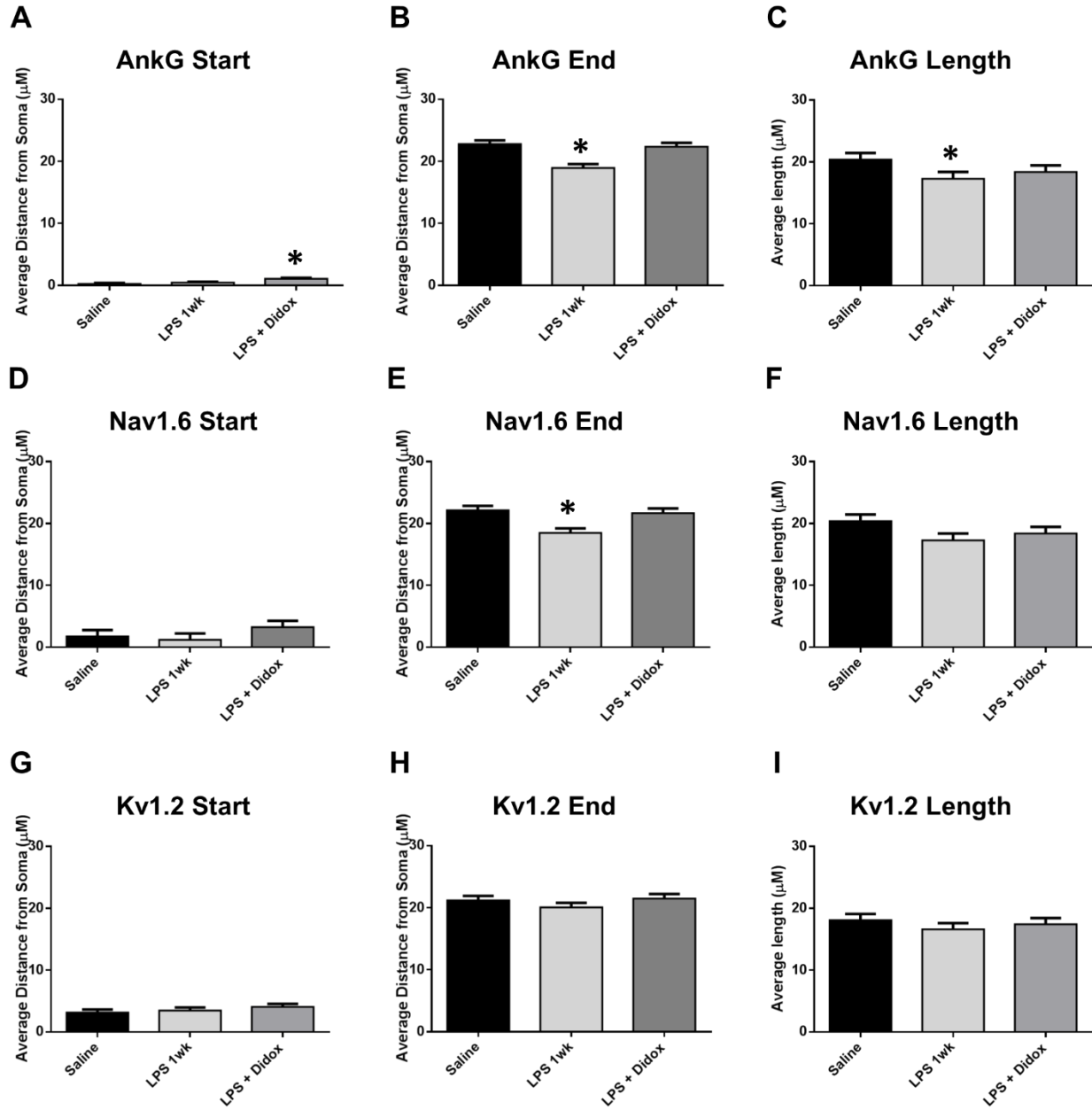


Figure 2.9. Treatment with Didox Reverses AIS Distal Shortening. AISs in layer V of the cerebral cortex were identified by ankG immunolabeling in saline-, LPS-, and LPS+Didox treated mice. The mean \pm SEM of ankG (A-C), Nav1.6 (D-F), and Kv1.2 (G-I) start and end positions relative to soma edge and total length are presented. AISs have a significant shift in the distal location of ankG and Nav1.6 (closer to soma) through 1 week post-LPS injection (B,E,H). LPS-injected mice that received Didox treatment beginning at 24 h post injection and continued for 5 subsequent days (LPS+Didox) displayed no change in the distal location of ankG, Nav1.6, or Kv1.2 compared to saline controls (B,E,H) demonstrating a reversal of disrupted AIS sub-domain clustering with anti-inflammatory administration. An asterisk indicates significant difference ($p < 0.05$) from saline.

Figure 2.10

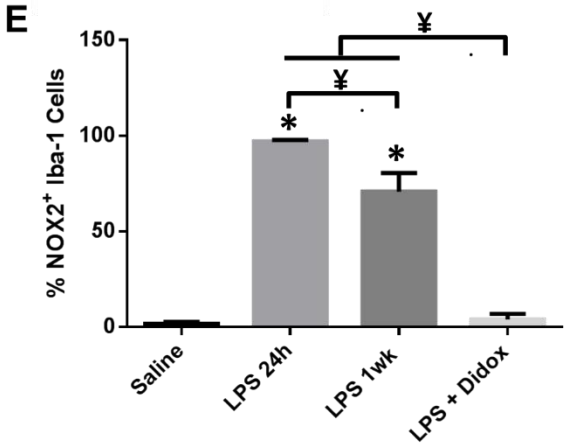
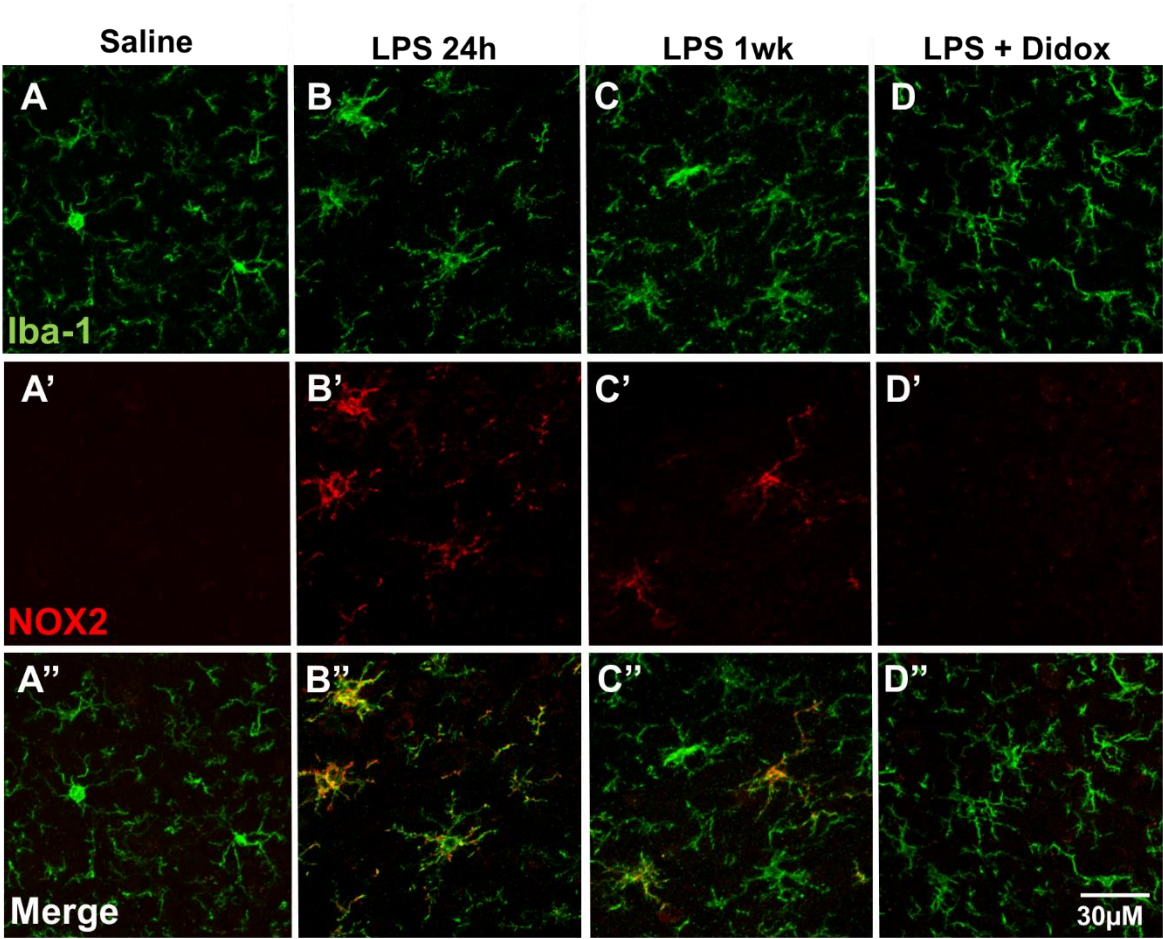


Figure 2.10. Treatment with Didox Alters Microglial NOX2 Levels. A-D, Microglia, visualized by Iba-1 immunolabeling, displayed enhanced NOX2 immunoreactivity in mice 24h (B') and 1wk (C') post LPS injection compared to control mice, which received saline only injections (A'). Anti-inflammatory Didox treatment decreased microglial NOX2 immunoreactivity (D') to saline control levels (A'). Scale bar = 30µM. E, the mean percentage ± SEM of NOX2 positive microglia in saline-, LPS-treated, and LPS+Didox mice. An asterisk indicates significant difference ($p < 0.05$) from saline, and a ¥ indicates a difference between treatment groups.

Figure 2.11

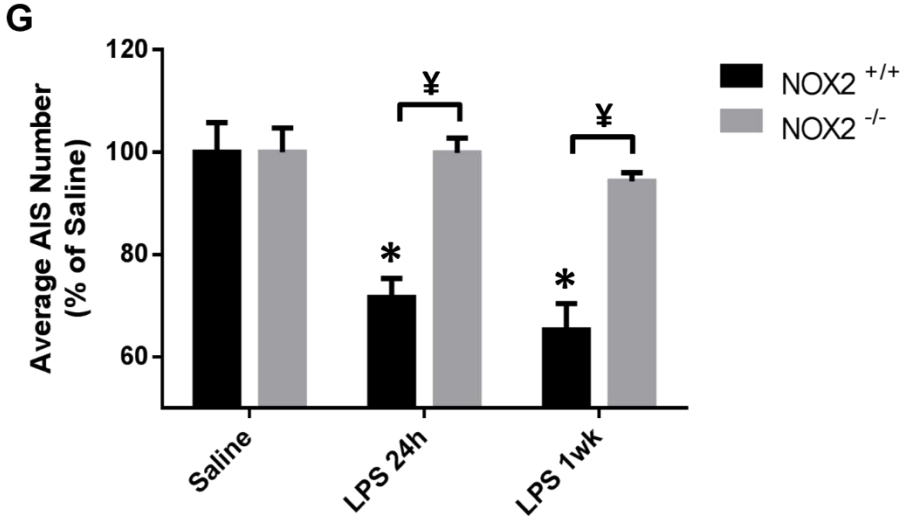
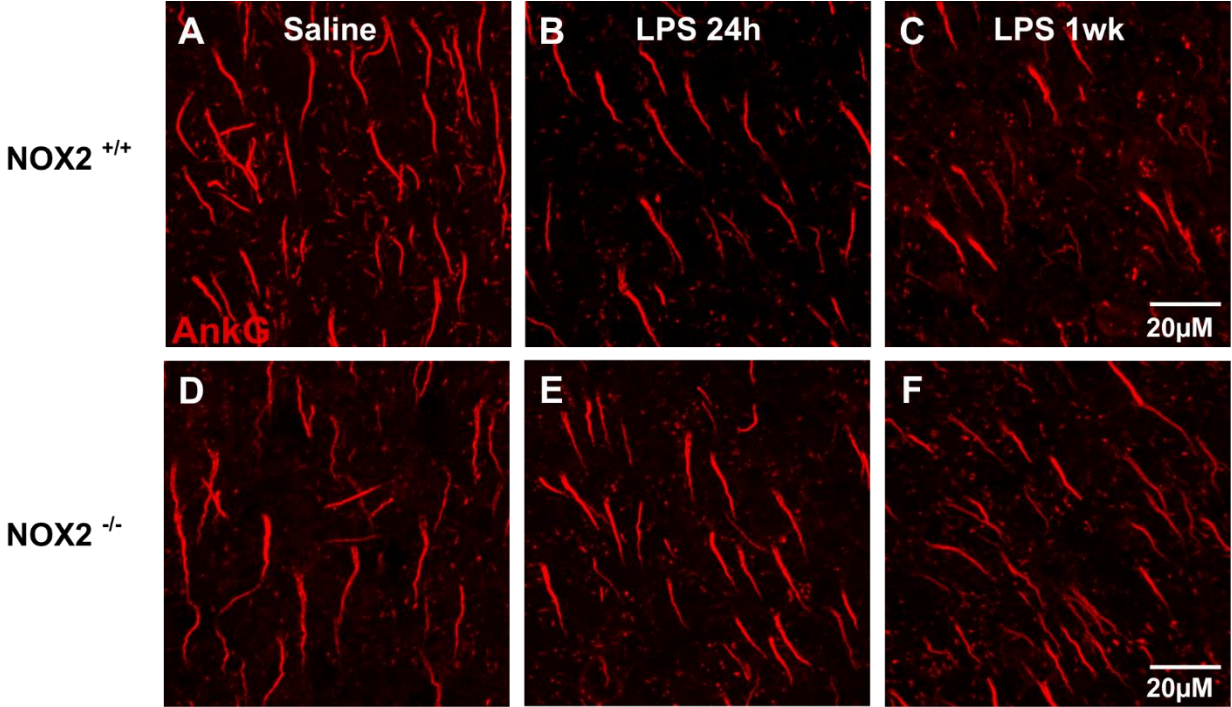


Figure 2.11. Ablation of NOX2 Prevents AIS Disruption. A-F, AISs in layer V of the cerebral cortex from NOX2^{+/+} (A-C) and NOX2^{-/-} (D-F) mice were identified by ankG immunolabeling after saline (A, D) or LPS (B-C, E-F) treatment. AISs were disrupted in LPS treated NOX2^{+/+} mice, but were preserved in LPS treated NOX2^{-/-} mice. Scale bar = 20 μ M. G, The mean \pm SEM. of AISs/FOV in NOX2^{+/+} and NOX2^{-/-} mice treated with saline or LPS as a percent of saline controls. An asterisk indicates significant difference ($p < 0.05$) from saline, and a \yen indicates a difference between genotypes.

Figure 2.12

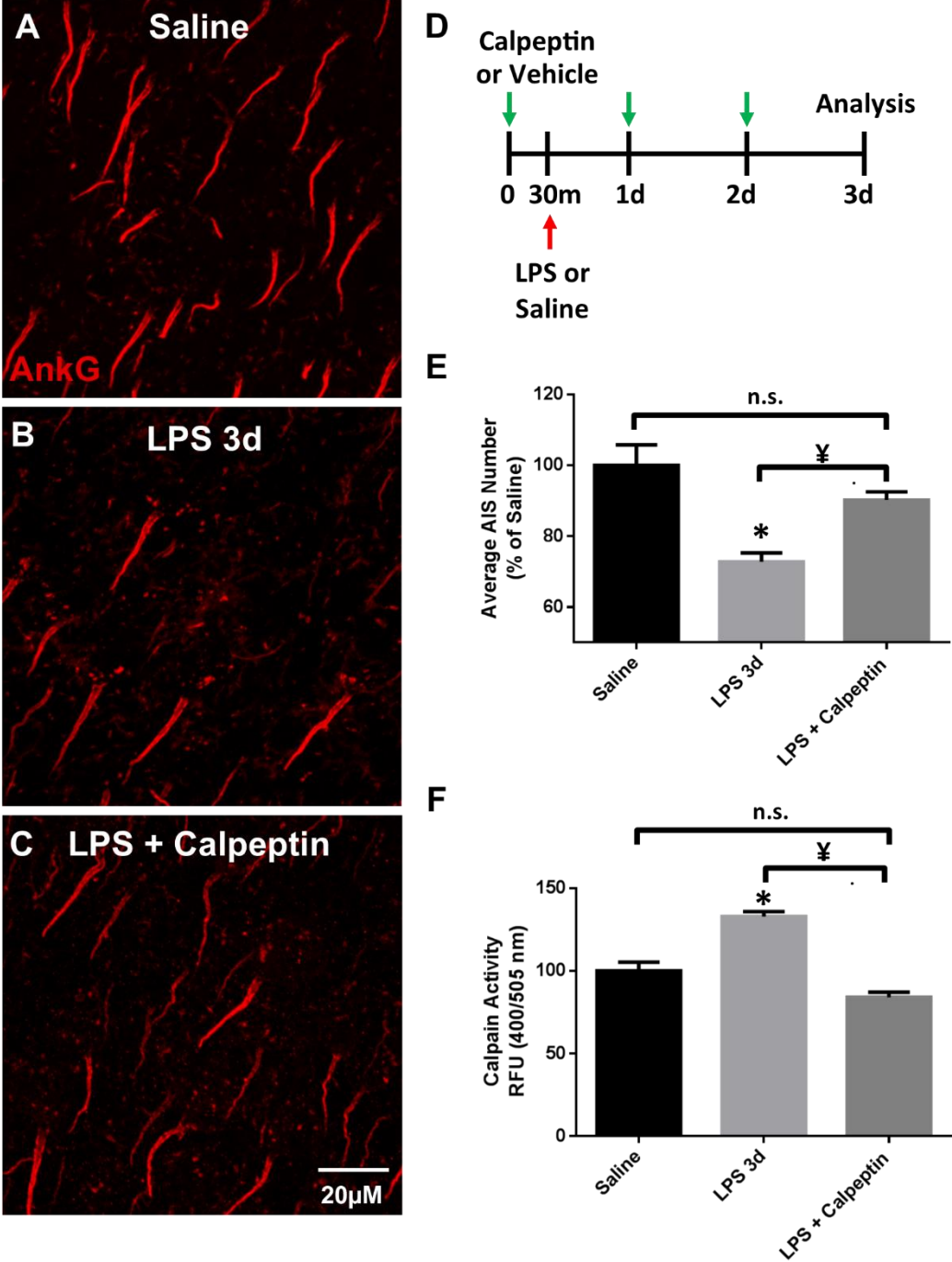


Figure 2.12. Treatment with Calpain Inhibitor Prevents AIS Disruption. A-C, AISs, immunolabeled for ankG, were reduced 3d post-LPS injection (B, E). LPS-injected mice that received Calpeptin treatment (calpain inhibitor), beginning 30min prior to LPS injection and continued once daily for 2 days (D), displayed no loss in ankG⁺ labeled AISs (C, E). Scale bar = 20 μ M. D, schematic of LPS and Calpeptin administration. E, The mean \pm SEM of AISs/FOV in saline-, LPS+vehicle, and LPS+Calpeptin mice as a percent of saline controls. F, The mean \pm SEM of calpain activity levels in relative fluorescent units in saline-, LPS+vehicle, and LPS+Calpeptin mice as a percent of saline controls. An asterisk indicates significant difference ($p < 0.05$) from saline, and a \neq indicates a difference between treatment groups.

Table 2.1. Neuronal Density and Cortical Volume Measurements from Saline and LPS-injected Mice

Treatment Group	Average NeuN Count (% Saline \pm SEM)		Average Cortical Volume \pm SEM (μm^3) $\times 10^3$	
	NOX2 ^{+/+}	NOX2 ^{-/-}	NOX2 ^{+/+}	NOX2 ^{-/-}
Saline	100% \pm 3.2	100% \pm 7.3	1.4 \pm 0.2	1.14 \pm 0.3
LPS 6h	103% \pm 5.9	-	1.1 \pm 0.2	-
LPS 24h	98% \pm 0.8	109% \pm 4.9	1.1 \pm 0.1	1.15 \pm 0.3
LPS 3d	108.1% \pm 2.5	-	1.4 \pm 0.1	-
LPS 1w	97.7% \pm 2.5	110% \pm 3.4	1.2 \pm 0.1	1.27 \pm 0.1
LPS 2w	108% \pm 3.9	-	1.5 \pm 0.1	-

Table 2.1. No significant difference was detected with regard to density of neuronal cell bodies or cortical volume among any of the treatment groups in either NOX2^{+/+} or NOX2^{-/-} mice.

Table 2.2. Oligonucleotide Primer Pairs Used for RT-qPCR

Gene	Accession #	Forward Primer	Reverse Primer
Tnfa	NM_013693.1	5'-GCCCACGTCTAGCAAACCACC-3'	5'-CCCATCGGCTGGCACCCTA-3'
COX-2 (Ptgs2)	NM_009367.1	5'-TTGCTGGCCGGTTGCTGG-3'	5'-CAGGGAGAAGCGTTTGCAGT-3'
NOX2 (Cybb)	NM_023965.1	5'-GGGAACTGGGCTGTGAATGA-3'	5'-CAGTGCTGACCCAAGGAGTT-3'
Mrc1	NM_008625.2	5'-GGCTGATTACGAGCAGTGGA-3'	5'-CATCACTCCAGGTGAACCCC-3'
Fizz-1 (Retnlb)	NM_020509.3	5'-CAGCTGATGGTCCCAGTGAAT-3'	5'-AGTGGAGGGATAGTTAGCTGG-3'
TGF- β	NM_009367.2	5'-CTCCCCTCCGAAAATGCCA-3'	5'-GTTTTGCAAGCGGAAGACCC-3'
iNOS	NM_010927.4	5'-TCCAGAATCCCTGGACAAGCTGC-3'	5'-TGCAAGTCAAATCCGATGTGGCCT-3'
Cyclophilin A	NM_008907.1	5'-CTAGAGGGCATGGATGTGGT-3'	5'-TGACATCCTTCAGTGGCTTG-3'
PGK1	NM_008828.3	5'-ATGCAAAGACTGGCCAAGCTA C-3'	5'-AGCCACAGCCTCAGCATATTTTC -3'

Table 2.3. AnkG Start and End Positions and Length Measurements

AnkG			
Treatment group	Start (μM)	End (μM)	Length (μM)
Saline	0.25 \pm 0.14	22.79 \pm 0.61	22.52 \pm 0.62
LPS 6h	0.06 \pm 0.14	20.31 \pm 0.61*	20.36 \pm 0.62*
LPS 3d	0.29 \pm 0.14	20.30 \pm 0.61*	19.87 \pm 0.62*
LPS 1wk	0.43 \pm 0.14	18.95 \pm 0.61***	18.50 \pm 0.62***
LPS 2wk	0.23 \pm 0.14	24.61 \pm 0.61	24.49 \pm 0.62*
LPS + Didox	1.07 \pm 0.14**	22.37 \pm 0.62	21.24 \pm 0.62

Table 2.3. The mean \pm SEM of ankG start and end positions relative to soma edge and overall length measurements from Saline or LPS-injected Mice. An asterisk indicates significant difference (* $p < 0.05$; ** $p < 0.01$; *** $p < 0.001$) compared to saline.

Table 2.4. Nav1.6 Start and End Positions and Length Measurements

Nav1.6			
Treatment group	Start (μM)	End (μM)	Length (μM)
Saline	1.75 \pm 1.03	22.14 \pm 0.73	20.38 \pm 1.08
LPS 6h	1.62 \pm 1.02	19.65 \pm 0.73*	18.12 \pm 1.08
LPS 3d	3.41 \pm 1.02	19.09 \pm 0.73*	15.55 \pm 1.08**
LPS 1wk	1.18 \pm 1.02	18.48 \pm 0.73**	17.30 \pm 1.08
LPS 2wk	3.72 \pm 1.02	22.97 \pm 0.73	19.37 \pm 1.08
LPS + Didox	3.23 \pm 1.03	21.69 \pm 0.74	18.38 \pm 1.08

Table 2.4. The mean \pm SEM of Nav1.6 start and end positions relative to soma edge and overall length measurements from Saline or LPS-injected Mice. An asterisk indicates significant difference (* $p < 0.05$; ** $p < 0.01$; *** $p < 0.001$) compared to saline.

Table 2.5. Kv1.2 Start and End Positions and Length Measurements

Kv1.2			
Treatment group	Start (μM)	End (μM)	Length (μM)
Saline	3.14 \pm 0.49	21.20 \pm 0.71	18.1 \pm 0.99
LPS 6h	4.02 \pm 0.49	18.90 \pm 0.71*	14.93 \pm 0.99*
LPS 3d	4.72 \pm 0.49	18.72 \pm 0.71*	14.21 \pm 1.0*
LPS 1wk	3.47 \pm 0.49	20.06 \pm 0.71	16.61 \pm 1.0
LPS 2wk	4.00 \pm 0.50	21.15 \pm 0.72	17.34 \pm 1.0
LPS + Didox	4.05 \pm 0.49	21.49 \pm 0.71	17.44 \pm 0.99

Table 2.5. The mean \pm SEM of Kv1.2 start and end positions relative to soma edge and overall length measurements from Saline or LPS-injected Mice. An asterisk indicates significant difference (**p* < 0.05; ***p* < 0.01; ****p* < 0.001) compared to saline.

Table 2.6. GO-BP enrichment analysis of 42 genes significantly up-regulated 2-fold or greater in LPS 6h mice compared to saline controls.

Functional clustering of genes up-regulated: LPS 6h vs. Saline		
<u>Term</u>	<u>%</u>	<u>Benjamini</u>
positive regulation of inflammatory response	43.9	1.8E-16
immune response	36.6	9.3E-14
cellular response to interleukin-1	29.3	5.4E-15
positive regulation of transcription from RNA polymerase II promoter	29.3	2.2E-4
response to lipopolysaccharide	26.8	1.7E-9
G-protein coupled receptor signaling pathway	26.8	3.9E-2
positive regulation of ERK1 and ERK2 cascade	24.4	2.0E-8
signal transduction	24.4	1.9E-2
chemotaxis	22.0	4.3E-10
chemokine-mediated signaling pathway	19.5	2.9E-9
cellular response to interferon-gamma	19.5	1.2E-8
cellular response to tumor necrosis factor	19.5	2.6E-7
positive regulation of apoptotic process	19.5	2.4E-4
positive regulation of cell proliferation	19.5	3.2E-3
positive regulation of NF-kappaB transcription factor activity	17.1	6.3E-6
positive regulation of GTPase activity	17.1	2.8E-5
negative regulation of cell proliferation	17.1	3.5E-3
positive regulation of gene expression	17.1	4.1E-3
positive regulation of tumor necrosis factor production	14.6	8.2E-6
cytokine-mediated signaling pathway	14.6	4.4E-4
positive regulation of cytosolic calcium ion concentration	14.6	4.5E-4
positive regulation of I-kappaB kinase/NF-kappaB signaling	14.6	4.5E-4
positive regulation of nitric oxide biosynthetic process	14.6	1.0E-5
positive regulation of interleukin-1 beta secretion	9.8	4.2E-4

Table 2.7. GO-BP enrichment analysis of 13 genes significantly down-regulated 2-fold or greater in LPS 6h mice compared to saline controls.

Functional clustering of genes down-regulated: LPS 6h vs. Sal		
<u>Term</u>	<u>%</u>	<u>Benjamini</u>
positive regulation of cell migration	25.0	7.6E-1
inflammatory response	25.0	8.6E-1
immune system process	25.0	8.0E-1
positive regulation of gene expression	25.0	7.3E-1
positive regulation of cell proliferation	25.0	8.5E-1
apoptotic process	25.0	8.2E-1
protein phosphorylation	25.0	7.8E-1
transforming growth factor beta receptor signaling pathway	16.7	4.2E-1

Table 2.8. GO-BP enrichment analysis of 17 genes significantly up-regulated 2-fold or greater in LPS 1wk mice compared to saline controls.

Functional clustering of genes up-regulated: LPS 1wk vs. Sal		
<u>Term</u>	<u>%</u>	<u>Benjamini</u>
inflammatory response	62.5	5.3E-10
positive regulation of ERK1 and ERK2 cascade	50.0	1.4E-8
immune response	43.8	2.8E-6
G-protein coupled receptor signaling pathway	43.8	2.3E-2
positive regulation of inflammatory response	37.5	1.7E-7
chemotaxis	37.5	2.1E-6
chemokine-mediated signaling pathway	31.2	5.1E-6
cellular response to interferon-gamma	31.2	1.1E-5
cellular response to interleukin-1	31.2	1.9E-5
cellular response to tumor necrosis factor	31.2	6.1E-5
positive regulation of angiogenesis	31.2	7.6E-5
positive regulation of GTPase activity	31.2	1.3E-4
positive regulation of protein phosphorylation	31.2	2.9E-4
positive regulation of gene expression	31.2	4.4E-3
lipopolysaccharide-mediated signaling pathway	25.0	6.8E-5
protein kinase B signaling	25.0	1.1E-4
monocyte chemotaxis	25.0	1.2E-4
MAPK cascade	25.0	4.9E-4
transforming growth factor beta receptor signaling pathway	25.0	4.6E-2
positive regulation of vascular endothelial growth factor production	18.8	3.1E-3
positive regulation of calcium ion transport	18.8	4.4E-3
positive regulation of cell adhesion	18.8	1.5E-2
positive regulation of tumor necrosis factor production	18.8	1.6E-2
cellular calcium ion homeostasis	18.8	3.7E-2
cytokine-mediated signaling pathway	18.8	6.5E-2

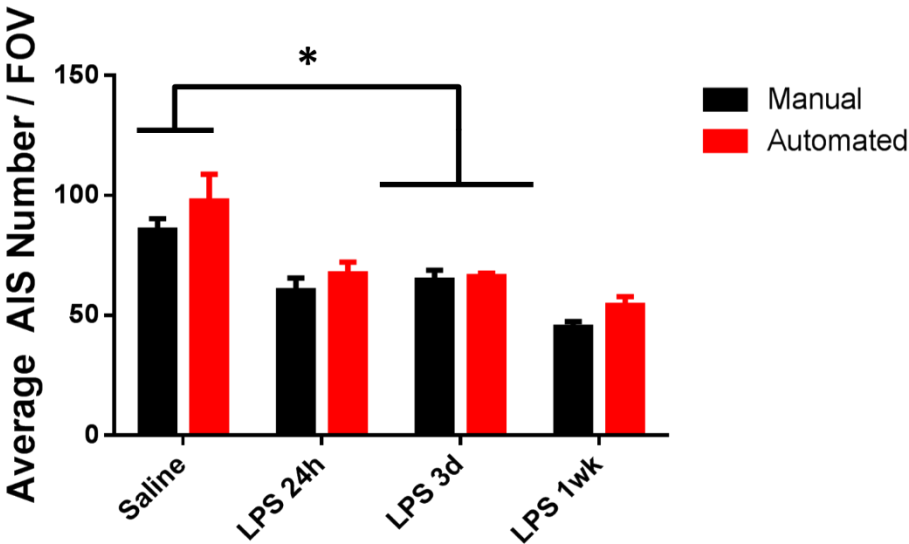
Table 2.9. GO-BP enrichment analysis of 74 genes significantly down-regulated 2-fold or greater in LPS 1wk mice compared to LPS 6h mice

Functional clustering of genes down-regulated: LPS 1wk vs. LPS 6h		
<u>Term</u>	<u>%</u>	<u>Benjamini</u>
immune response	38.7	1.60E-28
cellular response to interleukin-1	25.8	4.50E-21
positive regulation of GTPase activity	25.8	2.80E-11
positive regulation of nitric oxide biosynthetic process	25.8	2.30E-05
chemokine-mediated signaling pathway	22.6	4.70E-20
response to molecule of bacterial origin	22.6	5.10E-06
lymphocyte chemotaxis	19.4	4.50E-15
cellular response to tumor necrosis factor	19.4	3.50E-14
cellular response to interferon-beta	19.4	1.60E-05
cellular response to interferon-gamma	16.1	7.20E-17
monocyte chemotaxis	16.1	2.50E-12
positive regulation of NF-kappaB import into nucleus	16.1	2.20E-05
positive regulation of interleukin-1 beta secretion	16.1	3.80E-05
positive regulation of fever generation	16.1	4.80E-05
response to glucocorticoid	16.1	2.40E-04
positive regulation of cell adhesion	12.9	2.90E-06
positive regulation of ERK1 and ERK2 cascade	9.7	1.40E-12
positive regulation of interleukin-12 production	9.7	1.80E-06
response to cytokine	9.7	2.10E-05
positive regulation of cytosolic calcium ion concentration	9.7	4.50E-05

Table 2.10. GO-BP enrichment analysis of 32 genes significantly up-regulated 2-fold or greater in LPS 1wk mice compared to LPS 6h mice

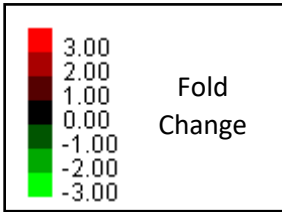
Functional clustering of genes up-regulated: LPS 1wk vs. LPS 6h		
<u>Term</u>	<u>%</u>	<u>Benjamini</u>
positive regulation of transcription from RNA polymerase II promoter	25.8	2.90E-02
protein phosphorylation	25.8	1.90E-03
signal transduction	25.8	8.40E-02
phosphorylation	22.6	1.60E-02
positive regulation of ERK1 and ERK2 cascade	22.6	1.00E-04
apoptotic process	19.4	5.90E-02
intracellular signal transduction	19.4	1.70E-02
positive regulation of gene expression	16.1	8.70E-02
positive regulation of peptidyl-tyrosine phosphorylation	16.1	1.50E-03
transforming growth factor beta receptor signaling pathway	16.1	1.00E-03
positive regulation of cell migration	12.9	8.70E-02
cellular response to transforming growth factor beta stimulus	9.7	8.60E-02
positive regulation of histone acetylation	9.7	1.70E-02

Supplementary Figure 2.1



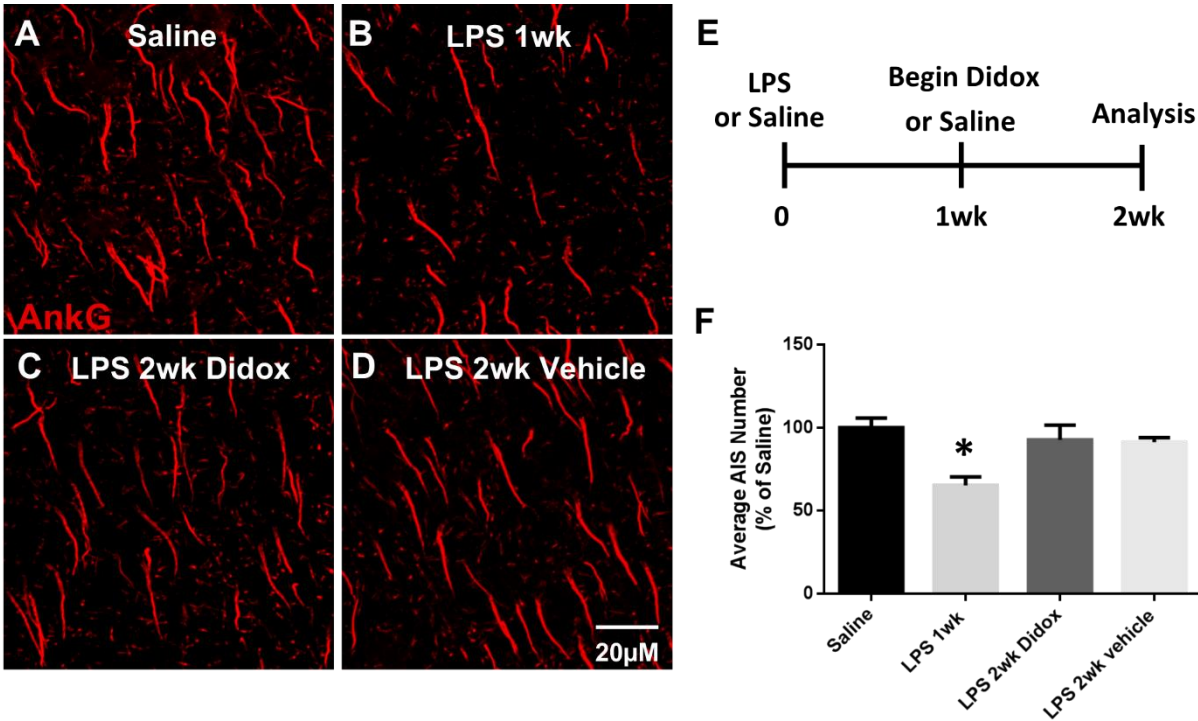
Supplementary Figure 2.1. Automated AIS Counts Using FIJI is an Accurate Method for Quantifying AISs. Method comparison of manual AIS tracings and automated AIS counts using FIJI shows no difference in AIS counts between methods. Mean \pm SEM of ankG⁺ AIS counts in saline- and LPS-injected mice. Significant treatment effects (LPS) were detected compared to saline controls ($p < 0.0001$) as expected; however, no significant difference was found between methods ($p = 0.795$).

Supplementary Figure 2.2



Supplementary Figure 2.2. Heat map of Differentially Expressed Genes in Microglia of LPS-Injected Mice. Quantitative nCounter expression profiling of 248 inflammation related genes was performed in microglia isolated from saline and LPS-injected mice. The fold change of each differentially regulated gene (rows) within each LPS group compared to saline controls (column) is presented. Each column represents the group average ($n = 3$) fold change compared to saline controls. 3 mice were pooled for each n at each time point. The relative fold change of transcripts is indicated by a color (red, higher; black, median; green, low).

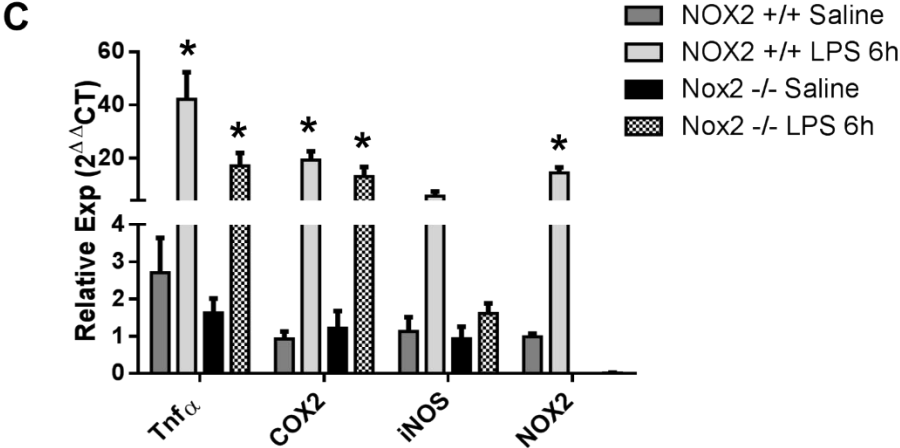
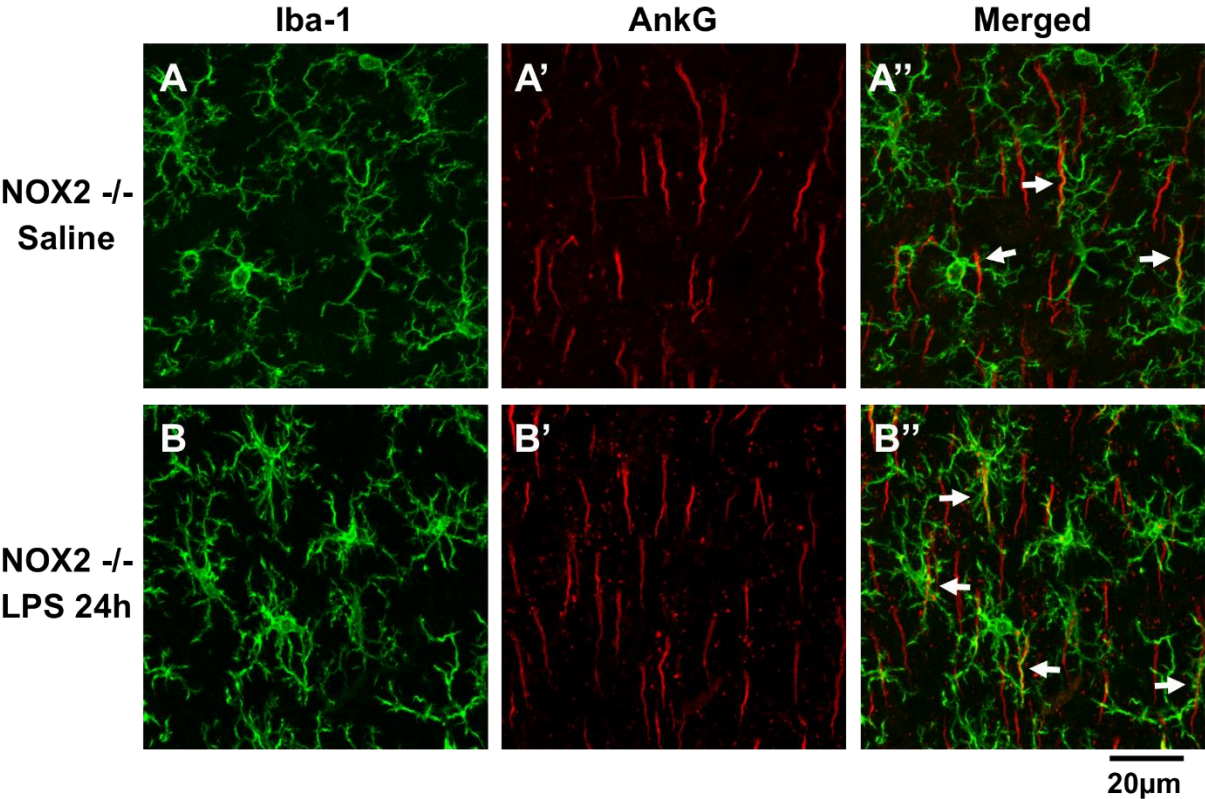
Supplementary Figure 2.3



Supplementary Figure 2.3. AISs Spontaneously Recovered 2wks post-LPS

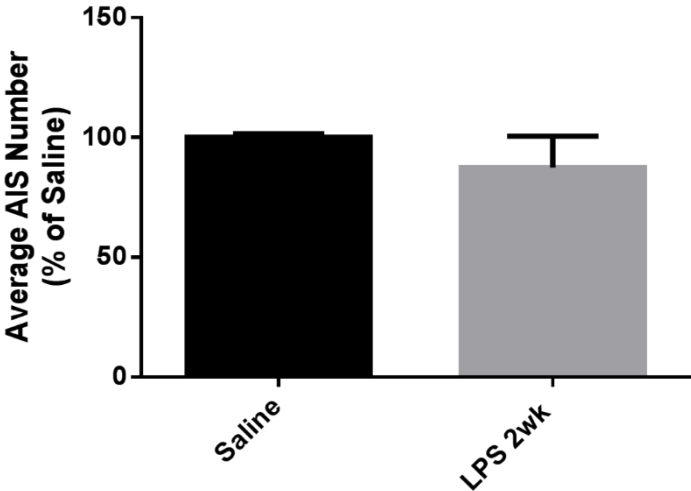
Injection. Didox paradigm was used to investigate reversibility of AIS disruption: Didox (250 mg/kg solubilized in 0.9% saline) or vehicle (0.9% saline, 10 mL/kg) was administered intraperitoneally beginning at 1 week post-LPS injection and continued for 6 days. Animals were analyzed 2 weeks post-LPS injection (E). A-D, The number of AISs, immunolabeled for ankG, was reduced through 1 week post-LPS injection (B). LPS-injected mice that received either vehicle or Didox displayed no loss in ankG⁺ AISs (C,D,F). Scale bar = 20 μ M. F, the mean \pm SEM of AISs/FOV in saline, LPS 1wk, LPS 2wk vehicle and LPS 2wk Didox mice as a percent of saline controls. An asterisk indicates significant difference ($p < 0.05$) from saline. These data revealed spontaneous AIS recovery in the LPS 2wk vehicle controls.

Supplementary Figure 2.4



Supplementary Figure 2.4. NOX2-deficient Mice Mount a Pro-inflammatory Response after LPS-Injection. A-B, Microglia, visualized by Iba-1 immunolabeling, displayed a reactive morphology in NOX2 ^{-/-} mice 24h (B) post LPS injection compared to surveying morphology present in saline injected NOX2 ^{-/-} mice (A). Microglia enhanced contact with AISs in LPS injected NOX2 ^{-/-} mice (A'',B'', white arrows). Consistent with microglial morphologies, inflammatory markers were significantly upregulated at 6 hours post LPS injection in NOX2 ^{-/-} mice compared to NOX2 ^{+/+} saline controls (C). As expected, NOX2 transcript was not amplified in NOX2 ^{-/-} mice (C). mRNA expression was evaluated by quantitative RT-PCR, values were normalized using the $2^{-\Delta\Delta CT}$ method and were reported as mean expression \pm SEM. An asterisk indicates significant difference ($p < 0.05$) from saline.

Supplementary Figure 2.5



Supplementary Figure 2.5. LPS 10mg/kg Injection Does Not Result in Sustained Disruption of AISs 2wks post-injection. Mice received a single LPS 10mg/kg or saline injection and AISs were quantified 2 weeks post-injection, a time point that showed reversibility with the lower LPS dose (5mg/kg). 8 mice were injected with LPS 10mg/kg and 3 mice were used as saline controls. 3 of the 8 LPS mice (38%) survived to the 2wk time point. No difference in AIS number was found between saline and LPS 10mg/kg mice demonstrating that an increase in initial inflammatory insult is not sufficient to prevent AIS recovery.

CHAPTER THREE

NOVEL EXPRESSION OF NEUROFASCIN IN MICROGLIA: A CANDIDATE FOR MICROGLIA-AIS INTERACTION

3.1 Abstract

Microglia dynamically interact with neurons influencing the development, structure, and function of neuronal networks. Recent studies suggest that microglia may also influence or respond to neuronal activity by directly contacting and wrapping around the axonal domain responsible for action potential initiation, the axon initial segment (AIS). The molecules that mediate this interaction, however, remain unknown. This portion of my work aimed to identify a candidate molecule that facilitates microglial-AIS contact. Here, I identify and characterize a novel isoform of the cell adhesion molecule neurofascin (Nfasc) expressed by microglia. Sequencing experiments revealed that microglial Nfasc excludes three small alternatively spliced domains in the extracellular region: 1. neuron specific sequence at the extreme N-terminus (mini-exon 6), 2. the Ig2 – Ig3 linker sequence present in Nfasc 155 of myelinating glia (exon 11), and 3. a hinge domain located between the Ig like and FNIII domains (exon 20). Microglial Nfasc also excludes the Nfasc 186 specific mucin and 5th FNIII domains while including the 3rd FNIII repeat unique to Nfasc 155. Microglial Nfasc localized to microglial processes and was enriched at the microglial-AIS interface. Furthermore, its expression is up-regulated during chronic inflammation and parallels disease severity consistent with increased contact between microglia and the AIS.

3.2 Introduction

Microglia are the innate immune cells of the CNS and play important roles in brain development, homeostasis, plasticity, and function (von Bernhardi et al., 2016b). Microglia actively survey the brain environment by extending and retracting their processes (Nimmerjahn et al., 2005), and this process can be altered by sensory experience, ATP, or neurotransmitters (Davalos et al., 2005; Fontainhas et al., 2011; Tremblay et al., 2010). Consistently, microglia respond to changes in and alter neural activity. In the zebrafish optic tectum, microglia preferentially contacted highly active neurons and after contact, these neurons decreased activity (Li et al., 2012). Furthermore, in cortical brain slices of mice, microglial processes contacted axons of hyperactive neurons induced by repetitive stimulation. After microglial contact, rapid soma membrane repolarization was detected and neuronal cell death was prevented (Kato et al., 2016). Thus, microglial-neuronal interaction is important for neuronal integrity and function.

It was recently reported that microglia also contact AISs during development and this contact is maintained throughout life implicating a role for these cells in the regulation of AIS structure and/or function in both the developing and mature CNS (Baalman et al., 2015). Moreover, our laboratory (Clark et al., 2016) showed that in the diseased state microglia-AIS contact is increased both with regard to the number of AISs contacted and the extent of contact (e.g. microglial process completely surround the AIS). Since the AIS is the axonal domain where action potentials are generated, this consistent microglial-AIS contact in both health and disease strongly implicates microglia as a regulator of neuronal function.

Molecules mediating microglia-AIS interactions remain to be identified; however, chemokine fractalkine receptor (CX3CR1) is known to mediate microglial contact with other neuronal domains (Rogers et al., 2011). Mice with fractalkine receptor CX3CR1-deficient microglia have impaired synaptic pruning and reduced functional connectivity (Paolicelli et al., 2011; Zhan et al., 2014) implicating the fractalkine receptor as not only a mediator of microglial-somal and microglial-dendritic interactions but also identified the receptor as a candidate molecule for mediating AIS interactions. However, Baalman et al. (2015) reported that the absence of microglial CX3CR1 receptors did not disrupt contact with the AIS suggesting that microglial-AIS interactions are not mediated through the fractalkine receptor. In an effort to identify AIS-specific molecules microglia are targeting, Baalman and colleagues (2015) investigated brevican and versican, members of the specialized extracellular matrix (ECM) at the AIS (Baalman et al., 2015); however, loss of the specialized ECM surrounding the AIS did not disrupt contact. These data suggest that microglial-AIS interactions are not mediated by CX3CR1 or the specialized ECM components brevican and versican, and that microglia may interact with a molecule present in the AIS membrane (Baalman et al., 2015). Consistent with microglia-AIS contact occurring through AIS membrane proteins, loss of the AIS master scaffolding protein ankG led to a significant decrease in the frequency of microglia-AIS interactions, confirming that molecules normally restricted to the AIS are important for microglia-AIS contact (Baalman et al., 2015).

In order to determine the importance of microglial-AIS contact, the molecules that mediate contact either at the AIS or on the microglia need to be identified. To identify AIS candidate proteins, one approach could be the knockout of AIS proteins; however, loss

of ankG and other AIS proteins significantly disrupts axonal and AIS identity, and consequently neuronal activity, an important component of known microglial-neuronal interactions (Davalos et al., 2005; Fontainhas et al., 2011; Kato et al., 2016; Li et al., 2012; Tremblay et al., 2010). Thus, it could be difficult to determine whether loss of interaction is due to loss of a microglial binding partner or loss of neuronal integrity. Therefore, identifying novel candidates expressed by microglia that mediate cell adhesion may provide a better approach. Candidates that mediate microglia-AIS contact should include molecules expressed by microglia and molecules involved in glial-neuronal communication. Therefore, I investigated the Nfasc cell adhesion molecule as a candidate mediator of microglia-AIS contact.

Nfasc proteins are cell adhesion molecules implicated in a wide spectrum of functions including process extension and neurite outgrowth, axonal domain maintenance, and axo-glial contact (Ango et al., 2004; Charles et al., 2002; Davis et al., 1996; Ebel et al., 2014; Hassel et al., 1997; Pruss et al., 2004; Rathjen et al., 1987; Tait et al., 2000; Zhang et al., 2015). As part of the L1 subgroup of the immunoglobulin (Ig) superfamily of cell adhesion molecules (CAMs), Nfasc contains six aminoterminal Ig-like domains, followed by five fibronectin type III (FNIII) repeats, a single-pass transmembrane region, and a short, highly conserved cytoplasmic domain (Davis et al., 1993; Hassel et al., 1997; Volkmer et al., 1992). Nfasc is expressed in a highly complex temporally- and spatially-regulated pattern, where complexity is achieved by extensive alternative splicing and posttranslational modifications. Nfasc has numerous exons that can be alternatively spliced resulting in the expression of multiple isoforms that are cell type specific (Hassel et al., 1997; Kriebel et al., 2012).

Four Nfasc polypeptides of 186, 155 high and 155 low, and 140 kDa have been described in the rodent nervous system (Davis et al., 1993; Hassel et al., 1997; Pomicter et al., 2010; Rathjen et al., 1987; Zhang et al., 2015). Neuronal isoforms 186 and 140 differ primarily in the combination of FNIII domains as well as the alternative splicing of a mucin domain. Nfasc186 is expressed mainly at the AIS and nodes of Ranvier, where it is implicated in clustering of Nav channels and stabilization of axo-axonic synapses (Desmazieres et al., 2014; Lonigro and Devaux, 2009; McEwen and Isom, 2004). Nfasc140 is targeted to the node of Ranvier and the AIS where its expression is abundant during embryonic development but declines relative to Nfasc186 in the embryo until birth (E13-P1) (Zhang et al., 2015). In Nfasc *null* mice, transgenic expression of Nfasc140 can rescue nodal complexes and restore electrophysiological function (Zhang et al., 2015) suggesting Nfasc140 may complement the function of Nfasc186 in initial stages of assembly and stabilization of the nodal complex.

To date, only one glial isoform has been characterized. Nfasc 155 is expressed by myelinating cells and is composed of the 1st – 4th FNIII domains and the Ig2 – Ig3 linker sequence (mini-exon 11) and excludes the Nfasc 186-specific mucin and 5th FNIII domains (Davis et al., 1996; Tait et al., 2000). Nfasc155 is found in oligodendrocytes and Schwann cells where it plays an important role in mediating axo-glial contact by forming paranodal septate-like junctions (Pillai et al., 2009; Sherman et al., 2005; Zonta et al., 2008). Interestingly, our laboratory identified a second Nfasc 155 form present in myelinating glia (Pomicter et al., 2010), where extended electrophoresis revealed that the initially characterized Nfasc 155 protein band actually consisted of two distinct bands. These were identified as Nfasc 155 high and Nfasc 155 low. Both Nfasc 155 forms are

expressed by myelinating cells and their expression coincides with the onset of myelination (Pillai et al., 2009; Sherman et al., 2005; Zonta et al., 2008). However, the composition and function of these two forms are yet to be defined.

The differences in expression of alternatively spliced domains among Nfasc isoforms account for distinct protein-protein interactions, and thus regulate how Nfasc isoforms exert essential functions in the nervous system. In this study, I demonstrate that microglia express a Nfasc isoform and that this isoform is unique from previously described isoforms. Sequencing experiments revealed that microglial Nfasc excludes the small alternatively spliced domains in the extracellular region (mini-exons 6, 11 and 20), the mucin and 5th FNIII domains while including the 3rd FNIII domain. IHC analysis revealed that expression of this novel Nfasc isoform localized to microglial processes and was enriched at the microglial-AIS interface. Furthermore, protein expression of microglial Nfasc was up-regulated in neuroinflammatory conditions where increased microglial-AIS contact is observed (Clark et al., 2016), consistent with the potential of microglial Nfasc mediating microglial-AIS contact.

3.3 Methods

Animals

All animals for these studies were maintained in the AAALAC accredited McGuire Veterans Affairs Medical Center (VAMC) vivarium with access to food and drink *ad libitum*. All procedures were conducted in accordance with the National Institutes of Health guidelines for the care and use of laboratory animals and were approved by the McGuire VAMC Institutional Animal Care and Use Committee.

To evaluate *Nfasc* expression in chronic inflammatory conditions (Fig. 3.1, 3.2), naïve C57BL/6J mice and C57BL/6J mice induced with experimental autoimmune encephalomyelitis (EAE) were used. The chronic model of (EAE) was induced as previously described (Clark et al., 2016; DeVries et al., 2012). Briefly, 11-12 weeks old female C57BL/6J mice were injected subcutaneously over each shoulder with 50 μ L of a solution containing 3 mg/mL myelin oligodendrocyte glycoprotein peptide 35–55 (MOG_{35–55}, MEVGWYRSPFSRVVHLYRNGK) (AnaSpec, Inc., Fremont, CA) emulsified with complete Freund's adjuvant containing 2 mg/mL of heat-killed *M. tuberculosis* (Invitrogen Life Technologies, Grand Island, NY). Mice were also injected intraperitoneal (i.p.) on the same day with 300 ng Pertussis toxin (PT) (List Biological Labs, Campbell, California) in 200 μ L phosphate buffered saline (PBS) with a booster PT injection 48 hours later. Clinical motor symptoms were scored daily and recorded as follows: 0 = no signs, 1 = limp tail, 2 = loss of righting reflex, 3 = paralysis of single hind limb and 4 = paralysis of both hind limbs. Mice achieved peak clinical symptoms at ~15 days post injection. Immunohistochemical and western blot analyses were conducted a late inflammatory time point (9 days post peak clinical symptoms; ~24 days post induction). Microglia of EAE mice with scores of 3 or 4 were pooled (3 each per *n*, *n* = 3) for western blot analysis.

For determination of *Nfasc* transcript sequence in microglia, female C57BL/6J mice purchased from Jackson Laboratories (Bar Harbor, ME) were used, and to confirm *Nfasc* gene product in microglia we used sunflower seed oil or 4-hydroxy tamoxifen (4-HT) injected *CX3CR1^{creER+/-}/Nfasc^{fl/fl}* and *CX3CR1^{creER-/-}/Nfasc^{fl/fl}* mice. We established a breeding colony of *Nfasc*-floxed mice (*Nfasc^{fl/fl}*; provided by Dr. Manzoor Bhat, University of Texas San Antonio Health Science Center, Pillai et al., 2009) mated with *CX3Cr1-cre*

estrogen receptor (ER) mice (Yona et al., 2013) (Jackson Laboratories; 020940). Using *CX3CR1^{creER+/-}/Nfasc^{fl/fl}* mice, temporal and microglia-specific ablation of *Nfasc* was induced by i.p. administration of 4-HT. 4-HT was solubilized in 100% ethyl alcohol (EtOH) to yield a 20mg/ml solution. Then 50µl of 20mg/ml 4-HT was diluted in 250µl of sunflower seed oil, emulsified, and vacuum centrifuged to evaporate the EtOH. Thus, each mouse received 1mg of 4-HT in 250ul sunflower seed oil for 3 days, skipping a day between injections 1 and 2, beginning at P14. *CX3CR1^{creER+/-}/Nfasc^{fl/fl}* mice that received sunflower seed oil-only or *CX3CR1^{creER-/-}/Nfasc^{fl/fl}* mice served as controls. Microglia were isolated 2 weeks post 4-HT administration.

To confirm cre-mediated recombination, genomic DNA was extracted from magnetic bead-CD11b isolated cells using a Qiagen DNeasy Blood and Tissue kit (Qiagen, Germantown, MD) according to manufacturer's instructions. DNA fragments spanning genomic target sites were amplified by PCR using the following primer pair: NullNfasc Forward (5' TTT ACG GTA TCG CCG CTC CCG ATT 3') NullNfasc Reverse (5' CCC TGT TCT GCT CCT GGT TCA GTC 3'). The NullNfasc Forward primer targets upstream of the first flanking loxP site and NullNfasc Reverse primer targets downstream of the second flanking loxP site, such that when recombination does not occur, the distance between these primer targets is too far to amplify. However, after cre-mediated recombination the distance between these primer target sites is shortened and a 630bp band is detected (Thaxton et al., 2011). Cycling parameters were one cycle at 94°C (3 min), 35 cycles of 94°C (30 s), 55°C (30 s), and 72°C (1 min), then 72°C (3 min), and a final hold at 4°C. PCR amplified products were analyzed by agarose gel electrophoresis.

Tissue Preparation, Immunohistochemistry, and Imaging

Mice were deeply anesthetized using 0.016 mL/gm body weight of a 2.5% solution of avertin (2, 2, 2 tribromoethanol; Sigma-Aldrich; St. Louis, MO) in 0.9% sodium chloride (Sigma-Aldrich), and transcardially perfused with 4% paraformaldehyde (Ted Pella, Redding, CA) (Benusa et al., 2017; Clark et al., 2016; Dupree et al., 1999). Following perfusion, brains were removed and immersed in 0.1 M PBS containing 30% sucrose for 48h and frozen in Optimal Cutting Temperature compound (Sakura, Tokyo, Japan). Brains were serially sectioned into 40µm thick coronal sections spanning 1.1mm anterior to Bregma to 2.5mm posterior to Bregma using a Leica CM 1850 cryostat. Fifteen sets of six sections were collected and placed on ProbeOn Plus slides (Fisher Scientific, Loughborough, UK) and stored at -80°C.

Sections were immunostained using the following antibodies: mouse monoclonal anti-ankyrin G (AnkG; NeuroMab, Davis, CA; N106/36, 1:500), rabbit polyclonal anti-Iba1 (Wako Chemicals, Richmond, VA; 019-19741; 1:1,000), and rat anti-pan-Nfasc (gift of Dr. Manzoor Bhat, UTSA HSC; 1:200). All secondary antibodies were obtained from Invitrogen Life Technologies (Grand Island, NY; Alexa™ Fluor) and used at a dilution of 1:500. Immunolabeling was performed as previously described (Clark et al., 2016; Dupree et al., 1999; Pomicter et al., 2010) with some modifications: 0.5% Triton X-100 and 10mM sodium-citrate buffer oven retrieval (30 minutes at 80°C) was used for antigen retrieval. Nuclei were stained with BisBenzimide (Sigma-Aldrich, 1:1000). Slides were mounted with Vectashield™ (Vector Laboratories, Burlingame, CA); and imaged using confocal microscopy.

Imaging was performed on a Zeiss LSM 710 confocal laser scanning microscope (Carl Zeiss Microscopy, LLC, Thornwood, NY) housed in the VCU Department of Anatomy and Neurobiology Microscopy Facility. Images were collected as previously described (Benusa et al., 2017; Clark et al., 2016). Briefly, confocal z-stacks spanning an optical thickness of 25 μ m, using a pinhole of 1 Airy disc unit and Nyquist sampling (optical slice thickness, 0.48 μ m) were collected from neocortical layer V. Images were collected using single channel acquisition in a sequential fashion (3 pass, sequential). Furthermore, AlexaTM Fluor 488 anti-rat secondary was used to detect Nfasc; AlexaTM Fluor 568 anti-mouse IgG2a was used to detect ankG; and AlexaTM Fluor 647 anti-rabbit was used to detect Iba-1. Co-localization of Nfasc⁺Iba-1⁺ microglia with ankG⁺ AISs was confirmed using VolocityTM 3D Image Analysis Software version 6.3.

Western blot analysis

Western blot analysis was performed as previously described (Pomicter et al., 2010). Briefly, whole brain or FACS-isolated microglia were homogenized in ice-cold RIPA buffer (1% Nonidet P-40, 0.5% Sodium Deoxycholate, 0.1% SDS, 98.4% 1X PBS) including Proteinase Inhibitor Cocktail (10 μ l/ml, ThermoFisher, Rockford, IL). Homogenates were centrifuged for 10 min at 600 x *g* at 4°C. Supernatant concentrations were determined using the Micro BCA Protein Assay Kit (Pierce, Rockford, IL, USA). 5 μ g of whole brain homogenate or 20 μ g of microglial isolate in Laemmli sample buffer (BioRad, Hercules, CA, USA) containing 5% β -mercaptoethanol were subjected to SDS–polyacrylamide gel electrophoresis for 30min at 70V followed by 180V using 4-15% gels (BioRad) and transferred to methanol-activated Immobilon-P PVDF membrane (EMD

Millipore) for 2h at 100V. The membranes were then blocked with 5% non-fat dry milk (Bio-Rad) in PBS containing 0.05% Tween 20 (Sigma-Aldrich) prior to incubation with primary and secondary antibodies horseradish peroxidase (HRP)-conjugated, Sigma-Aldrich), and the same solution was utilized for antibody incubations. Primary antibodies to detect pan-Nfasc (FIGQY, rabbit polyclonal, 1:1,000, gift of Dr. Matt Rasband (Ogawa et al., 2006) and GAPDH (mouse monoclonal, 1:10,000, EMD Millipore-MAB374) were used. Immunoreactive bands were visualized with HRP chemiluminescent substrate (EMD Millipore, Billerica, MA, USA) using a ChemiDoc detection system (BioRad). Quantitation of Nfasc protein band density in microglial samples was performed using FIJI. Densitometry was quantified using the 3 prominent Nfasc protein bands as a ratio of the GAPDH protein band for each microglial sample. Data are presented as percent of naïve microglia.

CD11b magnetic bead isolation

Adult cortical microglia were isolated using MACS magnetic bead separation (Miltenyi Biotec, San Diego, CA) as described above (Chapter 2, page 132). Briefly, 4-HT or sunflower injected *CX3CR1^{creER/+}/Nfasc^{fl/fl}* mice were deeply anesthetized with 2.5% avertin and transcardially perfused with 50mL ice-cold PBS. After removal of the meninges, cerebral cortices of each mouse was harvested and suspended in Hank's Balanced Salt Solution (HBSS) without CaCl₂ and MgCl₂ (Corning, Corning, NY). A single-cell suspension was prepared using the Miltenyi Neural Tissue Dissociation Kit according to manufacturer's instructions. The cell solution was depleted of myelin by suspension in 3 mL of 30% isotonic Percoll™ (GE Healthcare Life Sciences, Pittsburgh,

PA) followed by a 10 min centrifugation at 700 x *g* at 4°C. The cell pellet was washed in 5 mL HBSS without CaCl₂ and MgCl₂ and isolation of microglia was performed with magnetic CD11b microbeads (Miltenyi) and MACS magnetic separator (Miltenyi) according to manufacturer's instructions.

FACS isolation of microglia and macrophages

Mice were deeply anesthetized with 2.5% avertin and transcardially perfused with 50mL ice-cold PBS. After removal of the meninges, cerebral cortices of each mouse was harvested and suspended in HBSS without CaCl₂ and MgCl₂ (Corning). A single-cell suspension was prepared using the Miltenyi Neural Tissue Dissociation Kit according to manufacturer's instructions. The cell solution was depleted of myelin by suspension in 3mL of 30% isotonic Percoll™ (GE Healthcare Life Sciences, Pittsburgh, PA) followed by a 10 min centrifugation at 700 x *g* at 4°C. The cell pellet was washed with cold wash buffer (0.5% BSA, 2mM EDTA in PBS) and cells were incubated for 5min, at 4°C with 5µL Mouse Fc Receptor Block (CD16/CD32; BD Pharmingen, San Diego, CA) followed by a 20min incubation at 4°C in the dark with APC-conjugated anti-mouse CD11b (ThermoFisher, 17-0112-81) and BB515-conjugated anti-mouse CD45 (BD Biosciences-564590, San Diego, CA) or APC-conjugated rat IgG2b κ isotype (ThermoFisher, 17-4031-81) and BB515-conjugated rat IgG2b κ isotype (BD Biosciences, 564421) . Cell viability was determined using Zombie Violet™ staining (BioLegend, 423113, San Diego, CA). Cells were washed and resuspended in cold wash buffer and passed through a 40µm filter and then through a BD FACSAria II flow cytometer (BD Biosciences). Gates were demarcated to sort CD11b⁺/CD45^{hi} (macrophages) and CD11b⁺/CD45^{lo} (microglia) cells. Cells were

suspended in either protein lysis buffer (RIPA, western blot analysis) or RNA extraction buffer (Qiagen RNeasy kit, sequencing or qPCR analysis).

RNA extraction

Total RNA was extracted from FACS-isolated microglia using a Qiagen RNeasy mini kit (Qiagen) and treated with Ambion DNase I (Invitrogen Life Technologies, Grand Island, NY) ($n=3$ samples per experimental group). RNA concentrations were determined using a NanoPhotometer (Implen, Los Angeles, CA) and purity was assessed by the ratio of absorbance at 260 and 280nm ($OD_{260/280} > 1.8$). Oligo-dT-primed cDNAs were synthesized from 50 ng of RNA for each sample using the Sensiscript RT Kit (Qiagen) according to the manufacturer's guidelines. Samples with no reverse transcriptase added served as controls.

PCR analysis

Gene-specific primers were designed and checked for specificity using National Center for Biotechnology Information/Primer-BLAST (basic local alignment search tool; (Ye et al., 2012) (Primer sequences are presented in Table 3.1). Some primers (as indicated in Table 3.1) were previously published (Basak et al., 2007; Bennett et al., 2016); specificities for these primers were also confirmed using NCBI-BLAST. Additional primers were generated by Integrated DNA Technologies (San Diego, CA).

RT-qPCR reactions with at least two technical replicates per sample were performed on a CFX96 real-time PCR detection system (BioRad) using 1 μ L of cDNA,

SsoFast Evagreen Supermix (BioRad), and forward and reverse primers (500nM). Cycling parameters were one cycle at 95°C (5 min), 40 cycles of 95°C (5 s) and 56°C (5 s) followed by a melt curve measurement consisting of 5s 0.5°C incremental increases from 65°C to 95°C. Relative changes in gene expression were calculated by the $2^{-\Delta\Delta Ct}$ method (Livak and Schmittgen, 2001) using cyclophilin A and PGK1 as internal reference controls.

End-point PCR reactions were performed on a Veriti™ 96-well thermal cycler (Applied Biosystems, Foster City, CA) using 4μL of cDNA, Platinum™ Taq DNA Polymerase (Invitrogen), dNTP mix (0.2mM each, ThermoFisher), and forward and reverse primers (0.2μM). Cycling parameters were one cycle at 94°C (2 min), 40 cycles of 94°C (30 s), 56°C (30 s), and 72°C (1 min), and a final hold at 4°C. PCR amplified products were analyzed by agarose gel electrophoresis. For sequencing, each amplified product was excised and DNA was extracted using the QIAquick Gel Extraction Kit (Qiagen) according to manufacturer's instructions. Gel-purified products (25ng/μl) were commercially sequenced by GenScript (Piscataway, NJ).

Sequence analysis

Sequences of microglial Nfasc products were analyzed via VectorNTI advanced software (ThermoFisher). Chromatogram data files were loaded, processed, and assembled to create a contiguous sequence. Sequences of multiple microglial sample replicates were analyzed to ensure specificity of sequencing results and to create the finished microglial Nfasc consensus sequence. The consensus sequence for microglial

Nfasc was translated and the protein-coding region was identified using VectorNTI, then using AlignX, microglial Nfasc was aligned with published sequences of Nfasc variants 1-4 from NCBI (Accession numbers: NM_182716.4, NM_001160316.1, NM_001160317.1, NM_001160318.1).

Statistical analysis

Graphing and statistical analyses were performed using GraphPad Prism version 6.03 (GraphPad Software, San Diego, CA). Data were analyzed by a Student's t test or one-way analysis of variance and where mean differences were significant, assessed using Tukey's Honest Significance Difference post hoc analysis. Treatment groups were presented as percent of control (% Control \pm SEM) and $p < 0.05$ was considered statistically significant.

3.4 Results

Nfasc is expressed in Microglia and Clusters at the Microglia-AIS Interface

Microglia make direct contact with the AIS during development and throughout adulthood (Baalman et al., 2015). Furthermore, our laboratory found that this contact is enhanced during chronic inflammation consistent with AIS disruption suggesting an important interaction in regulating AIS stability (Clark et al., 2016). In order to elucidate the significance of this interaction, the ultimate goal is to inhibit contact and quantitatively assess the consequence on AIS structure and function. To this end, the first step is to identify candidate molecules that potentially mediate this interaction, which defines the

goal of this portion of my work. I determined that the neurofascin family of proteins exhibit criteria that candidate molecules would need to exhibit including glial cell expression and mediators of glial-neuronal interactions (Kriebel et al., 2012). Additionally, the neurofascin family presents with multiple isoforms that are cell type specific (Zonta et al., 2008), which is consistent with the possibility that microglia may express a novel isoform. Therefore, to determine if a Nfasc isoform is expressed in microglia and has the potential to regulate microglial-AIS contact during chronic inflammation, cortical brain sections from EAE-induced mice were triple immunolabeled for the AIS (ankG, red), microglia (Iba-1, green), and Nfasc (white) (Fig. 3.1). I used a pan-Nfasc antibody targeting the c-terminal domain that is highly conserved among Nfasc isoforms. IHC analysis revealed that microglia (Fig. 3.1 A-B', Iba-1⁺ cells, green) label robustly for Nfasc (Fig. 3.1 A-B'', grey) and this labeling is enhanced in microglial processes and clusters at the AIS interface (Fig. 3.1 A-B''', merged, white arrows, inset). These data suggest that Nfasc is expressed in reactive microglia and clusters at the point of contact between microglia and the AIS.

Microglial Nfasc is Up-regulated in Neuroinflammation

Our laboratory demonstrated that microglial-AIS contact is enhanced with microglial reactivity and disease progression in the chronic neuroinflammatory model EAE (Clark et al., 2016). Not only was the amount of microglial contact increased, but the type of contact was enhanced with reactive microglia frequently aligning along the entire domain and often surrounding the AIS coinciding with disease severity (Clark et al., 2016). To determine if expression of microglial Nfasc coincides with disease progression, IHC and western blot analyses were employed (Fig. 3.2). IHC analysis revealed Nfasc

immunoreactivity (C-term, gift of Dr. Bhat) was weakly detected in microglia of Naïve mice (Fig. 3.2 A-A'), but greatly enhanced in microglia of EAE-induced mice (Fig. 3.2 B-B'), where labeling was observed in the cell bodies and peripheral processes (Fig. 3.2 B', arrows). Western blot analysis using a second pan-Nfasc antibody targeting the conserved cytoplasmic domain (FIGQY, gift of Dr. Rasband) revealed three Nfasc isoforms in whole brain homogenate (5µg) (Fig. 3.2C, lane 1): Nfasc186 (neuron specific), Nfasc155 (myelin specific), and Nfasc140 (immature neuron specific) (Collinson et al., 1998; Davis et al., 1993; Hassel et al., 1997; Zhang et al., 2015; Zonta et al., 2008). Homogenates (20µg) of isolated microglia from cortices of Naïve and EAE mice revealed three Nfasc bands of unique molecular weights that displayed increased density corresponding with disease (Fig. 3.2C, lanes 2-5). Densitometric analysis was used to determine if Nfasc expression was up-regulated in EAE (Fig. 3.2D). The calculated intensities of the three prominent bands present in microglial isolates were combined and normalized to GAPDH demonstrating a significant increase in microglial Nfasc during neuroinflammation ($149.9\% \pm 16.24$ EAE versus $100\% \pm 6.1$ naïve, $n=3$, $p < 0.05$, Fig. 3.2D).

Microglia Express Nfasc mRNA and contain Nfasc binding domains Ig 5 and 6

Western blot analysis revealed that Nfasc protein is present in cortical microglial isolates; however, to confirm that Nfasc protein was not due to phagocytosis and to confirm that microglia express Nfasc mRNA, I amplified primer pairs designed to target two conserved Nfasc domains (Fig. 3.3). Two primer sets were designed against the highly conserved cytoplasmic domain (Fig. 3.3A, red arrows) and a primer set

encompassing the Ig-like 5 and 6 domains (Fig. 3.3A, blue arrows), which play a role in Nfasc homophilic binding (Itoh et al., 2004; Thaxton et al., 2010). PCR amplification of cDNA isolated from microglia revealed the presence of both cytoplasmic and Ig-like domains of Nfasc (Fig. 3.3 B,C, respectively). To confirm that Nfasc detection was not due to cell contamination in the microglial isolates (such as neurons or oligodendrocytes) or amplification of other L1 family members expressed by microglia, I employed microglial *Nfasc null* mice. *CX3CR1^{creER+/-}/Nfasc^{fl/fl}* mice were injected with 4-HT to induce cre-mediated recombination of the loxP flanked Nfasc sequence in CX3CR1⁺ cells (microglia). *CX3CR1^{creER+/-}/Nfasc^{fl/fl}* mice injected with sunflower seed oil (vehicle) served as controls. Using previously published primers designed to amplify a 630bp Nfasc product, which is only amplified after cre-mediated recombination (Thaxton et al., 2011), PCR amplification revealed that recombination of the *Nfasc* allele took place in CX3CR1⁺ cells (microglia) in 4HT-injected mice, but not in sunflower controls or cre-negative (*CX3CR1^{creER-/-}/Nfasc^{fl/fl}*) mice (Fig. 3.3 D). qPCR analysis of cDNA isolated from microglia of 4-HT- or sunflower-injected *CX3CR1^{creER+/-}/Nfasc^{fl/fl}* or cre-negative (*CX3CR1^{creER-/-}/Nfasc^{fl/fl}*) mice demonstrated reduced Nfasc mRNA levels in 4-HT-injected microglia (28.02% ± 6.9) versus sunflower controls (132.9% ± 12.7, n=3, *p* < 0.01) (Fig. 3.3 E). No difference was detected between cre-negative and sunflower-injected *CX3CR1^{creER+/-}/Nfasc^{fl/fl}* mice (100% ± 4.3 vs. 132.9% ± 12.7, *p* = 0.16) (Fig. 3.3 E). These data confirm the presence of a *Nfasc* gene product in microglia and that microglial Nfasc isoform(s) contain highly conserved domains and domains implicated in Nfasc binding.

Microglial Nfasc maintains conserved FNIII and cytoplasmic domains and excludes the alternatively spliced mucin and 5th FNIII domain

Western blot analysis revealed that microglia express Nfasc bands of unique molecular weights (Fig. 3.2C). In an effort to determine if microglial Nfasc isoform(s) is unique from major known isoforms, I employed RT-qPCR techniques. Nfasc has numerous alternatively spliced domains (Fig. 3.4A, grey diagonal squares) generating numerous cell-specific isoforms, which differ mainly in the alternative expression of the various fibronectin type III domains (Fig. 3.4A, F). Primers were designed against both conserved and alternatively spliced FNIII domains (Fig. 3.4A, black arrows). RT-qPCR analysis using homogenates from whole brain, isolated oligodendrocytes, and isolated microglia, revealed that, as expected, oligodendrocytes expressed the 3rd FNIII repeat (Fig. 3.4B) but did not express the mucin domain or the 5th FNIII repeat (Fig. 3.4C,D), which are domains specific for the neuron-associated isoform (Nfasc 186). However, all three domains were present in the whole brain homogenate (Fig. 3.4B-D). Interestingly, microglia also did not express the mucin domain or the 5th FNIII repeat (Fig. 3.4C,D), but did contain the 3rd FNIII repeat (Fig. 3.4B,E) and the conserved FNIII 1st, 2nd, and 4th repeats (Fig. 3.4E). These data suggest that microglial Nfasc has a similar domain composition in the FNIII domain region compared to Nfasc 155 expressed by oligodendrocytes (Fig. 3.4F).

Microglial Nfasc transcript is unique from Nfasc 186 and Nfasc 155

FNIII domain analysis revealed that microglial Nfasc has similar composition to Nfasc 155. However, to determine if the remaining ectodomain of the microglial Nfasc transcript is also similar to Nfasc 155, I amplified and sequenced the microglial Nfasc transcript. Primers were designed targeting ~300-1000bp regions specific to the *Nfasc* gene in stepwise fashion that overlapped by at least 100bp. PCR amplified products were subjected to agarose gel electrophoresis (Fig. 3.5B-G) and purified for DNA sequencing. These experiments revealed that microglia express Nfasc products of similar size to Nfasc 186 (neurons) and Nfasc 155 (oligodendrocytes) in exons 7-9 and exons 13-17 (Fig. 3.5B, E, respectively). For exons 8-15 (Fig. 3.5B), Nfasc appears slightly larger in oligodendrocytes than in neurons or microglia suggesting that microglia exclude an exon that is maintained in oligodendrocytes. This finding is consistent with published sequences demonstrating oligodendrocytes (Nfasc 155) maintain exon 11 whereas neurons do not (Nfasc 186) (Davis et al., 1996; Tait et al., 2000). Likewise, microglia exhibit a smaller PCR product for exons 15-21 (Fig. 3.5C). PCR primer sets, which targeted exon 30, were not amplified in oligodendrocytes or microglia, further confirming the absence of the mucin and 5th FNIII domain in these cell types (Fig. 3.5G). A primer set that spans exons 27-36 demonstrated that, as expected, microglia exhibit a PCR product of similar size to oligodendrocytes (Fig. 3.5D). Interestingly, two other amplified products were detected in microglial samples (Fig. 3.5D). These bands were sequenced and were also determined to be Nfasc products. For exons 19-27 (Fig. 3.5F), Nfasc appears larger in microglia than oligodendrocytes, however, sequencing did not reveal differences in the amplified targets.

Using VectorNTI software, the nucleotide sequences were processed and a contiguous nucleotide sequence for microglial *Nfasc* was obtained and the amino acid sequence translated. Sequence alignment with the NCBI published sequences of major *Nfasc* isoforms (*Nfasc* 186, *Nfasc* 155, and unidentified variant 4) revealed that, indeed, microglia express a specific *Nfasc* transcript (Fig. 3.5H, partial sequence and Supp. Fig. 3.1, full sequence) and while it has similarity to the known isoforms (Fig. 3.5 H, yellow regions), it exhibits a unique sequence compared to *Nfasc* 186 and *Nfasc* 155 (Fig. 3.5 H, blue region). This unique exclusion corresponded with the sequence of exon 20 (45 bp, amino acids 629-643) demonstrating that microglia express a unique *Nfasc* isoform that excludes alternatively spliced hinge domains in the N-terminal region, the mucin and the 5th FNIII domain, but includes the 3rd FNIII repeat (Fig. 3.6). The inclusion/exclusion of the *Nfasc* domains was further confirmed using qPCR analysis utilizing microglial *Nfasc* null mice (Fig. 3.7). RT-qPCR of isolated microglia of 4-HT or sunflower injected *CX3CR1^{creER+/-}/Nfasc^{fl/fl}* mice revealed reduced *Nfasc* cytoplasmic (Fig. 3.7A, mean difference 0.49 ± 0.11 , $p < 0.05$), 1st FNIII (Fig. 3.7B, mean difference 0.60 ± 0.14 , $p < 0.05$), and 3rd FNIII (Fig. 3.7C, mean difference 0.61 ± 0.03 , $p < 0.05$) mRNA levels in 4-HT-injected microglia versus sunflower controls demonstrating that these domains are present in microglial *Nfasc* and were diminished in the microglial-specific *Nfasc* knockout mouse.

Microglial *Nfasc* protein is not reduced 45 days after 4HT induction

PCR analysis of microglia of 4-HT- or sunflower-injected *CX3CR1^{creER+/-}/Nfasc^{fl/fl}* mice confirmed *Nfasc* gene recombination and *Nfasc* mRNA reduction in microglia of 4-

HT-injected mice (Fig. 3.3); therefore, to determine if Nfasc protein levels were also reduced, western blot analysis was used. Western blot analysis using the pan-Nfasc FIGQY antibody revealed Nfasc bands in isolated microglia from cortices of sunflower-injected mice (Fig. 3.8A, lane 1), and these bands were not diminished 30 days post-4-HT induction in 4-HT-injected mice (Fig. 3.8A, lane 2). Conditional ablation of Nfasc 155 revealed that Nfasc 155 protein levels are not significantly reduced, however, until 40 days post-tamoxifen induction (Pillai et al., 2009). Therefore, we investigated microglial Nfasc protein levels 45 days post-4HT induction and found that Nfasc protein was not diminished in microglia from 4-HT-injected *CX3CR1^{creER+/-}/Nfasc^{fl/fl}* mice (Fig. 3.8B). Both *Nfasc* gene recombination (Fig. 3.8C) and reduced Nfasc mRNA levels (Fig. 3.8C) were detected at 45 days post-4-HT induction, however, demonstrating that persistent Nfasc protein levels was not due to lack of cre-recombination.

3.5 Discussion

Microglia interact with the AIS beginning early in development and throughout adulthood (Baalman et al., 2015) and this interaction is enhanced during neuroinflammatory conditions (Clark et al., 2016) suggesting an important interaction in regulating AIS stability. The cell adhesion molecule Nfasc and its various isoforms are important for regulating axonal domain stability as well as regulating axo-glia interactions (Hedstrom and Rasband, 2006; Sherman et al., 2005; Zonta et al., 2008). In this study, we utilized IHC, PCR, and western blot analyses and determined that a unique isoform of the cell adhesion molecule Nfasc is expressed by microglia, and employed conditional ablation strategies of Nfasc in microglia to validate these novel findings. Furthermore, I

identified microglial Nfasc as a candidate molecule that may regulate the interaction between microglia and the AIS.

Microglial Nfasc Contains Conserved Ig Binding Domains: Implications for Homophilic Binding

Sequence analysis revealed that conserved Ig domains essential for protein binding are present in microglial Nfasc (Fig. 3.3, 3.6). Ig domains are important for mediating interactions of Nfasc and other L1 family CAMs (Itoh et al., 2004; Liu et al., 2011; Thaxton et al., 2010) and analysis of Ig domain conformation suggested that these proteins could preferentially interact in a homophilic manner (i.e. with other L1 family CAMs). The crystallized structure of Nfasc 155 Ig 1-4 domains revealed that Nfasc exists in a horseshoe conformation (Liu et al., 2011) similar to that reported for L1CAM and L1 homologs (Hall et al., 2000; Schürmann et al., 2001; Wei and Ryu, 2012). In this conformation the first and second Ig domains (Ig1 and Ig2) fold back to interact with the fourth and third Ig domains (Ig4 and Ig3), respectively. The authors predicted that homophilic interactions occur through a dimeric interaction between the edges of Ig2 domains with a perpendicular association between the edges of Ig 2 and 3 domains (Liu et al., 2011). While the horseshoe conformation was determined using Nfasc155, the high degree of conservation of the Ig like domains among Nfasc isoforms suggests that other Nfasc isoforms likely exhibit this conformation as well. Furthermore, due to the strength of the interaction that was measured between Ig domains in the horseshoe structure, the authors proposed that other L1 CAMs likely exist in the horseshoe conformation instead of the previously proposed extended conformation (Schürmann et al., 2001). If this is true,

the authors suggest that this would increase the likelihood of homophilic interactions among L1 family molecules (Liu et al., 2011). Indeed, this has been shown for Nfasc, NrCAM and L1CAM (Desmazieres et al., 2014; Feinberg et al., 2010; Labasque et al., 2011; Lambert et al., 1997; McEwen and Isom, 2004; Ogawa et al., 2006; Ratcliffe et al., 2001; Volkmer et al., 1996). Interestingly, NrCAM and Nfasc186, which are potential binding partners of microglial Nfasc, are clustered at the AIS.

While studies have shown that the first four Ig domains participate in the horseshoe structure and potentially in homophilic binding, other studies have revealed that the Ig5 and 6 domains are also important for mediating homophilic adhesion. Deletion of Ig6 in mice interfered with L1CAM homophilic binding (Itoh et al., 2004) and knockout of Ig5 and 6 domains in Nfasc 155 in mice resulted in a lack of paranodal septate junctions and juxtaparanode disruption mimicking the total loss of Nfasc155 (Thaxton et al., 2010). These data demonstrate that while the horseshoe region may be important for homophilic interactions, it is not the only region involved. Nevertheless, microglial Nfasc contains all 6 Ig like domains implicating L1 family molecules as potential binding partners.

Microglial Nfasc excludes the Ig2-Ig3 linker sequence: Implications for Horseshoe Conformation

The extracellular region of Nfasc and other L1 family molecules contains the characteristic Ig like and FNIII domains, but it also includes peptide sequences that are not included in either of these types of domains. One such peptide sequence is a linker peptide located between Ig2 and 3 (Nfasc exon 11, Fig. 3.4). This sequence is thought to

be provide flexibility, allowing Ig1 and 2 to pivot independently of the rest of L1CAM (Bateman et al., 1996) and allowing the Ig domains to adopt the horseshoe conformation (De Angelis et al., 2002). Nfasc 155 includes the Ig2–Ig3 linker and its crystallized structure revealed a horseshoe conformation. Furthermore, Nfasc 155 interacts with contactin (Gollan et al., 2003), a member of the Ig superfamily, underscoring the possibility that the Ig2-Ig3 linker peptide is critical for homophilic interactions. However, Nfasc 186 lacks the Ig2–Ig3 linker and reported binding partners for Nfasc 186 include NrCAM (Lustig et al., 2001; Volkmer et al., 1996), a homophilic binding partner suggesting that the Ig2-Ig3 linker peptide is not necessary for such associations. Interestingly, in the CNS, NrCAM-Nfasc binding occurs in *cis*, and Nfasc 186 binding partners in *trans* have not yet included other L1 CAMs, but rather ECM molecules (Hedstrom et al., 2007; Labasque et al., 2011; Volkmer et al., 1998). Perhaps lack of the Ig2-Ig3 linker sequence in Nfasc 186 and, consequently, a lack of horseshoe conformation provides rationale for this observation. If so, a similar interaction with ECM molecules is possible for microglial Nfasc, which also lacks the Ig2-Ig3 linker sequence.

Microglial Nfasc also lacks a hinge domain, located between the Ig like and FNIII domains, which is included in other Nfasc isoforms. When this domain was excluded using site-directed mutagenesis, quantitation of Nfasc-Fc protein aggregation demonstrated less homophilic binding (Basak et al., 2007). These data suggest that microglial Nfasc, while capable of interacting homophilically, may instead participate in heterophilic interactions.

Microglial Nfasc Contains the RGD Integrin Binding Motif: Implications for Heterophilic Interactions

Consistent with microglial Nfasc participating in heterophilic interactions, microglial Nfasc contains a specific Arg-Gly-Asp (RGD) integrin binding motif in its ectodomain. This sequence is located in the third FNIII repeat of microglial Nfasc and Nfasc 155 and in the Ig6 domain of L1CAM. The RGD amino acid sequence mediates binding with RGD-specific integrins including $\beta 1$ integrins, VLA-5, and $\alpha 5\beta 3$, which are important for promoting cell adhesion and directional motility (Felding-Habermann et al., 1997; Hortsch et al., 2014; Koticha et al., 2005; Montgomery et al., 1996; Ruppert et al., 1995; Thelen et al., 2002; Yip et al., 1998). Microglia express integrins that, upon binding, regulate the inflammatory response and cell motility such as CD11b, VLA-4, and VLA-5. These are up-regulated in microglia during pro-inflammatory conditions and play a role in microglial NOX2-mediated activation, migration, and recruitment (Kim et al., 2014; Milner and Campbell, 2003; Zhang et al., 2018). Nfasc molecules may interact with integrins to enhance clustering and initiate downstream signaling cascades. This has been shown for L1CAM, which interacts with $\beta 1$ integrins, resulting in increased clustering and initiation of signal transduction through activation of PI3 kinase and ERK, thereby promoting cell adhesion to ECM proteins (Maness and Schachner, 2007; Silletti et al., 2004; Thelen et al., 2002).

Integrin binding also initiates signaling cascades with growth factor signaling networks to promote motility. For example, expression of a chick Nfasc isoform that lacks the mucin/5th FNIII domain induced association with the fibroblast growth factor receptor 1 (FGFR1) in neurons resulting in the regulation of process extension, whereas the Nfasc

isoform maintaining the mucin/5th FNIII domain did not interact with FGFR1 (Kirschbaum et al., 2009). Furthermore, direct binding of fibroblast growth factor receptor 1 to integrin $\alpha 5\beta 3$ was necessary for proper FGFR1 signaling (Mori et al., 2008). Likewise, simultaneous stimulation of integrin by L1 and platelet derived growth factor receptor in HEK293 cells caused sustained activation of the MAP kinase pathway, which activated transcription of cell motility genes. Application of RGD-containing peptides blocked interaction with the ECM and migration demonstrating this interaction is dependent on the RGD sequence (Thelen et al., 2002). These findings suggest a common mechanism among IgCAMs to modulate integrin activated pathways. The integrin binding RGD domain in the 3rd FNIII repeat is maintained in oligodendrocyte Nfasc 155 and microglial Nfasc, but excluded from neuronal Nfasc 186 and 140, thus integrin-mediated signaling may be a unique function specific to glial Nfasc.

Microglial Nfasc Contains Conserved Ankyrin-Binding Domains: Implications for Intracellular Interactions

Clustering of L1-type CAMs occurs not only through extracellular interactions, but also through the binding of intracellular scaffolding proteins. The cytoplasmic segment consists of 110 amino acid residues and contains characteristic tyrosine-containing amino acid motifs. Two of these motifs, LVDY and FIGQY, exhibit the highest degree of sequence conservation throughout the L1 family and comprise the ankyrin-binding site (Garver et al., 1997; Hortsch, 1996, 2000; Tuvia et al., 1997; Zhang et al., 1998). Specifically, the phosphorylation/dephosphorylation of the FIGQY motif regulates the reversible binding of L1-type proteins to ankyrin (Garver et al., 1997), an adaptor protein

that links L1 molecules, ion channels, and calcium-release channels to the spectrin-based membrane skeleton (Bennett and Baines, 2001; Davis and Bennett, 1994; Garver et al., 1997; Jenkins and Bennett, 2002). The presence of the highly conserved LVDY and FIGQY (Supplementary Fig. 3.1) and high conservation of the L1-ankyrin interaction throughout the L1 family suggests that recruitment of membrane skeletal elements is an important aspect of L1 function and, thus, microglial Nfasc. Interestingly, increased *ANK1*, the ankyrinR coding gene, has been associated with disease pathogenesis in Alzheimer's disease (De Jager et al., 2014; Lunnon et al., 2014) and a recent study utilized laser capture microdissection to reveal that microglia in the hippocampus of patients with Alzheimer's disease increased expression of ankyrin (*ANK1*) 4-fold, but not astrocytes or neurons (Mastroeni et al., 2017). They found a similar increase in *ANK1* in microglia from tissue of patients with Parkinson's disease suggesting that microglial alterations of ankyrin may not be disease specific, but rather a response to a common pathway in neurodegenerative conditions (e.g. inflammation or oxidative stress) (Mastroeni et al., 2017). It will be interesting to determine if the highly conserved Nfasc/ankyrin interaction is present in microglia and if this interaction could play an important role in the microglial response during inflammatory conditions. Indeed, western blot and IHC analyses presented here revealed a significant upregulation of microglial Nfasc in inflammatory conditions (Fig. 3.2).

Nfasc in Microglia: Multiple isoforms or Post-Translational Processing?

Western blot analysis revealed three immunoreactive Nfasc bands (Fig. 3.2). One explanation for this finding is contamination from other cellular sources; however,

microglia for western blot analysis were isolated via FACS (Supp. Fig. 3.2) and qPCR analysis of cell specific markers in FACS-isolated samples revealed that microglial isolates were enriched for microglial marker colony stimulating factor 1 receptor (CSF1r), but not the oligodendrocyte marker cyclic nucleotide phosphodiesterase (CNP) or the neuronal marker RNA binding fox-1 homolog 3 (RbFox3) (Supp. Fig. 3.3). Thus, another explanation is that microglia express multiple Nfasc isoforms, consistent with reports for other cell types (Charles et al., 2002; Zhang et al., 2015).

An alternative explanation for multiple Nfasc bands is posttranslational modifications. Posttranslational modification of Nfasc CAMs include palmitoylation (Ren and Bennett, 1998), o-mannosylation (Pacharra et al., 2012), phosphorylation (Tuvia et al., 1997), and glycosylation (Davis et al., 1993; Labasque et al., 2014; Maier et al., 2005; Volkmer et al., 1992) . In particular, Nfasc isoforms and other Ig type CAMs can be extensively N-linked glycosylated, which can account for 25% of total protein mass (Haspel and Grumet, 2003; Salton et al., 1983; Stallcup and Beasley, 1985); thus, N-linked glycosylations could also explain the size difference among the three bands in microglia.

Microglial Nfasc protein: highly stable or increased microglial proliferation?

Pillai and colleagues (2009) demonstrated that Nfasc 155 levels persist at 40 days after tamoxifen induction and near-complete absence of Nfasc 155 is not seen until 90 days after injection (Pillai et al., 2009). These findings indicate that Nfasc 155 is quite stable once expressed. In this study, we examined microglial Nfasc protein levels at 45

days post-induction and found that *Nfasc* bands were not diminished in *Nfasc* null mice (Fig. 3.8). However, DNA and RNA analysis confirmed that gene recombination and reduction of *Nfasc* transcript took place suggesting that lack of protein reduction may be due to protein stability.

Persistent *Nfasc* protein levels could also be due to new protein production. Cre-mediated gene recombination is not 100% efficient and complete loss of *Nfasc* transcript is not detected after 4-HT induction (Fig. 3.3 and 3.8). Therefore, proliferation of microglia that have not undergone gene recombination could result in increased production of *Nfasc* in 4HT-injected mice, and thus, overall protein levels could maintain. Interestingly, quantitation of *Nfasc* transcript levels in this study revealed that at 14 days post-4-HT induction there was an approximate 70% reduction of *Nfasc* mRNA; however, at 45 days post-4-HT there was a 45% reduction detected (Fig. 3.8D). These findings suggest that there may be a preferential proliferation of cells in which *Nfasc* is not disrupted; though, further studies investigating cell proliferation are needed to clarify this.

Sequence of Microglial *Nfasc* Aligns with Previously Unidentified Variant 4

Complete sequence alignment with published *Nfasc* sequences from NCBI yielded a surprising find: while the microglial *Nfasc* isoform was unique compared to *Nfasc* 186 and *Nfasc* 155, it strongly aligned with the sequence for variant 4 (Supp. Fig. 3.1). Variant 4 is a *Nfasc* sequence for a *Nfasc* isoform with an unidentified cellular origin. A study performing large-scale sequencing analysis on whole brain homogenate identified and published sequences for four *Nfasc* variants (Okazaki et al., 2003; Strausberg et al.,

2002). Two of these sequences correspond to characterized isoforms: variant 1 – Nfasc 186, variant 2 – Nfasc 155; however, the cellular source for variants 3 and 4 had not been determined. Here, I found that the sequence of microglial Nfasc aligns with variant 4 (Supp. Fig. 3.1)(Fig. 3.5A), which has a domain composition excluding alternatively spliced hinge domains in the N-terminal and central region, the mucin domain and 5th FNIII repeat while including the 3rd FNIII repeat (Fig. 3.6).

Conclusion

Here, I have demonstrated that microglia express a novel Nfasc isoform and this isoform is enriched in microglial processes and at the interface of microglia-AIS contact. Furthermore, expression of microglial Nfasc is upregulated in neuroinflammatory conditions paralleling disease-dependent increase in microglia-AIS contact. Therefore, these findings identify a candidate that may regulate the contact between microglia and the AIS, though previous findings of functions and interactions of other IgCAM family members suggest that this protein may have numerous interacting partners consistent with the diverse roles microglia play in the CNS.

Figure 3.1

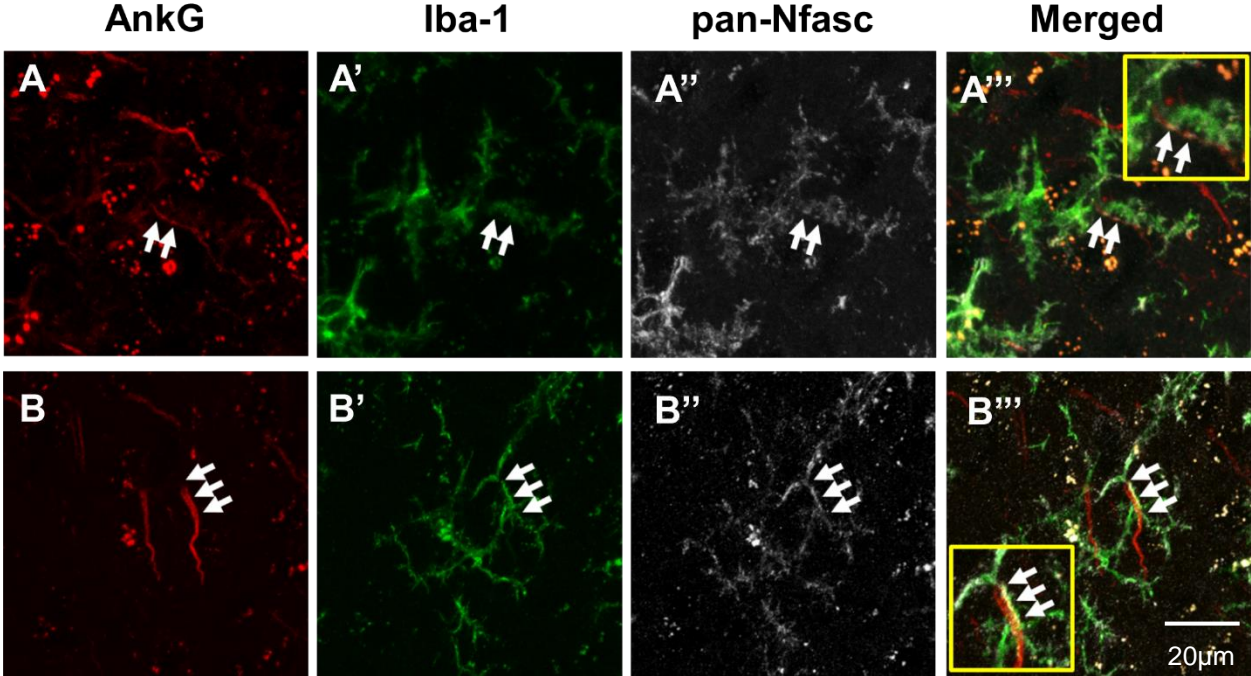


Figure 3.1. Microglial Nfasc Clusters at the Microglia-AIS Interface. Microglia, visualized by Iba-1 immunolabeling (A-B', green), from cortical brain sections of EAE-induced mice have robust Nfasc labeling (A-B'', grey, white arrows) that clusters in microglial processes and at the microglia/AIS interface (A-B''', white arrows).

Figure 3.2

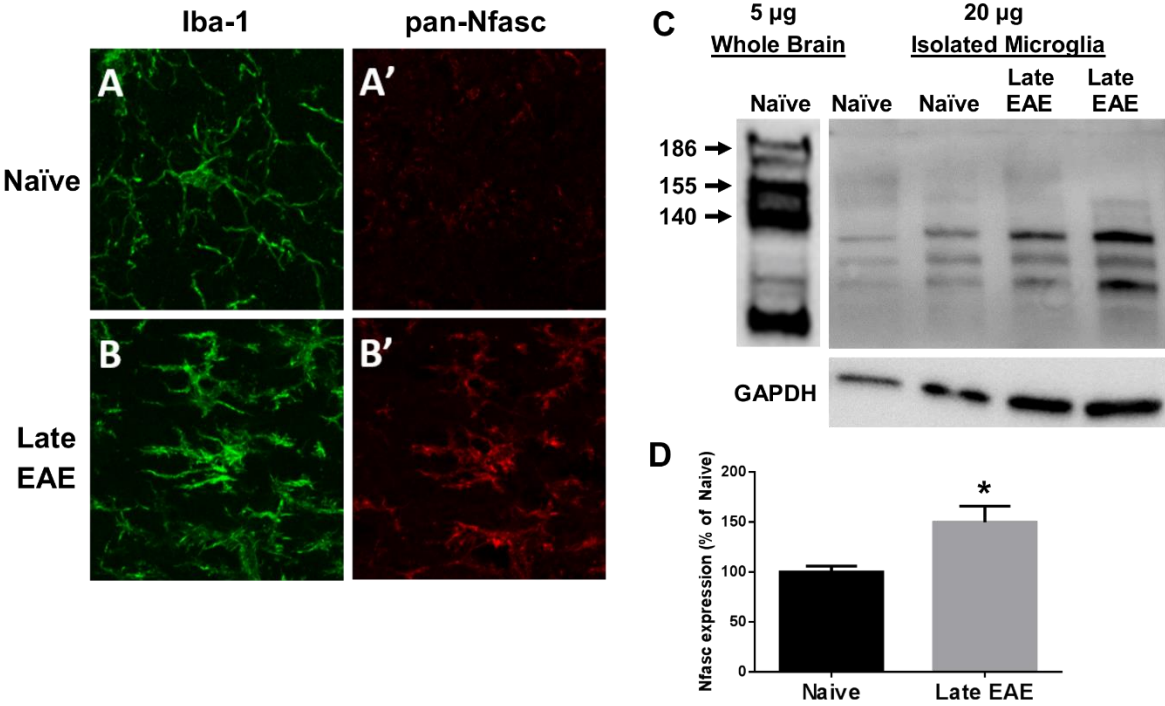


Figure 3.2. Microglial Nfasc is Up-regulated in EAE. A-B, Cortical brain sections from naïve mice reveal microglia (A-B, Iba-1, green) lack detectable levels of Nfasc (A', red); however, microglia in EAE-induced mice have robust Nfasc labeling (B'', red). C-D, Western blot analysis using a FIGQY pan-Nfasc antibody revealed 3 Nfasc isoforms in whole brain homogenate (5ug) (C): Nfasc186 (neuron specific), Nfasc155 (myelin specific), and Nfasc140 (immature neuron specific). Homogenates (20µg) of isolated microglia from cortices of Naïve and EAE mice revealed Nfasc bands of unique molecular weights that displayed increased density corresponding with increased disease severity (C). D, Densitometric analysis of prominent Nfasc bands present in isolated microglia (C, 3 bands, combined) as a ratio of GAPDH expression revealed a significant increase in Nfasc expression in EAE-induced mice. An asterisk indicates significant difference (n=3, $p < 0.05$) from naïve.

Figure 3.3

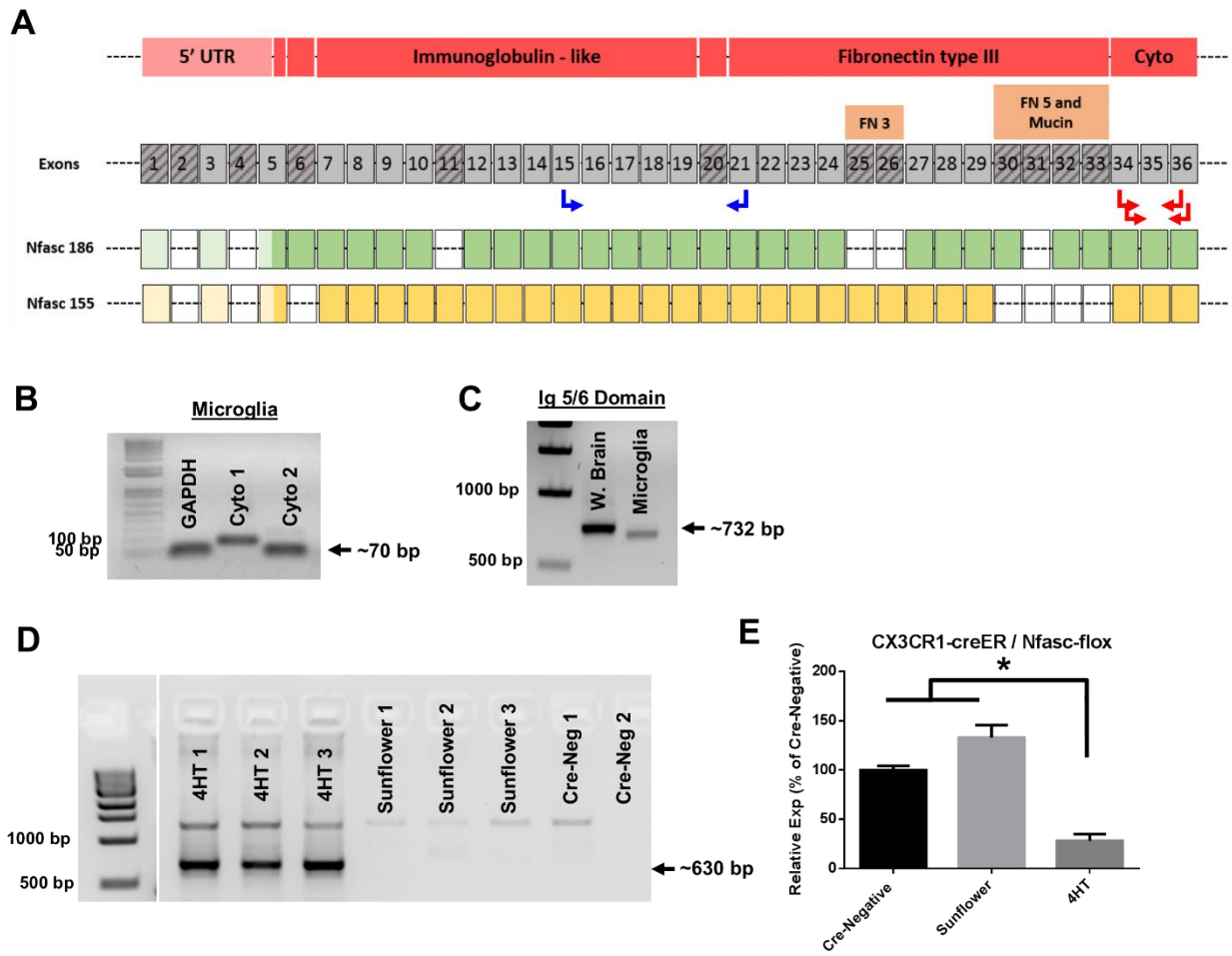


Figure 3.3. Microglia Express Nfasc mRNA, Contain Nfasc binding domains Ig 5 and 6, and Generation of Microglia-specific Nfasc null mice Confirms Presence of Nfasc Gene Product. A, schematic diagram depicting *Nfasc* exons (A, grey) and the coding exons for Ig-like, FN type III, and cytoplasmic protein domains (A, red). *Nfasc* has numerous alternatively spliced exons represented by grey squares with diagonal lines (A). Two well-characterized *Nfasc* isoforms, *Nfasc* 186 (A, green) and *Nfasc* 155 (A, yellow), are shown. White squares indicate exons that are alternatively spliced in that isoform. Primer pairs were designed against two domains conserved between *Nfasc* isoforms: Ig 5 and 6 (A, blue arrows) and cytoplasmic domain (A, red arrows, two sets). B, PCR amplification of cDNA from FACS-isolated microglia of WT mice revealed that isolated microglia contain both the conserved *Nfasc* cytoplasmic domain (B) as well as the conserved *Nfasc* binding domain Ig 5 and 6 (C). D, *CX3CR1^{creER+/-}/Nfasc^{fl/fl}* mice confirmed that *Nfasc* mRNA detected in microglial isolates were *Nfasc* gene products. PCR amplification of genomic DNA isolated from microglia of 4HT or sunflower injected *CX3CR1^{creER+/-}/Nfasc^{fl/fl}* mice and *CX3CR1^{creER-/-}/Nfasc^{fl/fl}* mice using specific primers recognizing the excision product of the *Nfasc* allele. The presence of the 630bp band confirmed that cre-mediated recombination of the *Nfasc* allele took place in *CX3CR1*-positive cells (microglia) in 4HT-injected mice, but not in sunflower (vehicle) controls or cre-negative (*CX3CR1^{creER-/-}/Nfasc^{fl/fl}*) mice. E, RT-qPCR of cDNA isolated from whole brain or microglia of 4HT or sunflower injected *CX3CR1^{creER+/-}/Nfasc^{fl/fl}* mice demonstrates reduced *Nfasc* mRNA levels in 4HT-injected microglia versus sunflower controls; however, *Nfasc* levels in other cell types (whole brain homogenate) are not diminished.

Figure 3.4

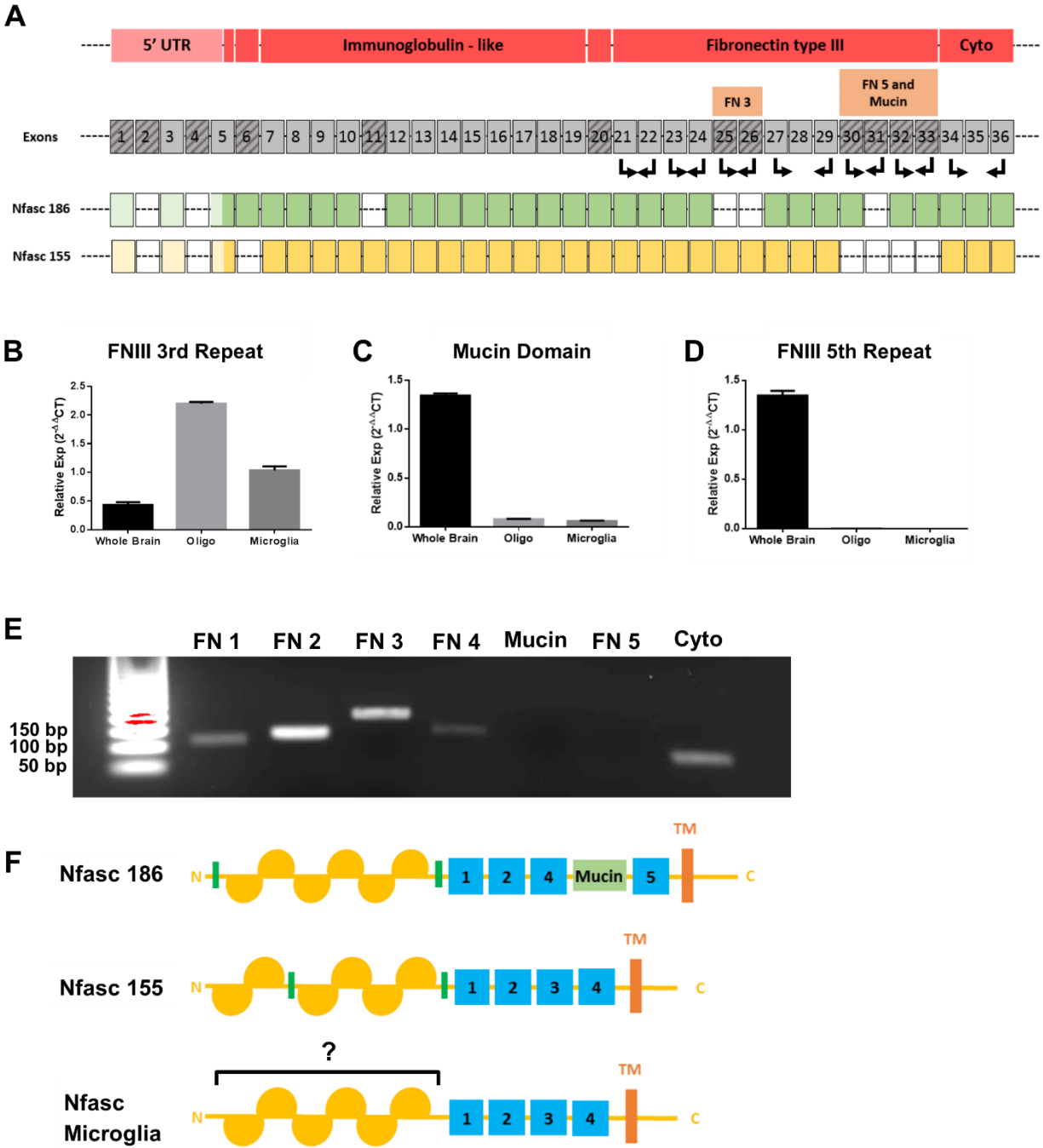


Figure 3.4. Microglial Nfasc Maintains Conserved FNIII and Cytoplasmic Domains and Excludes the Alternatively Spliced Mucin and 5th FNIII Repeat. A, schematic diagram depicting *Nfasc* exons (A, grey) and the coding exons for Ig-like, FN type III, and cytoplasmic protein domains (A, red). *Nfasc* has numerous alternatively spliced exons represented by grey squares with diagonal lines (A). Two well-characterized *Nfasc* isoforms, *Nfasc* 186 (A, green) and *Nfasc* 155 (A, yellow), are shown. White squares indicate exons which are alternatively spliced in that isoform. *Nfasc* 186 (A, green), a neuronal-specific isoform, begins coding in the 5th exon, excludes exons 11 and 25-26 (FNIII 3rd repeat), and maintains exons 30, 32, and 33 (FNIII 5th repeat and mucin domains). Conversely, *Nfasc* 155, the myelin-specific isoform, maintains exons 11 and the FNIII 3rd repeat, while excluding the FNIII 5th repeat and mucin domains. Primer pairs were designed against the conserved cytoplasmic domain and several fibronectin type III (FNIII) domains which are either conserved among isoforms or alternatively spliced (A, black arrows). B-D, RT-qPCR analysis of whole brain homogenate, isolated oligodendrocytes, and FACS-isolated microglia revealed that the *Nfasc* cytoplasmic domain was amplified in all samples (B); however, the mucin (C) and 5th FNIII repeat (D) was not detected in oligodendrocytes or microglia demonstrating that microglial *Nfasc* has similar domain composition in the FNIII region to *Nfasc* 155 present in oligodendrocytes. E, RT-qPCR amplified *Nfasc* products from microglia were analyzed by agarose gel electrophoresis confirming the presence or absence of various FNIII domains. F, schematic depicting protein domain composition of *Nfasc* 186, *Nfasc* 155, and microglial *Nfasc* demonstrating that microglial *Nfasc* has similar composition to *Nfasc* 155 in the FNIII region.

Figure 3.5

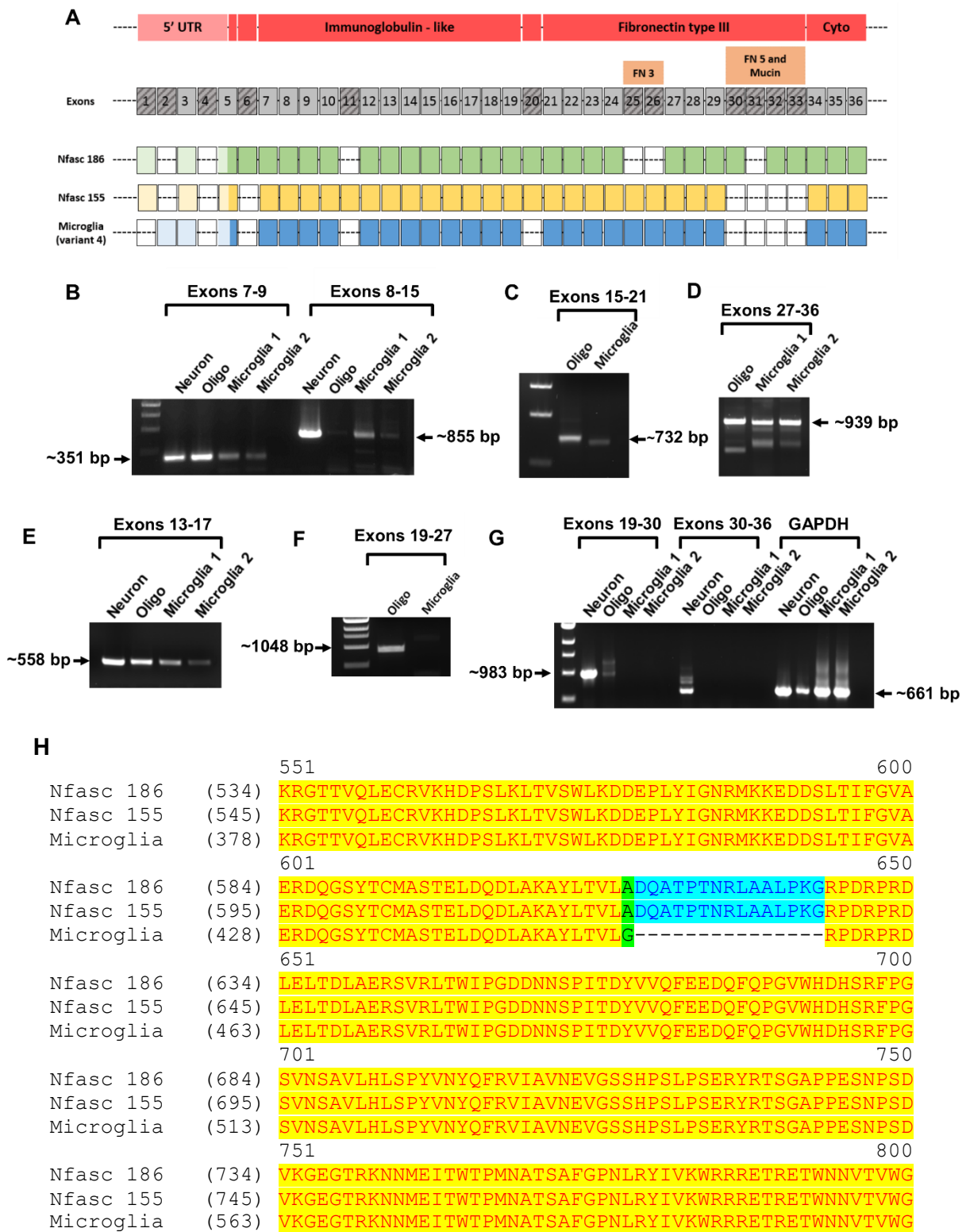


Figure 3.5. PCR Amplification and Sequencing Reveals Microglial Nfasc Transcript is Unique from Nfasc 186 and Nfasc 155. A, schematic diagram depicting *Nfasc* exons (A, grey) and the coding exons for Ig-like, FN type III, and cytoplasmic protein domains (A, red). *Nfasc* has numerous alternatively spliced exons represented by grey squares with diagonal lines (A). Two well-characterized *Nfasc* isoforms, *Nfasc* 186 (A, green) and *Nfasc* 155 (A, yellow), and newly identified microglial *Nfasc* (A, blue) are shown. White squares indicate exons which are alternatively spliced in that isoform. Microglial *Nfasc* (A, blue) has some differences in the 5' UTR but maintains the same coding exon as *Nfasc* 186 and 155. Microglial *Nfasc* excludes exon 20 demonstrating its uniqueness compared to other described isoforms. B-G, PCR amplification of cDNA from FACS-isolated microglia, neurons, oligodendrocytes, or whole brain homogenate. Primer pairs were designed to span ~300-1000bp regions of the coding region of the *Nfasc* gene with at least 100bp of overlap. Amplified products were analyzed by agarose gel electrophoresis and gel-purified products were commercially sequenced. H, Sequence alignment revealed microglial *Nfasc* is highly similar to known *Nfasc* isoforms (G, yellow regions): however, microglial *Nfasc* has a unique region compared to neuronal *Nfasc* 186 and myelin *Nfasc* 155 (H, blue regions) as it excludes exon 20, a small domain present at the hinge region between Ig-like and FNIII domains. Full sequence alignment is present in Supplementary Figure 3.1.

Figure 3.6

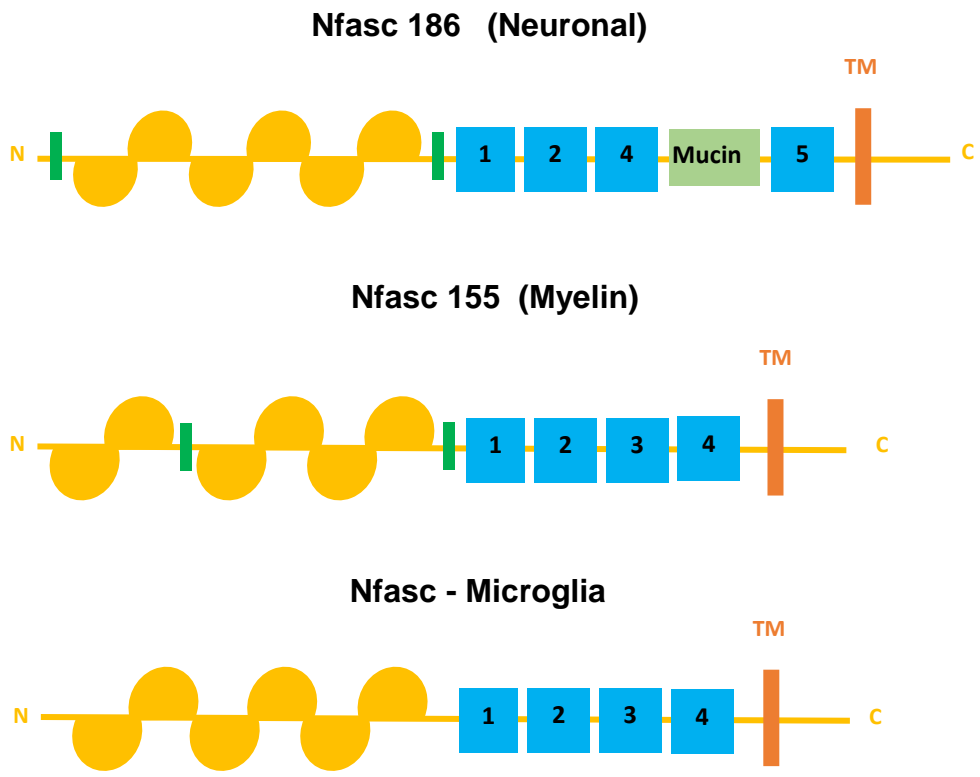


Figure 3.6. Proposed Domain Composition of Microglial Nfasc. Proposed domain composition based on the sequenced transcript of microglial Nfasc demonstrates the exclusion of a small domains present at the N-terminus and a hinge domain between the Ig-like and FNIII domains.

Figure 3.7

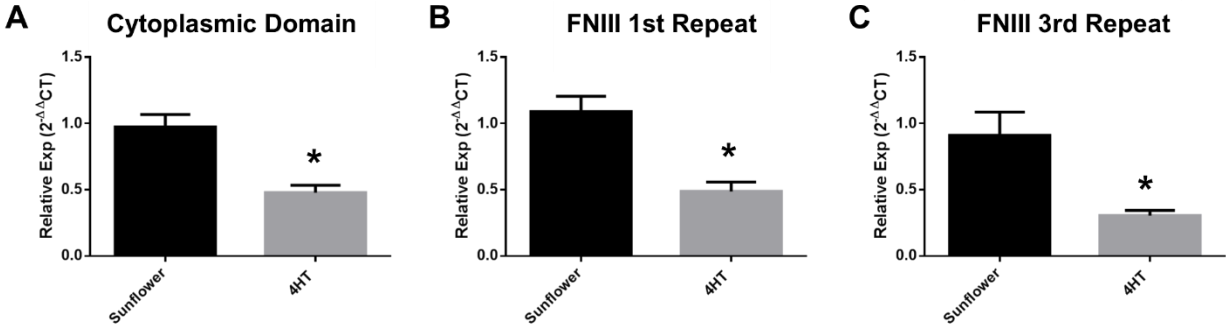


Figure 3.7. RT-qPCR Analysis using microglial *Nfasc null* mice confirms that Microglial *Nfasc* Transcript has the Conserved Cytoplasmic and 1st FNIII Repeat and the Alternatively Spliced 3rd FNIII Repeat. A-C, relative expression levels of *Nfasc* mRNA in FACS-isolated microglia from 4HT or sunflower injected *CX3CR1^{creER/+}/*Nfasc^{fl/fl}** mice demonstrates reduced levels of *Nfasc* cytoplasmic (A), 1st FNIII (B), and the 3rd FNIII domains in 4HT-injected microglia. These data confirm the presence of these domains in microglial *Nfasc*. An asterisk indicates significant difference (n=3, $p < 0.05$) from sunflower control.

Figure 3.8

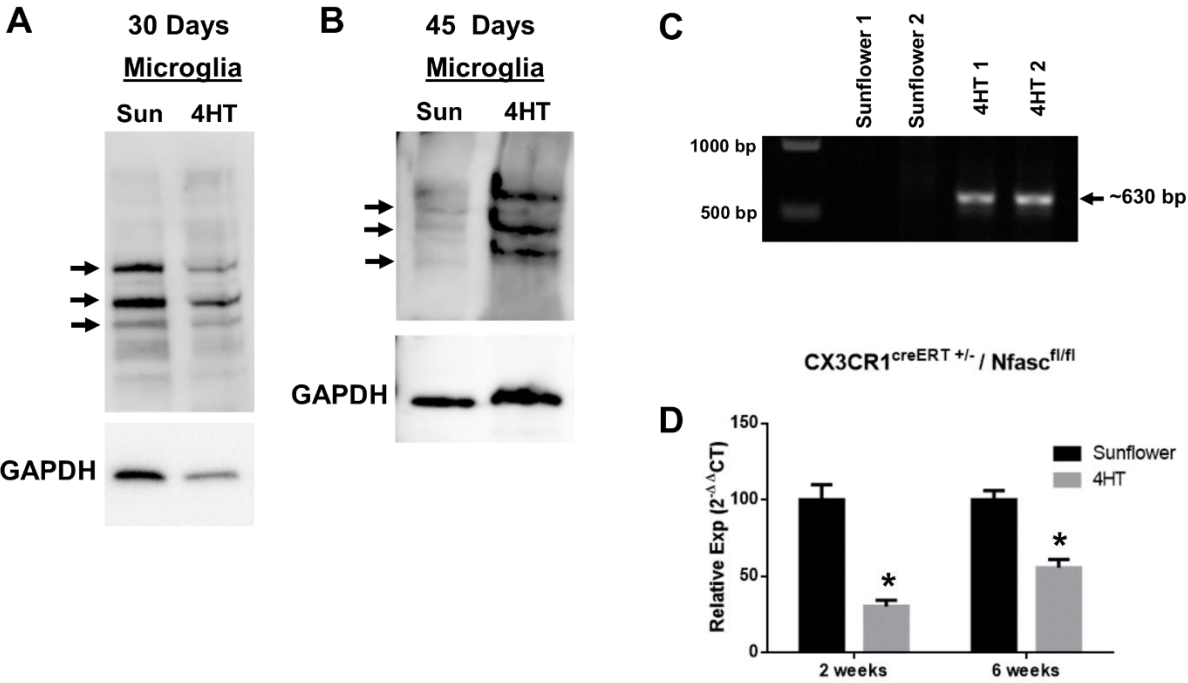


Figure 3.8. Protein levels are not reduced 45 days post-4-HT induction in *CX3CR1^{creER+/-}/Nfasc^{fl/fl}* mice. A-B, Western blot analysis using a FIGQY pan-Nfasc antibody revealed Nfasc immunoreactive bands are not diminished in isolated microglia from 4-HT injected *CX3CR1^{creER+/-}/Nfasc^{fl/fl}* mice compared to vehicle sunflower injected *CX3CR1^{creER+/-}/Nfasc^{fl/fl}* mice at either 30 (A) or 45 (B) days post-4-HT induction. C, PCR amplification of genomic DNA isolated from microglia of 4-HT or sunflower injected *CX3CR1^{creER+/-}/Nfasc^{fl/fl}* mice using primers recognizing the excision product of the *Nfasc* allele. The presence of the 630bp band confirmed that cre-mediated recombination of the *Nfasc* allele took place in CX3CR1-positive cells (microglia) in 4-HT-injected mice, but not in sunflower (vehicle) control mice at 45 days post-4-HT induction. D, RT-qPCR of cDNA isolated from microglia of 4-HT or sunflower injected *CX3CR1^{creER+/-}/Nfasc^{fl/fl}* mice demonstrates reduced Nfasc mRNA levels in 4-HT-injected microglia versus sunflower controls. An asterisk indicates significant difference (n=3-5, $p < 0.05$) from sunflower control.

Table 3.1. Oligonucleotide Primer Pairs Used for RT-qPCR and end-point PCR

Gene	Forward Primer (5' → 3')	Reverse Primer (5' → 3')	Expected Size (bp)
Nfasc cyto 2	GTGATGAGGACAACAAGCCC	CTCTCCTGCTGCVTTGATGGT	70
Nfasc cyto 1	CAAGTACCCAGTGCGGGAAA	CTCTCCTGCTGCTTGATGGT	150
Nfasc 1 st FNIII	AGTGTGAGGCTGACCTGGAT	TGGGAACCTGGAGTGGTCA	120
Nfasc 2 nd FNIII (Basak et al., 2007)	ATTGTCAAGTGGCGACGGA	CCAAAGTCATTTTCAGCCTGG	134
Nfasc 3 rd FNIII (Basak et al., 2007)	TCAGTGGAAACCGAGTCTACTC	ACCACCACCATCTCCAGCTTG	201
Nfasc 4 th FNIII (Basak et al., 2007)	TTTCAGAGTCCGACAGCCCAA	TTCCACCATCTGCTTTCCAG	139
Nfasc 5 th FNIII (Basak et al., 2007)	TGGAAGCACAATTTTCAGGCC	AATACACCCGCAACGTGTACG	151
Nfasc Mucin (Basak et al., 2007)	TTCTCCCTCAGTGCCAGGAC	TGGGATGATGGGAACTGTTGT	201
Cyclophilin A	CTAGAGGGCATGGATGTGGT	TGACATCCTTCAGTGGCTTG	78
PGK1	ATGCAAAGACTGGCCAAGCTAC	AGCCACAGCCTCAGCATATTTTC	104
Nfasc exons 7-9	AGAATGAGCTGACCCAACCC	CGACGGGGTCTAGGTTTTCC	351
Nfasc exons 8-15	TGCAGGTGTCCAAATCTCCC	CCAGCAGGTAGCCATGTTCA	855
Nfasc exons 13-17	GCACACGATCTCGGTGAGAG	TTTTCGGCTTTGCCAGGAT	558
Nfasc exons 15-21 (Ig 5 and 6)	CAGCAGGGCAGTGTACCAAT	CTCACACTCCTCTCAGCCAG	732
Nfasc exons 19-30	GCAAAGGCCTACCTCACTGT	GGAGGAGCTGCAGTTGGAGT	983
Nfasc exons 27-36	GCTACTCCAACCTGCAGCTTACAC	TTCATTTCTTGGGGAGAGCC	939
Nfasc exons 30-36	AACTGCAGCTCCTCCCAC	TCATTGCCCTCCGTTTCCTC	800
Nfasc exons 19-27	GCAAAGGCCTACCTCACTGT	GCAAGGGCAGTAGCATCAGT	1048

GAPDH (qRT-PCR)	AACTTTGGCATTGTGGAAGG	ATCCACAGTCTTCTGGGTGG	69
GAPDH (end-point PCR)	TGATGGGTGTGAACCACGAG	GCCTCTCTTGCTCAGTGTC	661
RbFox3 (NeuN)	GTTGCCTACCGGGGTGCACAC	TGCTCCAGTGCCGCTCCATAAG	110
CNP (Bennett et al., 2016)	TTCTGTGACTACGGGAAGGC	TCTCTTACCACCTCCTGCT	63
CSF1r (Bennett et al., 2016)	TGAGCAAGACCTGGACAAGGA	CCGCTGGTCAACAGCACGTTT	153

Supplementary Figure 3.1

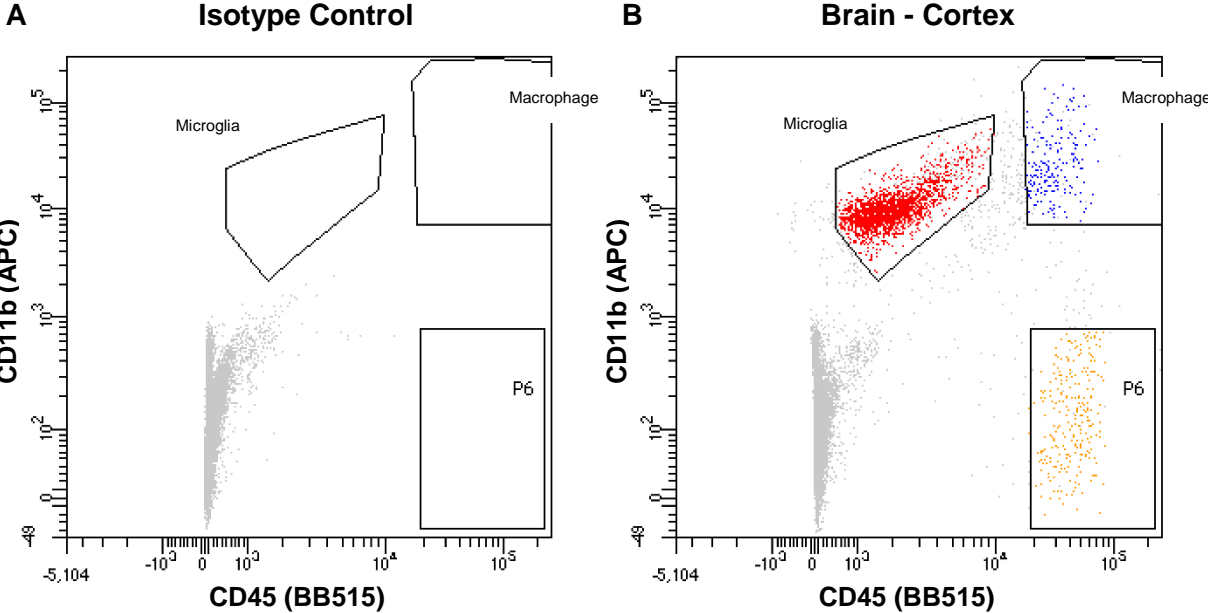
		1	50
Nfasc 186	(1)	MARQQAPPVWHIALILFLLSLGGAIEIPMDPSIQNE	LTQPPTITKQSVKD
Nfasc 155	(1)	MARQQAPPVWHIALILFLLSLGGAIEIPMD	-----LTQPPTITKQSVKD
Nfasc Variant 3	(1)	MARQQAPPVWHIALILFLLSLGGAIEIPMD	-----LTQPPTITKQSVKD
Nfasc Variant 4	(1)	MARQQAPPVWHIALILFLLSLGGAIEIPMD	-----LTQPPTITKQSVKD
Microglia Nfasc	(1)	-----	LTQPPTITKQSVKD
		51	100
Nfasc 186	(51)	HIVDPRDNILIECEAKGNPAPSFHWTRNSRFFNIAKDPRVSMRRRSGLTV	
Nfasc 155	(45)	HIVDPRDNILIECEAKGNPAPSFHWTRNSRFFNIAKDPRVSMRRRSGLTV	
Nfasc Variant 3	(45)	HIVDPRDNILIECEAKGNPAPSFHWTRNSRFFNIAKDPRVSMRRRSGLTV	
Nfasc Variant 4	(45)	HIVDPRDNILIECEAKGNPAPSFHWTRNSRFFNIAKDPRVSMRRRSGLTV	
Microglia Nfasc	(15)	HIVDPRDNILIECEAKGNPAPSFHWTRNSRFFNIAKDPRVSMRRRSGLTV	
		101	150
Nfasc 186	(101)	IDFRSGGRPEEYEGEYQCFARNKFGTALS NRIRLQVSKSPLWPKENLDPV	
Nfasc 155	(95)	IDFRSGGRPEEYEGEYQCFARNKFGTALS NRIRLQVSKSPLWPKENLDPV	
Nfasc Variant 3	(95)	IDFRSGGRPEEYEGEYQCFARNKFGTALS NRIRLQVSKSPLWPKENLDPV	
Nfasc Variant 4	(95)	IDFRSGGRPEEYEGEYQCFARNKFGTALS NRIRLQVSKSPLWPKENLDPV	
Microglia Nfasc	(65)	IDFRSGGRPEEYEGEYQCFARNKFGTALS NRIRLQVSKSPLWPKENLDPV	
		151	200
Nfasc 186	(151)	VVQEGAPLTLQCNPPLPSPVIFWMSSMEPITQDKRVSQGHNGDLYFS	
Nfasc 155	(145)	VVQEGAPLTLQCNPPLPSPVIFWMSSMEPITQDKRVSQGHNGDLYFS	
Nfasc Variant 3	(145)	VVQEGAPLTLQCNPPLPSPVIFWMSSMEPITQDKRVSQGHNGDLYFS	
Nfasc Variant 4	(145)	VVQEGAPLTLQCNPPLPSPVIFWMSSMEPITQDKRVSQGHNGDLYFS	
Microglia Nfasc	(115)	VVQEGAPLTLQCNPPLPSPVIFWMSSMEPITQDKRVSQGHNGDLYFS	
		201	250
Nfasc 186	(201)	NVMLQDMQTDYSCNARFHFTHTIQQKNPFTLKVLT	-----
Nfasc 155	(195)	NVMLQDMQTDYSCNARFHFTHTIQQKNPFTLKVLT	NNPYNDSSLRNHPDI
Nfasc Variant 3	(195)	NVMLQDMQTDYSCNARFHFTHTIQQKNPFTLKVLT	NNPYNDSSLRNHPDI
Nfasc Variant 4	(195)	NVMLQDMQTDYSCNARFHFTHTIQQKNPFTLKVLT	-----
Microglia Nfasc	(165)	NVMLQDMQTDYSCNARFHFTHTIQQKNPFTLKVLT	-----
		251	300
Nfasc 186	(237)	---RGVAERTPSFMYPQGTSSSQMVLRGMDLLECIASGVPTPDI AWYKK	
Nfasc 155	(245)	YSARGVAERTPSFMYPQGTSSSQMVLRGMDLLECIASGVPTPDI AWYKK	
Nfasc Variant 3	(245)	YSARGVAERTPSFMYPQGTSSSQMVLRGMDLLECIASGVPTPDI AWYKK	
Nfasc Variant 4	(231)	---RGVAERTPSFMYPQGTSSSQMVLRGMDLLECIASGVPTPDI AWYKK	
Microglia Nfasc	(201)	---RGVAERTPSFMYPQGTSSSQMVLRGMDLLECIASGVPTPDI AWYKK	
		301	350
Nfasc 186	(284)	GGDLPSNKAKFENFNKALRITNVSEEDSGEYFCLASNKMG SIRHTISVRV	
Nfasc 155	(295)	GGDLPSNKAKFENFNKALRITNVSEEDSGEYFCLASNKMG SIRHTISVRV	
Nfasc Variant 3	(295)	GGDLPSNKAKFENFNKALRITNVSEEDSGEYFCLASNKMG SIRHTISVRV	
Nfasc Variant 4	(278)	GGDLPSNKAKFENFNKALRITNVSEEDSGEYFCLASNKMG SIRHTISVRV	
Microglia Nfasc	(248)	GGDLPSNKAKFENFNKALRITNVSEEDSGEYFCLASNKMG SIRHTISVRV	
		351	400
Nfasc 186	(334)	KAAPYWLDEPKNLI LAPGEDGRLVCRANGNPKPTVQWMVNGEPLQSAPPN	
Nfasc 155	(345)	KAAPYWLDEPKNLI LAPGEDGRLVCRANGNPKPTVQWMVNGEPLQSAPPN	
Nfasc Variant 3	(345)	KAAPYWLDEPKNLI LAPGEDGRLVCRANGNPKPTVQWMVNGEPLQSAPPN	
Nfasc Variant 4	(328)	KAAPYWLDEPKNLI LAPGEDGRLVCRANGNPKPTVQWMVNGEPLQSAPPN	
Microglia Nfasc	(298)	KAAPYWLDEPKNLI LAPGEDGRLVCRANGNPKPTVQWMVNGEPLQSAPPN	
		401	450
Nfasc 186	(384)	PNREVAGDTIIFRDTQISSRAVYQCNTSNEHG YLLANAFVSVLDVPPRML	
Nfasc 155	(395)	PNREVAGDTIIFRDTQISSRAVYQCNTSNEHG YLLANAFVSVLDVPPRML	
Nfasc Variant 3	(395)	PNREVAGDTIIFRDTQISSRAVYQCNTSNEHG YLLANAFVSVLDVPPRML	
Nfasc Variant 4	(378)	PNREVAGDTIIFRDTQISSRAVYQCNTSNEHG YLLANAFVSVLDVPPRML	
Microglia Nfasc	(348)	PNREVAGDTIIFRDTQISSRAVYQCNTSNEHG YLLANAFVSVLDVPPRML	

		451		500
Nfasc 186	(434)	SARNQLIRVILYNRTRLDCPFFGSP IPTLRWFKNQGSNLDGGNYHVVYEN		
Nfasc 155	(445)	SARNQLIRVILYNRTRLDCPFFGSP IPTLRWFKNQGSNLDGGNYHVVYEN		
Nfasc Variant 3	(445)	SARNQLIRVILYNRTRLDCPFFGSP IPTLRWFKNQGSNLDGGNYHVVYEN		
Nfasc Variant 4	(428)	SARNQLIRVILYNRTRLDCPFFGSP IPTLRWFKNQGSNLDGGNYHVVYEN		
Microglia Nfasc	(398)	SARNQLIRVILYNRTRLDCPFFGSP IPTLRWFKNQGSNLDGGNYHVVYEN		
		501		550
Nfasc 186	(484)	GSLEIKMIRKEDQGIYTCVATNILGAENQVRLEVKDPTRIYRMPEDQVA		
Nfasc 155	(495)	GSLEIKMIRKEDQGIYTCVATNILGAENQVRLEVKDPTRIYRMPEDQVA		
Nfasc Variant 3	(495)	GSLEIKMIRKEDQGIYTCVATNILGAENQVRLEVKDPTRIYRMPEDQVA		
Nfasc Variant 4	(478)	GSLEIKMIRKEDQGIYTCVATNILGAENQVRLEVKDPTRIYRMPEDQVA		
Microglia Nfasc	(448)	GSLEIKMIRKEDQGIYTCVATNILGAENQVRLEVKDPTRIYRMPEDQVA		
		551		600
Nfasc 186	(534)	KRGTTVQLECRVKHDP SLKLT VSWLKDDEPLYIGNRMKKEDDSLTFGVA		
Nfasc 155	(545)	KRGTTVQLECRVKHDP SLKLT VSWLKDDEPLYIGNRMKKEDDSLTFGVA		
Nfasc Variant 3	(545)	KRGTTVQLECRVKHDP SLKLT VSWLKDDEPLYIGNRMKKEDDSLTFGVA		
Nfasc Variant 4	(528)	KRGTTVQLECRVKHDP SLKLT VSWLKDDEPLYIGNRMKKEDDSLTFGVA		
Microglia Nfasc	(498)	KRGTTVQLECRVKHDP SLKLT VSWLKDDEPLYIGNRMKKEDDSLTFGVA		
		601		650
Nfasc 186	(584)	ERDQGSYTCMASTELDQDLAKAYLTVLA	DQATPTNRLAALPKGRPDRPRD	
Nfasc 155	(595)	ERDQGSYTCMASTELDQDLAKAYLTVLA	DQATPTNRLAALPKGRPDRPRD	
Nfasc Variant 3	(595)	ERDQGSYTCMASTELDQDLAKAYLTVLG	-----RPDRPRD	
Nfasc Variant 4	(578)	ERDQGSYTCMASTELDQDLAKAYLTVLG	-----RPDRPRD	
Microglia Nfasc	(548)	ERDQGSYTCMASTELDQDLAKAYLTVLG	-----RPDRPRD	
		651		700
Nfasc 186	(634)	LELTDLAERSVRLTWIPGDDNNSPITDYVVQFEEDQFQPGVWHDSRFPF		
Nfasc 155	(645)	LELTDLAERSVRLTWIPGDDNNSPITDYVVQFEEDQFQPGVWHDSRFPF		
Nfasc Variant 3	(630)	LELTDLAERSVRLTWIPGDDNNSPITDYVVQFEEDQFQPGVWHDSRFPF		
Nfasc Variant 4	(613)	LELTDLAERSVRLTWIPGDDNNSPITDYVVQFEEDQFQPGVWHDSRFPF		
Microglia Nfasc	(583)	LELTDLAERSVRLTWIPGDDNNSPITDYVVQFEEDQFQPGVWHDSRFPF		
		701		750
Nfasc 186	(684)	SVNSAVLHLSPYVNYQFRVIAVNEVGSSHPSLPSERYRTSGAPPESNP	SD	
Nfasc 155	(695)	SVNSAVLHLSPYVNYQFRVIAVNEVGSSHPSLPSERYRTSGAPPESNP	SD	
Nfasc Variant 3	(680)	SVNSAVLHLSPYVNYQFRVIAVNEVGSSHPSLPSERYRTSGAPPESNP	SD	
Nfasc Variant 4	(663)	SVNSAVLHLSPYVNYQFRVIAVNEVGSSHPSLPSERYRTSGAPPESNP	SD	
Microglia Nfasc	(633)	SVNSAVLHLSPYVNYQFRVIAVNEVGSSHPSLPSERYRTSGAPPESNP	SD	
		751		800
Nfasc 186	(734)	VKGEETRKNNMEITWTPMNATSAFGPNLRYIVKWRRRETRETWNNVTVWG		
Nfasc 155	(745)	VKGEETRKNNMEITWTPMNATSAFGPNLRYIVKWRRRETRETWNNVTVWG		
Nfasc Variant 3	(730)	VKGEETRKNNMEITWTPMNATSAFGPNLRYIVKWRRRETRETWNNVTVWG		
Nfasc Variant 4	(713)	VKGEETRKNNMEITWTPMNATSAFGPNLRYIVKWRRRETRETWNNVTVWG		
Microglia Nfasc	(683)	VKGEETRKNNMEITWTPMNATSAFGPNLRYIVKWRRRETRETWNNVTVWG		
		801		850
Nfasc 186	(784)	SRYVVGQTPVYVPYEIRVQAENDFGKGPEPDTIIGYSG	-----	
Nfasc 155	(795)	SRYVVGQTPVYVPYEIRVQAENDFGKGPEPDTIIGYSG	EDYPRAAPTEVK	
Nfasc Variant 3	(780)	SRYVVGQTPVYVPYEIRVQAENDFGKGPEPDTIIGYSG	EDYPRAAPTEVK	
Nfasc Variant 4	(763)	SRYVVGQTPVYVPYEIRVQAENDFGKGPEPDTIIGYSG	EDYPRAAPTEVK	
Microglia Nfasc	(733)	SRYVVGQTPVYVPYEIRVQAENDFGKGPEPDTIIGYSG	EDYPRAAPTEVK	
		851		900
Nfasc 186	(822)	-----		
Nfasc 155	(845)	IRVLNSTAISLQWNRVYSDTVQGQLREYRAYYWRESSLLKNLWVSQKRQQ		
Nfasc Variant 3	(830)	IRVLNSTAISLQWNRVYSDTVQGQLREYRAYYWRESSLLKNLWVSQKRQQ		
Nfasc Variant 4	(813)	IRVLNSTAISLQWNRVYSDTVQGQLREYRAYYWRESSLLKNLWVSQKRQQ		
Microglia Nfasc	(783)	IRVLNSTAISLQWNRVYSDTVQGQLREYRAYYWRESSLLKNLWVSQKRQQ		
		901		950
Nfasc 186	(822)	-----	EDLPS	
Nfasc 155	(895)	ASFPGDRPRGVVARLFPYSNYKLEMVVVNGRGDGRSETKEFTTPEGVPS		

Nfasc Variant 3	(880)	ASFPGDRPRGVVARLFPYSNYKLEMVVVNGRGDGRSETKEFTTPEGVPS	
Nfasc Variant 4	(863)	ASFPGDRPRGVVARLFPYSNYKLEMVVVNGRGDGRSETKEFTTPEGVPS	
Microglia Nfasc	(833)	ASFPGDRPRGVVARLFPYSNYKLEMVVVNGRGDGRSETKEFTTPE	DLPS
		951	1000
Nfasc 186	(827)	APRRFRVRQPNLETINLEWDHPEHPNGILIGYILRYVPFNGTKLGKQMV	E
Nfasc 155	(945)	APRRFRVRQPNLETINLEWDHPEHPNGILIGYILRYVPFNGTKLGKQMV	E
Nfasc Variant 3	(930)	APRRFRVRQPNLETINLEWDHPEHPNGILIGYILRYVPFNGTKLGKQMV	E
Nfasc Variant 4	(913)	APRRFRVRQPNLETINLEWDHPEHPNGILIGYILRYVPFNGTKLGKQMV	E
Microglia Nfasc	(883)	APKRFKVRHPNLETINLEWDHPEHPNGILIGYILRYVPFNGTKLGKQMV	E
		1001	1050
Nfasc 186	(877)	NFSPNQTKFSVQRADPVSRYRFSLSARTQVGSGEAATEESPAAPPNEATPT	
Nfasc 155	(995)	NFSPNQTKFSVQRADPVSRYRFSLSARTQVGSGEAATEESPAAPPNEATPT	
Nfasc Variant 3	(980)	NFSPNQTKFSVQRADPVSRYRFSLSARTQVGSGEAATEESPAAPPNEATPT	
Nfasc Variant 4	(963)	NFSPNQTKFSVQRADPVSRYRFSLSARTQVGSGEAATEESPAAPPNEATPT	
Microglia Nfasc	(933)	NFSPNQTKFSVQRADPVSRYRFSLSARTQVGSGEAATEESPAAPPNEATPT	
		1051	1100
Nfasc 186	(927)	AA PPTLPPTTVGTTGLVSSTDATA LAATSEATTVP I IPTVVPTTVATTIA	
Nfasc 155	(1045)	AA-----	
Nfasc Variant 3	(1030)	AA-----	
Nfasc Variant 4	(1013)	AA-----	
Microglia Nfasc	(983)	AA-----	
		1101	1150
Nfasc 186	(977)	TTTTTTAATTTTTTTE SPPTTAGTKIHETAPDEQSIWNVTVLPNSKWAN	
Nfasc 155	(1047)	-----	
Nfasc Variant 3	(1032)	-----	
Nfasc Variant 4	(1015)	-----	
Microglia Nfasc	(985)	-----	
		1151	1200
Nfasc 186	(1027)	ITWKHNFRPGTDFVVEYIDSNHTKKTVPVKAQAQPIQLTDLFPGMTYTLR	
Nfasc 155	(1047)	-----	
Nfasc Variant 3	(1032)	-----	
Nfasc Variant 4	(1015)	-----	
Microglia Nfasc	(985)	-----	
		1201	1250
Nfasc 186	(1077)	VYSRDNEGISSTVITFMT	STAYTNNQADIATQGWFIGLMCAIALLVLILL
Nfasc 155	(1047)	-----	TAAYTNNQADIATQGWFIGLMCAIALLVLILL
Nfasc Variant 3	(1032)	-----	TAAYTNNQADIATQGWFIGLMCAIALLVLILL
Nfasc Variant 4	(1015)	-----	TAAYTNNQADIATQGWFIGLMCAIALLVLILL
Microglia Nfasc	(985)	-----	STAYTNNQADIATQGWFIGLMCAIALLVLILL
		1251	1300
Nfasc 186	(1127)	IVCFIKRSRGKYPVREKKDVPLGPEDPKEEDGSFDYSDEDNKPLQGSQT	
Nfasc 155	(1076)	IVCFIKRSRGKYPVREKKDVPLGPEDPKEEDGSFDYSDEDNKPLQGSQT	
Nfasc Variant 3	(1061)	IVCFIKRSRGKYPVREKKDVPLGPEDPKEEDGSFDYSDEDNKPLQGSQT	
Nfasc Variant 4	(1044)	IVCFIKRSRGKYPVREKKDVPLGPEDPKEEDGSFDYSDEDNKPLQGSQT	
Microglia Nfasc	(1014)	IVCFIKRSRGKYPVREKKDVPLGPEDPKEEDGSFDYSDEDNKPLQGSQT	
		1301	1350
Nfasc 186	(1177)	SLDGTIKQQESDDSLVDYEGEGGEGQFNEDGSFIGQYTVKKDKETE	EGNES
Nfasc 155	(1126)	SLDGTIKQQESDDSLVDYEGEGGEGQFNEDGSFIGQYTVKKDKETE	EGNES
Nfasc Variant 3	(1111)	SLDGTIKQQESDDSLVDYEGEGGEGQFNEDGSFIGQYTVKKDKETE	EGNES
Nfasc Variant 4	(1094)	SLDGTIKQQESDDSLVDYEGEGGEGQFNEDGSFIGQYTVKKDKETE	EGNES
Microglia Nfasc	(1064)	SLDGTIKQQESDDSLVDYEGEGGEGQFNEDGSFIGQYTVKKDKETE	EGNES
		1351	1364
Nfasc 186	(1227)	SEATSPVNAIYSLA	
Nfasc 155	(1176)	SEATSPVNAIYSLA	
Nfasc Variant 3	(1161)	SEATSPVNAIYSLA	
Nfasc Variant 4	(1144)	SEATSPVNAIYSLA	
Microglia Nfasc	(1114)	SEATSPVNAIYSLA	

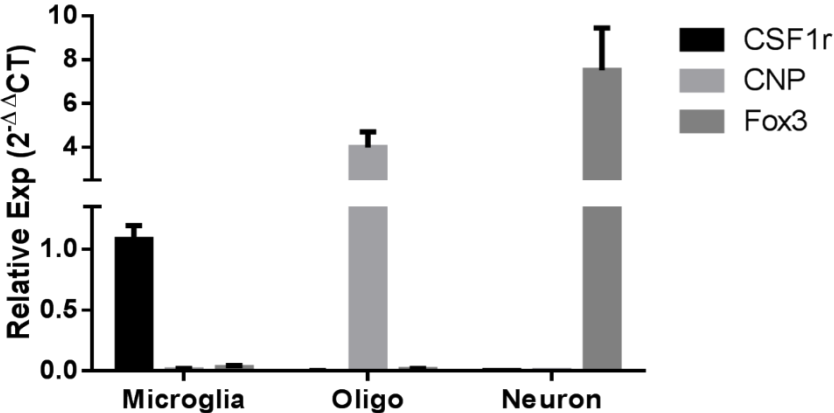
Supplementary Figure 3.1. Sequence Alignment of Translated Nucleotide Sequence of Microglial Nfasc with Published Sequences from NCBI. Microglial Nfasc is similar to Nfasc 186 and Nfasc 155 (yellow), but contains some unique regions (blue). Microglial Nfasc is highly similar to previously identified variant 4 sequence.

Supplementary Figure 3.2



Supplementary Figure 3.2. Microglia are Distinguished from Macrophages and Isolated by FACS. Single-cell suspensions from mouse cortices were stained with BB515-anti-CD45 and APC-anti-CD11b then sorted on a FACS Aria II by gating for CD11b and CD45 high/low expression. A-B, Flow cytometric analysis using isotype controls (A) demonstrated lack of non-specific binding of target antibodies in cortical sample. B, CD11b⁺CD45^{lo} microglia (red) and CD11b⁺CD45^{hi} macrophages (blue) were sorted from EAE-induced mice.

Supplementary Figure 3.3



Supplementary Figure 3.3. Isolated Microglia are Enriched for Microglial Markers but not Oligodendrocyte or Neuronal Markers. Relative expression levels of CSF1r (microglial marker), CNP (oligodendrocyte marker), Fox3 (Neuronal marker) mRNA in FACS-isolated microglia demonstrate isolated cells are enriched for microglia and do not appear to have oligodendrocyte or neuronal contamination.

CHAPTER FOUR

DISCUSSION

4.1 Synopsis

The AIS was characterized and identified as the site of action potential initiation over 50 years ago (Conradi, 1966; Palay et al., 1968); however, it was not until 2006 that the dynamicity of this domain began to be appreciated when Kuba and colleagues (2006) demonstrated in the nucleus laminaris of the chick that the position of the AIS could be regulated for optimal neuron function (Kuba et al., 2006). In 2010, two hallmark papers (Grubb and Burrone, 2010; Kuba et al., 2010) demonstrated that the AIS, though comprised of numerous densely clustered and highly organized proteins, was capable of undergoing significant structural changes. Grubb and Burrone (2010) demonstrated that chronic depolarization of cultured hippocampal neurons induced a distal relocation of the AIS and altered neuronal function. Kuba and colleagues (2010) found that deprivation of auditory input in avian auditory neurons increased AIS length demonstrating that presynaptic activity modulates the properties and structure of the AIS. Since these studies, the structural reorganization and relocation of the AIS have been studied both in the context of development and disease where the AIS has been demonstrated to undergo a number of forms of plasticity such as ion channel switching, changes in ion channel distribution, and altered length and location relative to the soma (Bened-Jensen et al., 2016; Del Puerto et al., 2015; Gutzmann et al., 2014; Hu et al., 2009; Kole et al., 2007; Kuba et al., 2006, 2010, 2015b). AIS plasticity has been observed during development of the avian auditory system where length of AISs is dependent on the sound frequency to which each neuron responds (Kuba et al., 2006). Similarly, in the

rodent visual cortex, AIS length is dynamically regulated throughout development where AISs shorten with the onset of activity (eye opening) and then slowly elongate until the end of the critical period (Gutzmann et al., 2014). These changes suggest that the neuron responds to its environment and fine-tunes excitability, a process described as homeostatic plasticity (Leterrier et al., 2015; Wefelmeyer et al., 2016; Yamada and Kuba, 2016).

In addition to plasticity during developmental, AIS structural changes have also been reported in pathological conditions. In 2009, Schafer et al. showed that AIS integrity was lost following middle cerebral artery occlusion due to irreversible calpain-mediated proteolysis of AIS proteins (Schafer et al., 2009). AIS disruption also occurs in mTBI, Alzheimer's disease, stroke, and MS models (Baalman et al., 2013; Clark et al., 2016; Hinman et al., 2013; Marin et al., 2016; Sohn et al., 2016; Vascak et al., 2017). Similar to the findings of Schafer and colleagues (2009), these studies also reported no reversibility of AIS pathology. A common component of these neuropathological conditions is neuroinflammation; thus, my studies aimed to investigate AIS dynamics throughout various phases of the inflammatory response. Specifically, my studies were designed 1. to provide a better understanding of the neuroinflammatory environment with associated AIS pathology, 2. to identify the underlying mechanisms driving AIS disruption, and 3. to determine if AIS disruption is reversible. My findings revealed that AIS ankG and functional sub-domains are significantly shortened within 6h of the onset of acute inflammation. This alteration precedes the loss of ankG clustering, which occurs in nearly one third of the cortical neurons with sustained inflammation. mRNA and IHC analyses, as well as the use of an anti-inflammatory and free-radical scavenger, implicated ROS

producing enzymes as a potential mediator of AIS disruption. Analyses utilizing NOX2 knockout mice confirmed that NOX2, a major producer of ROS in the CNS, is a mediator of inflammation-induced AIS disruption. Furthermore, using a pharmacological approach I identified the calcium-dependent protease calpain as a mediator of AIS structural disruption. Transcript characterization of the microglial inflammatory profile and analysis of microglia-AIS contact implicated microglia as potentially pivotal regulators of AIS stability; however, no mediator of microglia-AIS contact had been identified. Therefore, I addressed this void in our understanding by identifying the cell adhesion molecule Nfasc as a candidate protein that regulates microglial-AIS interaction.

The studies presented here add to the body of literature investigating AIS plasticity and identify ROS as a novel mediator of AIS disruption. I have identified progressive changes in the AIS architecture including changes to AIS functional sub-domains that correspond to the rise, peak, and resolution of the inflammatory environment. I also describe the novel expression of a cell adhesion molecule, Nfasc, in microglia. Interestingly, the clustering pattern of this novel protein suggests that Nfasc may regulate the interaction of microglia with the AIS, an interaction that may be critical for AIS stability. Furthermore, I have identified a model *in vivo* that allows for the investigation of mechanisms underlying both the disruption and recovery of AIS stability.

4.2 AIS Plasticity in Inflammation: Microglial Contact and Microglial Inflammation

Previous work from our laboratory demonstrated that AISs are disrupted with disease progression and severity in an animal model of Multiple Sclerosis known as EAE

(Clark et al., 2016). Disruption was independent of myelin loss but paralleled inflammation progression. Furthermore, we identified AIS pathology in normal appearing grey matter of post-mortem tissue from patients with MS (Davenne and Lubetzki, unpublished; Clark and Dupree, unpublished). These findings suggest that AIS disruption is a primary axonal pathology in EAE and MS and may be a novel therapeutic target. However, it is important to remember that AIS disruption is not limited to MS and its models, since this axonal pathology occurs in other neuropathological environments (Harty et al., 2013; Hinman et al., 2013; Marin et al., 2016; Schafer et al., 2009; Sohn et al., 2016; Vascak et al., 2017) and can be induced *in vitro* by altering axonal activity or by exposure to pathological stressors (Bened-Jensen et al., 2016; Clark et al., 2017; Del Puerto et al., 2015; Evans et al., 2013, 2015; Grubb and Burrone, 2010).

Although numerous studies have shown the loss of AIS integrity using both *in vivo* and *in vitro* models, the investigation of reversibility or recovery of AIS disruption has been limited to *in vitro* systems (Evans et al., 2015; Grubb and Burrone, 2010); thus, it remained to be shown that recovery occurred *in vivo*. My work addressed this question by using an acute inflammatory model as a tool to investigate how neuroinflammation affects AIS structure/stability. I found that early in the inflammatory response, subtle changes in AIS functional sub-domains are induced; Nav1.6 and Kv1.2 AIS sub-domains are shortened consistent with changes seen in response to enhanced neuronal activity (reviewed in Jamann et al., 2017). Furthermore, following peak microglial inflammation, loss of AIS ankG detection suggested a progressive and continued AIS disruption. Importantly, AIS disruption was reversed following resolution of the microglial inflammatory response and amelioration of the inflammatory environment using anti-inflammatory treatment, which

together identified the AIS as a potential therapeutic target in neuropathological conditions.

In addition to determining the reparative potential of AIS structure, my work aimed to understand the driving factors of inflammation-induced AIS disruption. Previous work from our lab suggested that microglia play a role in AIS stability and contribute to pathology during chronic inflammation. We demonstrated that AISs are increasingly contacted by microglia in inflammatory conditions present in both EAE and cuprizone models of MS; however, disruption to the AIS only occurred in the EAE model suggesting that contact alone does not drive AIS disruption (Clark et al., 2016). Utilizing an acute neuroinflammatory model, I elucidated that while microglia contact AISs, alterations in the microglial inflammatory profile correlated with AIS disruption and recovery suggesting that rather than contact itself, the phenotype of the microglia in close proximity drive AIS changes. This possibility is supported by my experiments that demonstrated microglial NOX2 expression correlated with AIS changes and that NOX2 knockout mice exhibit microglial-AIS contact; however, LPS-induced AIS disruption was prevented. Furthermore, *in vitro* studies from our laboratory indicated that ROS induced AIS disruption in cortical neurons in a calpain-dependent manner (Clark et al., 2017) similar to that observed in my study (Chapter 2; (Benusa et al., 2017)). Interestingly, microglial contact (Yamasaki et al., 2014), ROS (Guemez-Gamboa et al., 2011; Haider et al., 2011; Ohl et al., 2016), and calpain- (Das et al., 2013; Guyton et al., 2005; Trager et al., 2014) dependent mechanisms have also been implicated in other axonal pathologies described in MS suggesting that a common mechanism may underlie axonal disruptions. These findings of microglia driving neuronal pathology are consistent with literature that has

implicated pro-inflammatory microglia in the progression of a number of neuropathological environments (Edison et al., 2008; Gomez-Nicola and Perry, 2015; Johnson et al., 2013; Ohl et al., 2016; Russo and McGavern, 2016).

While pro-inflammatory microglia interact with neurons and exert deleterious effects, the presence of microglia at the AIS may instead confer protection. Microglia are highly dynamic cells rapidly extending processes and surveying their environment and microglial process dynamics are altered following changes in neuronal activity. For example, microglial-synapse contact in the zebrafish tectum increased with neuronal activity. Contacted neurons exhibited decreased activity, while noncontacted neurons maintained an increased firing rate (Li et al., 2012). In a model of kainate-induced seizure activity, microglia extended their processes to sites of ATP release and increased neuronal contact with enhanced firing, and inhibition of the microglial response in mice lacking P2Y12 exacerbated seizures (Eyo et al., 2014). Additionally, when repeated stimulations were used to induce neuronal hyperexcitability, microglia extended their processes and wrapped around axons (Kato et al., 2016). This induced a rapid repolarization in the neuron back to resting value and when microglial migration was pharmacologically blocked, activity-induced depolarization continued until cell death ensued (Kato et al., 2016). These studies suggest that microglial-neuronal contact is neuroprotective in cases of neuronal hyperexcitation. Interestingly, our AIS structural findings indicated a change that is consistent with alterations seen in response to hyperexcitable environments (reviewed in Jamann et al., 2017).

4.3 Future Directions

It remains to be determined the nature of microglial-AIS contact and whether loss of contact would improve or worsen AIS pathology. To begin to address this overarching question, a candidate molecule mediating the interaction between microglia and the AIS needed to be identified. My experiments revealed that a novel isoform of Nfasc, a CAM important in regulating axonal domain stability and axo-glial interactions (Pillai et al., 2009; Sherman et al., 2005), is expressed by microglia. Furthermore, Nfasc was upregulated concomitant with enhanced microglial-AIS association and localized to the microglial-AIS interface identifying this microglia protein as a novel candidate in AIS contact. Further studies investigating the effects of loss of microglial Nfasc will begin to elucidate its role, if any, in microglial-AIS interaction and whether this interaction is important for stabilizing AIS activity.

We have described AIS structural plasticity in the presence of acute neuroinflammation where both ankG clustering and functional sub-domain clustering is altered and restored. These kinds of changes are consistent with homeostatic plasticity where neurons fine tune their excitability by altering AIS structure. While our data indicate a response to enhanced neuronal input, which occurs as a means to decrease neuronal activity, we do not know if there are functional consequences of the observed structural changes. Therefore, future experiments measuring function throughout the inflammatory response will be of value. To do this, electrophysiological recordings of cortical neurons from control or LPS-injected mice at time points investigated here would allow us to pair inflammation-induced AIS structural changes with functional consequences both at the cellular level and circuitry level.

While we have established that loss of AIS protein clustering is reversible after an acute neuroinflammatory insult, it is unclear whether the capability to recover is diminished after a greater insult or repeated insults. I attempted to answer one of these questions by using a larger inflammatory insult induced by administering an LPS dose of 10mg/kg.; however, at 2 weeks post-injection, loss of AIS ankG clustering was still reversed. These data suggested that inflammation induced by increased bacterial insult in the periphery was not sufficient to induce irreversible AIS damage. A future experiment investigating the effects of repeated insult would be interesting. This would mimic a relapse-remitting phenotype present in MS patients who experience multiple inflammatory attacks throughout disease course where recovery potential is lessened as disease progresses. To do this, multiple low dose LPS injections could be used or an animal model of EAE that displays a relapse-remitting phenotype would allow a chronic evaluation that is more disease specific.

4.4 Concluding Remarks

My work identifies the AIS as a viable therapeutic target in neuroinflammatory conditions and identifies ROS as an important mediator of inflammation-induced AIS disruption. Furthermore, my work establishes microglia as a potentially pivotal mediator of AIS stability. I show that microglia make direct contact with the AIS, changes in their inflammatory profile tracks closely with changes in AIS structure, and microglial inflammatory factors such as NOX2 drive AIS alterations. Future studies are needed to address the nature of microglia-AIS association and whether AIS structural changes are adaptive or maladaptive. These answers will be important in honing our search for novel

therapeutics in inflammatory conditions present in neurodegenerative disease such as multiple sclerosis.

LIST OF REFERENCES

- Aarts, M.M., and Tymianski, M. (2005). TRPM7 and ischemic CNS injury. *Neurosci. Rev. J. Bringing Neurobiol. Neurol. Psychiatry* 11, 116–123.
- Aarts, E., Verhage, M., Veenvliet, J.V., Dolan, C.V., and van der Sluis, S. (2014). A solution to dependency: using multilevel analysis to accommodate nested data. *Nat. Neurosci.* 17, 491–496.
- Aguzzi, A., Barres, B.A., and Bennett, M.L. (2013). Microglia: scapegoat, saboteur, or something else? *Science* 339, 156–161.
- Ango, F., di Cristo, G., Higashiyama, H., Bennett, V., Wu, P., and Huang, Z.J. (2004). Ankyrin-based subcellular gradient of neurofascin, an immunoglobulin family protein, directs GABAergic innervation at purkinje axon initial segment. *Cell* 119, 257–272.
- Anrather, J., Racchumi, G., and Iadecola, C. (2006). NF-kappaB regulates phagocytic NADPH oxidase by inducing the expression of gp91phox. *J. Biol. Chem.* 281, 5657–5667.
- Atapour, N., and Rosa, M.G.P. (2017). Age-related plasticity of the axon initial segment of cortical pyramidal cells in marmoset monkeys. *Neurobiol. Aging* 57, 95–103.
- Baalman, K., Marin, M.A., Ho, T.S.-Y., Godoy, M., Cherian, L., Robertson, C., and Rasband, M.N. (2015). Axon initial segment-associated microglia. *J. Neurosci. Off. J. Soc. Neurosci.* 35, 2283–2292.
- Baalman, K.L., Cotton, R.J., Rasband, S.N., and Rasband, M.N. (2013). Blast wave exposure impairs memory and decreases axon initial segment length. *J. Neurotrauma* 30, 741–751.
- Banerjee, S., Sousa, A.D., and Bhat, M.A. (2006). Organization and function of septate junctions: an evolutionary perspective. *Cell Biochem. Biophys.* 46, 65–77.
- Baranauskas, G., David, Y., and Fleidervish, I.A. (2013). Spatial mismatch between the Na⁺ flux and spike initiation in axon initial segment. *Proc. Natl. Acad. Sci. U. S. A.* 110, 4051–4056.
- Basak, S., Raju, K., Babiarz, J., Kane-Goldsmith, N., Koticha, D., and Grumet, M. (2007). Differential expression and functions of neuronal and glial neurofascin isoforms and splice variants during PNS development. *Dev. Biol.* 311, 408–422.
- Bateman, A., Jouet, M., MacFarlane, J., Du, J.S., Kenwrick, S., and Chothia, C. (1996). Outline structure of the human L1 cell adhesion molecule and the sites where mutations cause neurological disorders. *EMBO J.* 15, 6050–6059.

Bender, K.J., Ford, C.P., and Trussell, L.O. (2010). Dopaminergic Modulation of Axon Initial Segment Calcium Channels Regulates Action Potential Initiation. *Neuron* 68, 500–511.

Bened-Jensen, T., Christensen, R.K., Denti, F., Perrier, J.-F., Rasmussen, H.B., and Olesen, S.-P. (2016). Live Imaging of Kv7.2/7.3 Cell Surface Dynamics at the Axon Initial Segment: High Steady-State Stability and Calpain-Dependent Excitotoxic Downregulation Revealed. *J. Neurosci. Off. J. Soc. Neurosci.* 36, 2261–2266.

Bennett, V., and Baines, A.J. (2001). Spectrin and ankyrin-based pathways: metazoan inventions for integrating cells into tissues. *Physiol. Rev.* 81, 1353–1392.

Bennett, M.L., Bennett, F.C., Liddel, S.A., Ajami, B., Zamanian, J.L., Fernhoff, N.B., Mulinyawe, S.B., Bohlen, C.J., Adil, A., Tucker, A., et al. (2016). New tools for studying microglia in the mouse and human CNS. *Proc. Natl. Acad. Sci. U. S. A.* 113, E1738–1746.

Benusa, S.D., George, N.M., Sword, B.A., DeVries, G.H., and Dupree, J.L. (2017). Acute neuroinflammation induces AIS structural plasticity in a NOX2-dependent manner. *J. Neuroinflammation* 14, 116.

Bercury, K.K., and Macklin, W.B. (2015). Dynamics and mechanisms of CNS myelination. *Dev. Cell* 32, 447–458.

von Bernhardi, R., Eugenín-von Bernhardi, J., Flores, B., and Eugenín León, J. (2016a). Glial Cells and Integrity of the Nervous System. *Adv. Exp. Med. Biol.* 949, 1–24.

von Bernhardi, R., Heredia, F., Salgado, N., and Muñoz, P. (2016b). Microglia Function in the Normal Brain. *Adv. Exp. Med. Biol.* 949, 67–92.

Bilimoria, P.M., and Stevens, B. (2015). Microglia function during brain development: New insights from animal models. *Brain Res.* 1617, 7–17.

Block, M.L., Zecca, L., and Hong, J.-S. (2007). Microglia-mediated neurotoxicity: uncovering the molecular mechanisms. *Nat. Rev. Neurosci.* 8, 57–69.

Bordt, E.A., and Polster, B.M. (2014). NADPH oxidase- and mitochondria-derived reactive oxygen species in proinflammatory microglial activation: a bipartisan affair? *Free Radic. Biol. Med.* 76, 34–46.

Buffington, S.A., and Rasband, M.N. (2011). The axon initial segment in nervous system disease and injury. *Eur. J. Neurosci.* 34, 1609–1619.

Chand, A.N., Galliano, E., Chesters, R.A., and Grubb, M.S. (2015). A distinct subtype of dopaminergic interneuron displays inverted structural plasticity at the axon initial segment. *J. Neurosci. Off. J. Soc. Neurosci.* 35, 1573–1590.

Charles, P., Tait, S., Faivre-Sarrailh, C., Barbin, G., Gunn-Moore, F., Denisenko-Nehrbass, N., Guennoc, A.-M., Girault, J.-A., Brophy, P.J., and Lubetzki, C. (2002). Neurofascin is a glial receptor for the paranodin/Caspr-contactin axonal complex at the axoglial junction. *Curr. Biol. CB* 12, 217–220.

Chen, S.-H., Oyarzabal, E.A., and Hong, J.-S. (2016). Critical role of the Mac1/NOX2 pathway in mediating reactive microgliosis-generated chronic neuroinflammation and progressive neurodegeneration. *Curr. Opin. Pharmacol.* 26, 54–60.

Cherry, J.D., Olschowka, J.A., and O'Banion, M.K. (2014). Neuroinflammation and M2 microglia: the good, the bad, and the inflamed. *J. Neuroinflammation* 11, 98.

Choi, D.C., Lee, J.Y., Lim, E.J., Baik, H.H., Oh, T.H., and Yune, T.Y. (2012). Inhibition of ROS-induced p38MAPK and ERK activation in microglia by acupuncture relieves neuropathic pain after spinal cord injury in rats. *Exp. Neurol.* 236, 268–282.

Clark, B.D., Goldberg, E.M., and Rudy, B. (2009). Electrogenic tuning of the axon initial segment. *Neurosci. Rev. J. Bringing Neurobiol. Neurol. Psychiatry* 15, 651–668.

Clark, K., Sword, B.A., and Dupree, J.L. (2017). Oxidative Stress Induces Disruption of the Axon Initial Segment. *ASN Neuro* 9, 1759091417745426.

Clark, K.C., Josephson, A., Benusa, S.D., Hartley, R.K., Baer, M., Thummala, S., Joslyn, M., Sword, B.A., Elford, H., Oh, U., et al. (2016). Compromised axon initial segment integrity in EAE is preceded by microglial reactivity and contact. *Glia* 64, 1190–1209.

Colbert, C.M., and Pan, E. (2002). Ion channel properties underlying axonal action potential initiation in pyramidal neurons. *Nat. Neurosci.* 5, 533–538.

Collinson, J.M., Marshall, D., Gillespie, C.S., and Brophy, P.J. (1998). Transient expression of neurofascin by oligodendrocytes at the onset of myelinogenesis: implications for mechanisms of axon-glial interaction. *Glia* 23, 11–23.

Conradi, S. (1966). Ultrastructural specialization of the initial axon segment of cat lumbar motoneurons. Preliminary observations. *Acta Soc. Med. Ups.* 71, 281–284.

Crotti, A., and Ransohoff, R.M. (2016a). Microglial Physiology and Pathophysiology: Insights from Genome-wide Transcriptional Profiling. *Immunity* 44, 505–515.

Crotti, A., and Ransohoff, R.M. (2016b). Microglial Physiology and Pathophysiology: Insights from Genome-wide Transcriptional Profiling. *Immunity* 44, 505–515.

Das, A., Guyton, M.K., Smith, A., Wallace, G., McDowell, M.L., Matzelle, D.D., Ray, S.K., and Banik, N.L. (2013). Calpain inhibitor attenuated optic nerve damage in acute optic neuritis in rats. *J. Neurochem.* 124, 133–146.

- Davalos, D., Grutzendler, J., Yang, G., Kim, J.V., Zuo, Y., Jung, S., Littman, D.R., Dustin, M.L., and Gan, W.-B. (2005). ATP mediates rapid microglial response to local brain injury *in vivo*. *Nat. Neurosci.* *8*, 752–758.
- Davis, J.Q., and Bennett, V. (1993). Ankyrin-binding activity of nervous system cell adhesion molecules expressed in adult brain. *J. Cell Sci. Suppl.* *17*, 109–117.
- Davis, J.Q., and Bennett, V. (1994). Ankyrin binding activity shared by the neurofascin/L1/NrCAM family of nervous system cell adhesion molecules. *J. Biol. Chem.* *269*, 27163–27166.
- Davis, J.Q., McLaughlin, T., and Bennett, V. (1993). Ankyrin-binding proteins related to nervous system cell adhesion molecules: candidates to provide transmembrane and intercellular connections in adult brain. *J. Cell Biol.* *121*, 121–133.
- Davis, J.Q., Lambert, S., and Bennett, V. (1996). Molecular composition of the node of Ranvier: identification of ankyrin-binding cell adhesion molecules neurofascin (mucin+/third FNIII domain-) and NrCAM at nodal axon segments. *J. Cell Biol.* *135*, 1355–1367.
- De Angelis, E., Watkins, A., Schäfer, M., Brümmendorf, T., and Kenwrick, S. (2002). Disease-associated mutations in L1 CAM interfere with ligand interactions and cell-surface expression. *Hum. Mol. Genet.* *11*, 1–12.
- De Jager, P.L., Srivastava, G., Lunnon, K., Burgess, J., Schalkwyk, L.C., Yu, L., Eaton, M.L., Keenan, B.T., Ernst, J., McCabe, C., et al. (2014). Alzheimer's disease: early alterations in brain DNA methylation at *ANK1*, *BIN1*, *RHBDF2* and other loci. *Nat. Neurosci.* *17*, 1156–1163.
- Del Puerto, A., Fronzaroli-Molinieres, L., Perez-Alvarez, M.J., Giraud, P., Carlier, E., Wandosell, F., Debanne, D., and Garrido, J.J. (2015). ATP-P2X7 Receptor Modulates Axon Initial Segment Composition and Function in Physiological Conditions and Brain Injury. *Cereb. Cortex N. Y. N 1991* *25*, 2282–2294.
- Desmazieres, A., Zonta, B., Zhang, A., Wu, L.-M.N., Sherman, D.L., and Brophy, P.J. (2014). Differential stability of PNS and CNS nodal complexes when neuronal neurofascin is lost. *J. Neurosci. Off. J. Soc. Neurosci.* *34*, 5083–5088.
- DeVries, G.H., Farrer, R., Papadopoulos, C., Campbell, C., Litz, J., Paletta, J., Dupree, J., and Elford, H. (2012). Didox-A Multipotent Drug for Treating Demyelinating disease. *FASEB J.* *26*, 341.4-341.4.
- DiSabato, D.J., Quan, N., and Godbout, J.P. (2016). Neuroinflammation: the devil is in the details. *J. Neurochem.* *139 Suppl 2*, 136–153.
- Dodson, P.D., Barker, M.C., and Forsythe, I.D. (2002). Two heteromeric Kv1 potassium channels differentially regulate action potential firing. *J. Neurosci. Off. J. Soc. Neurosci.* *22*, 6953–6961.

- Domingues, H.S., Portugal, C.C., Socodato, R., and Relvas, J.B. (2016). Oligodendrocyte, Astrocyte, and Microglia Crosstalk in Myelin Development, Damage, and Repair. *Front. Cell Dev. Biol.* 4, 71.
- von Drygalski, A., Furlan-Freguia, C., Ruf, W., Griffin, J.H., and Mosnier, L.O. (2013). Organ-specific protection against LPS-induced vascular leak is dependent on the endothelial protein C receptor (EPCR). *Arterioscler. Thromb. Vasc. Biol.* 33, 769–776.
- Dupree, J.L., Girault, J.A., and Popko, B. (1999). Axo-glial interactions regulate the localization of axonal paranodal proteins. *J. Cell Biol.* 147, 1145–1152.
- Ebel, J., Beuter, S., Wuchter, J., Kriebel, M., and Volkmer, H. (2014). Organisation and control of neuronal connectivity and myelination by cell adhesion molecule neurofascin. *Adv. Neurobiol.* 8, 231–247.
- Edison, P., Archer, H.A., Gerhard, A., Hinz, R., Pavese, N., Turkheimer, F.E., Hammers, A., Tai, Y.F., Fox, N., Kennedy, A., et al. (2008). Microglia, amyloid, and cognition in Alzheimer's disease: An [11C](R)PK11195-PET and [11C]PIB-PET study. *Neurobiol. Dis.* 32, 412–419.
- Elford, H., Lee, R., Turchan, J., Gallicchio, V., Ussery, M., Hiscott, J., and Nath, A. (2007). The Virtues of Unique Ribonucleotide Reductase Inhibitors Didox and Trimidox for Retrovirus Therapy. *Antiviral Res.* 74, A65–A66.
- Evans, M.D., Sammons, R.P., Lebron, S., Dumitrescu, A.S., Watkins, T.B.K., Uebele, V.N., Renger, J.J., and Grubb, M.S. (2013). Calcineurin signaling mediates activity-dependent relocation of the axon initial segment. *J. Neurosci. Off. J. Soc. Neurosci.* 33, 6950–6963.
- Evans, M.D., Dumitrescu, A.S., Kruijssen, D.L.H., Taylor, S.E., and Grubb, M.S. (2015). Rapid Modulation of Axon Initial Segment Length Influences Repetitive Spike Firing. *Cell Rep.* 13, 1233–1245.
- Eyo, U.B., Peng, J., Swiatkowski, P., Mukherjee, A., Bispo, A., and Wu, L.-J. (2014). Neuronal hyperactivity recruits microglial processes via neuronal NMDA receptors and microglial P2Y12 receptors after status epilepticus. *J. Neurosci. Off. J. Soc. Neurosci.* 34, 10528–10540.
- Feinberg, K., Eshed-Eisenbach, Y., Frechter, S., Amor, V., Salomon, D., Sabanay, H., Dupree, J.L., Grumet, M., Brophy, P.J., Shrager, P., et al. (2010). A glial signal consisting of gliomedin and NrCAM clusters axonal Na⁺ channels during the formation of nodes of Ranvier. *Neuron* 65, 490–502.
- Feissner, R.F., Skalska, J., Gaum, W.E., and Sheu, S.-S. (2009). Crosstalk signaling between mitochondrial Ca²⁺ and ROS. *Front. Biosci. Landmark Ed.* 14, 1197–1218.
- Felding-Habermann, B., Silletti, S., Mei, F., Siu, C.H., Yip, P.M., Brooks, P.C., Cheresch, D.A., O'Toole, T.E., Ginsberg, M.H., and Montgomery, A.M. (1997). A single

immunoglobulin-like domain of the human neural cell adhesion molecule L1 supports adhesion by multiple vascular and platelet integrins. *J. Cell Biol.* 139, 1567–1581.

Fontainhas, A.M., Wang, M., Liang, K.J., Chen, S., Mettu, P., Damani, M., Fariss, R.N., Li, W., and Wong, W.T. (2011). Microglial Morphology and Dynamic Behavior Is Regulated by Ionotropic Glutamatergic and GABAergic Neurotransmission. *PLOS ONE* 6, e15973.

Frühbeis, C., Fröhlich, D., Kuo, W.P., Amphornrat, J., Thilemann, S., Saab, A.S., Kirchhoff, F., Möbius, W., Goebbels, S., Nave, K.-A., et al. (2013). Neurotransmitter-triggered transfer of exosomes mediates oligodendrocyte-neuron communication. *PLoS Biol.* 11, e1001604.

Garver, T.D., Ren, Q., Tuvia, S., and Bennett, V. (1997). Tyrosine phosphorylation at a site highly conserved in the L1 family of cell adhesion molecules abolishes ankyrin binding and increases lateral mobility of neurofascin. *J. Cell Biol.* 137, 703–714.

Gasser, A., Ho, T.S.-Y., Cheng, X., Chang, K.-J., Waxman, S.G., Rasband, M.N., and Dib-Hajj, S.D. (2012). An ankyrinG-binding motif is necessary and sufficient for targeting Nav1.6 sodium channels to axon initial segments and nodes of Ranvier. *J. Neurosci. Off. J. Soc. Neurosci.* 32, 7232–7243.

Geiss, G.K., Bumgarner, R.E., Birditt, B., Dahl, T., Dowidar, N., Dunaway, D.L., Fell, H.P., Ferree, S., George, R.D., Grogan, T., et al. (2008). Direct multiplexed measurement of gene expression with color-coded probe pairs. *Nat. Biotechnol.* 26, 317–325.

Giannoni, P., Badaut, J., Dargazanli, C., Maudave, A.F.D., Klement, W., Costalat, V., and Marchi, N. (2018). The pericyte–glia interface at the blood–brain barrier. *Clin. Sci.* 132, 361–374.

Gibson, E.M., Purger, D., Mount, C.W., Goldstein, A.K., Lin, G.L., Wood, L.S., Inema, I., Miller, S.E., Bieri, G., Zuchero, J.B., et al. (2014). Neuronal activity promotes oligodendrogenesis and adaptive myelination in the mammalian brain. *Science* 344, 1252304.

Goldberg, E.M., Clark, B.D., Zaghera, E., Nahmani, M., Erisir, A., and Rudy, B. (2008). K⁺ channels at the axon initial segment dampen near-threshold excitability of neocortical fast-spiking GABAergic interneurons. *Neuron* 58, 387–400.

Gollan, L., Salomon, D., Salzer, J.L., and Peles, E. (2003). Caspr regulates the processing of contactin and inhibits its binding to neurofascin. *J. Cell Biol.* 163, 1213–1218.

Gomez-Nicola, D., and Perry, V.H. (2015). Microglial dynamics and role in the healthy and diseased brain: a paradigm of functional plasticity. *Neurosci. Rev. J. Bringing Neurobiol. Neurol. Psychiatry* 21, 169–184.

Grubb, M.S., and Burrone, J. (2010). Activity-dependent relocation of the axon initial segment fine-tunes neuronal excitability. *Nature* 465, 1070–1074.

Guemez-Gamboa, A., Estrada-Sánchez, A.M., Montiel, T., Páramo, B., Massieu, L., and Morán, J. (2011). Activation of NOX2 by the stimulation of ionotropic and metabotropic glutamate receptors contributes to glutamate neurotoxicity in vivo through the production of reactive oxygen species and calpain activation. *J. Neuropathol. Exp. Neurol.* 70, 1020–1035.

Gutzmann, A., Ergül, N., Grossmann, R., Schultz, C., Wahle, P., and Engelhardt, M. (2014). A period of structural plasticity at the axon initial segment in developing visual cortex. *Front. Neuroanat.* 8, 11.

Guyton, M.K., Wingrave, J.M., Yallapragada, A.V., Wilford, G.G., Sribnick, E.A., Matzelle, D.D., Tyor, W.R., Ray, S.K., and Banik, N.L. (2005). Upregulation of calpain correlates with increased neurodegeneration in acute experimental auto-immune encephalomyelitis. *J. Neurosci. Res.* 81, 53–61.

Guyton, M.K., Das, A., Samantaray, S., Wallace, G.C., Butler, J.T., Ray, S.K., and Banik, N.L. (2010). Calpeptin attenuated inflammation, cell death, and axonal damage in animal model of multiple sclerosis. *J. Neurosci. Res.* 88, 2398–2408.

Hahn, Y.K., Podhaizer, E.M., Farris, S.P., Miles, M.F., Hauser, K.F., and Knapp, P.E. (2015). Effects of chronic HIV-1 Tat exposure in the CNS: heightened vulnerability of males versus females to changes in cell numbers, synaptic integrity, and behavior. *Brain Struct. Funct.* 220, 605–623.

Haider, L., Fischer, M.T., Frischer, J.M., Bauer, J., Höftberger, R., Botond, G., Esterbauer, H., Binder, C.J., Witztum, J.L., and Lassmann, H. (2011). Oxidative damage in multiple sclerosis lesions. *Brain* 134, 1914–1924.

Hall, H., Bozic, D., Fauser, C., and Engel, J. (2000). Trimerization of cell adhesion molecule L1 mimics clustered L1 expression on the cell surface: influence on L1-ligand interactions and on promotion of neurite outgrowth. *J. Neurochem.* 75, 336–346.

Hamada, M.S., and Kole, M.H.P. (2015). Myelin loss and axonal ion channel adaptations associated with gray matter neuronal hyperexcitability. *J. Neurosci. Off. J. Soc. Neurosci.* 35, 7272–7286.

Harty, R.C., Kim, T.H., Thomas, E.A., Cardamone, L., Jones, N.C., Petrou, S., and Wimmer, V.C. (2013). Axon initial segment structural plasticity in animal models of genetic and acquired epilepsy. *Epilepsy Res.* 105, 272–279.

Haspel, J., and Grumet, M. (2003). The L1CAM extracellular region: a multi-domain protein with modular and cooperative binding modes. *Front. Biosci. J. Virtual Libr.* 8, s1210-1225.

- Hassel, B., Rathjen, F.G., and Volkmer, H. (1997). Organization of the neurofascin gene and analysis of developmentally regulated alternative splicing. *J. Biol. Chem.* *272*, 28742–28749.
- Hedstrom, K.L., and Rasband, M.N. (2006). Intrinsic and extrinsic determinants of ion channel localization in neurons. *J. Neurochem.* *98*, 1345–1352.
- Hedstrom, K.L., Xu, X., Ogawa, Y., Frischknecht, R., Seidenbecher, C.I., Shrager, P., and Rasband, M.N. (2007). Neurofascin assembles a specialized extracellular matrix at the axon initial segment. *J. Cell Biol.* *178*, 875–886.
- Hedstrom, K.L., Ogawa, Y., and Rasband, M.N. (2008). AnkyrinG is required for maintenance of the axon initial segment and neuronal polarity. *J. Cell Biol.* *183*, 635–640.
- Hines, J.H., Ravanelli, A.M., Schwandt, R., Scott, E.K., and Appel, B. (2015). Neuronal activity biases axon selection for myelination in vivo. *Nat. Neurosci.* *18*, 683–689.
- Hinman, J.D., Rasband, M.N., and Carmichael, S.T. (2013). Remodeling of the Axon Initial Segment After Focal Cortical and White Matter Stroke. *Stroke* *44*, 182–189.
- Hool, L.C. (2008). Evidence for the regulation of L-type Ca²⁺ channels in the heart by reactive oxygen species: mechanism for mediating pathology. *Clin. Exp. Pharmacol. Physiol.* *35*, 229–234.
- Hool, L.C., and Arthur, P.G. (2002). Decreasing Cellular Hydrogen Peroxide With Catalase Mimics the Effects of Hypoxia on the Sensitivity of the L-Type Ca²⁺ Channel to β -Adrenergic Receptor Stimulation in Cardiac Myocytes. *Circ. Res.* *91*, 601–609.
- Hortsch, M. (1996). The L1 family of neural cell adhesion molecules: old proteins performing new tricks. *Neuron* *17*, 587–593.
- Hortsch, M. (2000). Structural and functional evolution of the L1 family: are four adhesion molecules better than one? *Mol. Cell. Neurosci.* *15*, 1–10.
- Hortsch, M., Nagaraj, K., and Mualla, R. (2014). The L1 family of cell adhesion molecules: a sickening number of mutations and protein functions. *Adv. Neurobiol.* *8*, 195–229.
- Hu, W., Tian, C., Li, T., Yang, M., Hou, H., and Shu, Y. (2009). Distinct contributions of Na(v)1.6 and Na(v)1.2 in action potential initiation and backpropagation. *Nat. Neurosci.* *12*, 996–1002.
- Huang, D.W., Sherman, B.T., and Lempicki, R.A. (2009a). Bioinformatics enrichment tools: paths toward the comprehensive functional analysis of large gene lists. *Nucleic Acids Res.* *37*, 1–13.

- Huang, D.W., Sherman, B.T., and Lempicki, R.A. (2009b). Systematic and integrative analysis of large gene lists using DAVID bioinformatics resources. *Nat. Protoc.* **4**, 44–57.
- Hudasek, K., Brown, S.T., and Fearon, I.M. (2004). H₂O₂ regulates recombinant Ca²⁺-channel α 1C subunits but does not mediate their sensitivity to acute hypoxia. *Biochem. Biophys. Res. Commun.* **318**, 135–141.
- Inayat, M.S., Chendil, D., Mohiuddin, M., Elford, H.L., Gallicchio, V.S., and Ahmed, M.M. (2002). Didox (a novel ribonucleotide reductase inhibitor) overcomes Bcl-2 mediated radiation resistance in prostate cancer cell line PC-3. *Cancer Biol. Ther.* **1**, 539–545.
- Inayat, M.S., El-Amouri, I.S., Bani-Ahmad, M., Elford, H.L., Gallicchio, V.S., and Oakley, O.R. (2010). Inhibition of allogeneic inflammatory responses by the Ribonucleotide Reductase Inhibitors, Didox and Trimidox. *J. Inflamm. Lond. Engl.* **7**, 43.
- Itoh, K., Cheng, L., Kamei, Y., Fushiki, S., Kamiguchi, H., Gutwein, P., Stoeck, A., Arnold, B., Altevogt, P., and Lemmon, V. (2004). Brain development in mice lacking L1-L1 homophilic adhesion. *J. Cell Biol.* **165**, 145–154.
- Jamann, N., Jordan, M., and Engelhardt, M. (2017). Activity-dependent axonal plasticity in sensory systems. *Neuroscience*.
- Jenkins, S.M., and Bennett, V. (2001). Ankyrin-G coordinates assembly of the spectrin-based membrane skeleton, voltage-gated sodium channels, and L1 CAMs at Purkinje neuron initial segments. *J. Cell Biol.* **155**, 739–746.
- Jenkins, S.M., and Bennett, V. (2002). Developing nodes of Ranvier are defined by ankyrin-G clustering and are independent of paranodal axoglial adhesion. *Proc. Natl. Acad. Sci. U. S. A.* **99**, 2303–2308.
- Johnson, V.E., Stewart, J.E., Begbie, F.D., Trojanowski, J.Q., Smith, D.H., and Stewart, W. (2013). Inflammation and white matter degeneration persist for years after a single traumatic brain injury. *Brain* **136**, 28–42.
- Kaphzan, H., Buffington, S.A., Jung, J.I., Rasband, M.N., and Klann, E. (2011). Alterations in intrinsic membrane properties and the axon initial segment in a mouse model of Angelman syndrome. *J. Neurosci. Off. J. Soc. Neurosci.* **31**, 17637–17648.
- Kato, G., Inada, H., Wake, H., Akiyoshi, R., Miyamoto, A., Eto, K., Ishikawa, T., Moorhouse, A.J., Strassman, A.M., and Nabekura, J. (2016). Microglial Contact Prevents Excess Depolarization and Rescues Neurons from Excitotoxicity. *ENeuro* **3**, ENEURO.0004-16.2016.
- Kettenmann, H., Kirchhoff, F., and Verkhratsky, A. (2013). Microglia: New Roles for the Synaptic Stripper. *Neuron* **77**, 10–18.

- Kierdorf, K., and Prinz, M. (2013). Factors regulating microglia activation. *Front. Cell. Neurosci.* 7, 44.
- Kim, C., Cho, E.-D., Kim, H.-K., You, S., Lee, H.-J., Hwang, D., and Lee, S.-J. (2014). β 1-integrin-dependent migration of microglia in response to neuron-released α -synuclein. *Exp. Mol. Med.* 46, e91.
- Kirschbaum, K., Kriebel, M., Kranz, E.U., Pötz, O., and Volkmer, H. (2009). Analysis of non-canonical fibroblast growth factor receptor 1 (FGFR1) interaction reveals regulatory and activating domains of neurofascin. *J. Biol. Chem.* 284, 28533–28542.
- Klapal, L., Igelhorst, B.A., and Dietzel-Meyer, I.D. (2016). Changes in Neuronal Excitability by Activated Microglia: Differential Na⁺ Current Upregulation in Pyramid-Shaped and Bipolar Neurons by TNF- α and IL-18. *Neurotrauma* 44.
- Kobayashi, T., Storrie, B., Simons, K., and Dotti, C.G. (1992). A functional barrier to movement of lipids in polarized neurons. *Nature* 359, 647–650.
- Kole, M.H.P., and Stuart, G.J. (2012a). Signal processing in the axon initial segment. *Neuron* 73, 235–247.
- Kole, M.H.P., and Stuart, G.J. (2012b). Signal Processing in the Axon Initial Segment. *Neuron* 73, 235–247.
- Kole, M.H.P., Letzkus, J.J., and Stuart, G.J. (2007). Axon initial segment Kv1 channels control axonal action potential waveform and synaptic efficacy. *Neuron* 55, 633–647.
- Kole, M.H.P., Ilschner, S.U., Kampa, B.M., Williams, S.R., Ruben, P.C., and Stuart, G.J. (2008). Action potential generation requires a high sodium channel density in the axon initial segment. *Nat. Neurosci.* 11, 178–186.
- Koticha, D., Babiarz, J., Kane-Goldsmith, N., Jacob, J., Raju, K., and Grumet, M. (2005). Cell adhesion and neurite outgrowth are promoted by neurofascin NF155 and inhibited by NF186. *Mol. Cell. Neurosci.* 30, 137–148.
- Krämer-Albers, E.-M., Bretz, N., Tenzer, S., Winterstein, C., Möbius, W., Berger, H., Nave, K.-A., Schild, H., and Trotter, J. (2007). Oligodendrocytes secrete exosomes containing major myelin and stress-protective proteins: Trophic support for axons? *Proteomics Clin. Appl.* 1, 1446–1461.
- Kriebel, M., Wuchter, J., Trinks, S., and Volkmer, H. (2012). Neurofascin: A switch between neuronal plasticity and stability. *Int. J. Biochem. Cell Biol.* 44, 694–697.
- Kuba, H., Ishii, T.M., and Ohmori, H. (2006). Axonal site of spike initiation enhances auditory coincidence detection. *Nature* 444, 1069–1072.
- Kuba, H., Oichi, Y., and Ohmori, H. (2010). Presynaptic activity regulates Na(+) channel distribution at the axon initial segment. *Nature* 465, 1075–1078.

- Kuba, H., Adachi, R., and Ohmori, H. (2014). Activity-Dependent and Activity-Independent Development of the Axon Initial Segment. *J. Neurosci.* *34*, 3443–3453.
- Kuba, H., Yamada, R., Ishiguro, G., and Adachi, R. (2015a). Redistribution of Kv1 and Kv7 enhances neuronal excitability during structural axon initial segment plasticity. *Nat. Commun.* *6*, 8815.
- Kuba, H., Yamada, R., Ishiguro, G., and Adachi, R. (2015b). Redistribution of Kv1 and Kv7 enhances neuronal excitability during structural axon initial segment plasticity. *Nat. Commun.* *6*, 8815.
- Kuba Hiroshi, and Ohmori Harunori (2009). Roles of axonal sodium channels in precise auditory time coding at nucleus magnocellularis of the chick. *J. Physiol.* *587*, 87–100.
- Kumar, A., Barrett, J.P., Alvarez-Croda, D.-M., Stoica, B.A., Faden, A.I., and Loane, D.J. (2016). NOX2 drives M1-like microglial/macrophage activation and neurodegeneration following experimental traumatic brain injury. *Brain. Behav. Immun.* *58*, 291–309.
- Kumar, A., Barrett, J.P., Alvarez-Croda, D.-M., Stoica, B.A., Faden, A.I., and Loane, D.J. NOX2 drives M1-like microglial/macrophage activation and neurodegeneration following experimental traumatic brain injury. *Brain. Behav. Immun.*
- Labasque, M., Devaux, J.J., Lévêque, C., and Faivre-Sarrailh, C. (2011). Fibronectin type III-like domains of neurofascin-186 protein mediate gliomedin binding and its clustering at the developing nodes of Ranvier. *J. Biol. Chem.* *286*, 42426–42434.
- Labasque, M., Hivert, B., Nogales-Gadea, G., Querol, L., Illa, I., and Faivre-Sarrailh, C. (2014). Specific Contactin N-Glycans Are Implicated in Neurofascin Binding and Autoimmune Targeting in Peripheral Neuropathies. *J. Biol. Chem.* *289*, 7907–7918.
- Lambert, S., Davis, J.Q., and Bennett, V. (1997). Morphogenesis of the node of Ranvier: co-clusters of ankyrin and ankyrin-binding integral proteins define early developmental intermediates. *J. Neurosci. Off. J. Soc. Neurosci.* *17*, 7025–7036.
- Lappe-Siefke, C., Goebbels, S., Gravel, M., Nicksch, E., Lee, J., Braun, P.E., Griffiths, I.R., and Nave, K.-A. (2003). Disruption of *Cnp1* uncouples oligodendroglial functions in axonal support and myelination. *Nat. Genet.* *33*, 366–374.
- Lee, Y., Morrison, B.M., Li, Y., Lengacher, S., Farah, M.H., Hoffman, P.N., Liu, Y., Tsingalia, A., Jin, L., Zhang, P.-W., et al. (2012). Oligodendroglia metabolically support axons and contribute to neurodegeneration. *Nature* *487*, 443–448.
- Leterrier, C., Potier, J., Caillol, G., Debarnot, C., Rueda Boroni, F., and Dargent, B. (2015). Nanoscale Architecture of the Axon Initial Segment Reveals an Organized and Robust Scaffold. *Cell Rep.* *13*, 2781–2793.

- Li, Y., Du, X.-F., Liu, C.-S., Wen, Z.-L., and Du, J.-L. (2012). Reciprocal regulation between resting microglial dynamics and neuronal activity in vivo. *Dev. Cell* 23, 1189–1202.
- Liu, H., Focia, P.J., and He, X. (2011). Homophilic adhesion mechanism of neurofascin, a member of the L1 family of neural cell adhesion molecules. *J. Biol. Chem.* 286, 797–805.
- Livak, K.J., and Schmittgen, T.D. (2001). Analysis of relative gene expression data using real-time quantitative PCR and the 2(-Delta Delta C(T)) Method. *Methods San Diego Calif* 25, 402–408.
- Lonigro, A., and Devaux, J.J. (2009). Disruption of neurofascin and gliomedin at nodes of Ranvier precedes demyelination in experimental allergic neuritis. *Brain J. Neurol.* 132, 260–273.
- Lunnon, K., Smith, R., Hannon, E., De Jager, P.L., Srivastava, G., Volta, M., Troakes, C., Al-Sarraj, S., Burrage, J., Macdonald, R., et al. (2014). Methylomic profiling implicates cortical deregulation of *ANK1* in Alzheimer's disease. *Nat. Neurosci.* 17, 1164–1170.
- Lustig, M., Zanazzi, G., Sakurai, T., Blanco, C., Levinson, S.R., Lambert, S., Grumet, M., and Salzer, J.L. (2001). Nr-CAM and neurofascin interactions regulate ankyrin G and sodium channel clustering at the node of Ranvier. *Curr. Biol.* 11, 1864–1869.
- Ma, F., Liu, F., Ding, L., You, M., Yue, H., Zhou, Y., and Hou, Y. (2017). Anti-inflammatory effects of curcumin are associated with down regulating microRNA-155 in LPS-treated macrophages and mice. *Pharm. Biol.* 55, 1263–1273.
- Maier, O., van der Heide, T., van Dam, A.-M., Baron, W., de Vries, H., and Hoekstra, D. (2005). Alteration of the extracellular matrix interferes with raft association of neurofascin in oligodendrocytes. Potential significance for multiple sclerosis? *Mol. Cell. Neurosci.* 28, 390–401.
- Maness, P.F., and Schachner, M. (2007). Neural recognition molecules of the immunoglobulin superfamily: signaling transducers of axon guidance and neuronal migration. *Nat. Neurosci.* 10, 19–26.
- Marin, M.A., Ziburkus, J., Jankowsky, J., and Rasband, M.N. (2016). Amyloid- β plaques disrupt axon initial segments. *Exp. Neurol.* 281, 93–98.
- Mastroeni, D., Sekar, S., Nolz, J., Delvaux, E., Lunnon, K., Mill, J., Liang, W.S., and Coleman, P.D. (2017). *ANK1* is up-regulated in laser captured microglia in Alzheimer's brain; the importance of addressing cellular heterogeneity. *PLOS ONE* 12, e0177814.
- Matsebatlela, T.M., Anderson, A.L., Gallicchio, V.S., Elford, H., and Rice, C.D. (2015). 3,4-Dihydroxy-benzohydroxamic acid (Didox) suppresses pro-inflammatory profiles and

oxidative stress in TLR4-activated RAW264.7 murine macrophages. *Chem. Biol. Interact.* 233, 95–105.

Mayhew, C.N., Mampururu, L.J., Chendil, D., Ahmed, M.M., Phillips, J.D., Greenberg, R.N., Elford, H.L., and Gallicchio, V.S. (2002). Suppression of retrovirus-induced immunodeficiency disease (murine AIDS) by trimidox and didox: Novel ribonucleotide reductase inhibitors with less bone marrow toxicity than hydroxyurea. *Antiviral Res.* 56, 167–181.

McEwen, D.P., and Isom, L.L. (2004). Heterophilic interactions of sodium channel beta1 subunits with axonal and glial cell adhesion molecules. *J. Biol. Chem.* 279, 52744–52752.

Mensch, S., Baraban, M., Almeida, R., Czopka, T., Ausborn, J., El Manira, A., and Lyons, D.A. (2015). Synaptic vesicle release regulates myelin sheath number of individual oligodendrocytes in vivo. *Nat. Neurosci.* 18, 628–630.

Milner, R., and Campbell, I.L. (2003). The extracellular matrix and cytokines regulate microglial integrin expression and activation. *J. Immunol. Baltim. Md 1950* 170, 3850–3858.

Mitew, S., Gobijs, I., Fenlon, L.R., McDougall, S.J., Hawkes, D., Xing, Y.L., Bujalka, H., Gundlach, A.L., Richards, L.J., Kilpatrick, T.J., et al. (2018). Pharmacogenetic stimulation of neuronal activity increases myelination in an axon-specific manner. *Nat. Commun.* 9.

Miyamoto, A., Wake, H., Ishikawa, A.W., Eto, K., Shibata, K., Murakoshi, H., Koizumi, S., Moorhouse, A.J., Yoshimura, Y., and Nabekura, J. (2016). Microglia contact induces synapse formation in developing somatosensory cortex. *Nat. Commun.* 7, 12540.

Montgomery, A.M., Becker, J.C., Siu, C.H., Lemmon, V.P., Cheresh, D.A., Pancook, J.D., Zhao, X., and Reisfeld, R.A. (1996). Human neural cell adhesion molecule L1 and rat homologue NILE are ligands for integrin alpha v beta 3. *J. Cell Biol.* 132, 475–485.

Morgan, M.J., and Liu, Z. (2011). Crosstalk of reactive oxygen species and NF- κ B signaling. *Cell Res.* 21, 103–115.

Mori, S., Wu, C.-Y., Yamaji, S., Saegusa, J., Shi, B., Ma, Z., Kuwabara, Y., Lam, K.S., Isseroff, R.R., Takada, Y.K., et al. (2008). Direct Binding of Integrin α v β 3 to FGF1 Plays a Role in FGF1 Signaling. *J. Biol. Chem.* 283, 18066–18075.

Mossakowski, A.A., Pohlan, J., Bremer, D., Lindquist, R., Millward, J.M., Bock, M., Pollok, K., Mothes, R., Viohl, L., Radbruch, M., et al. (2015). Tracking CNS and systemic sources of oxidative stress during the course of chronic neuroinflammation. *Acta Neuropathol. (Berl.)* 130, 799–814.

Mouton, P.R. (2013). *Neurostereology: Unbiased Stereology of Neural Systems* (John Wiley & Sons).

Muir, J., and Kittler, J.T. (2014). Plasticity of GABAA receptor diffusion dynamics at the axon initial segment. *Front. Cell. Neurosci.* 8, 151.

Nakada, C., Ritchie, K., Oba, Y., Nakamura, M., Hotta, Y., Iino, R., Kasai, R.S., Yamaguchi, K., Fujiwara, T., and Kusumi, A. (2003). Accumulation of anchored proteins forms membrane diffusion barriers during neuronal polarization. *Nat. Cell Biol.* 5, 626–632.

Nayernia, Z., Jaquet, V., and Krause, K.-H. (2014). New insights on NOX enzymes in the central nervous system. *Antioxid. Redox Signal.* 20, 2815–2837.

Nelson, A.D., and Jenkins, P.M. (2017). Axonal Membranes and Their Domains: Assembly and Function of the Axon Initial Segment and Node of Ranvier. *Front. Cell. Neurosci.* 11, 136.

Nimmerjahn, A., Kirchhoff, F., and Helmchen, F. (2005). Resting microglial cells are highly dynamic surveillants of brain parenchyma in vivo. *Science* 308, 1314–1318.

Ogawa, Y., and Rasband, M.N. (2008). The functional organization and assembly of the axon initial segment. *Curr. Opin. Neurobiol.* 18, 307–313.

Ogawa, Y., Schafer, D.P., Horresh, I., Bar, V., Hales, K., Yang, Y., Susuki, K., Peles, E., Stankewich, M.C., and Rasband, M.N. (2006). Spectrins and AnkyrinB Constitute a Specialized Paranodal Cytoskeleton. *J. Neurosci.* 26, 5230–5239.

Ohl, K., Tenbrock, K., and Kipp, M. (2016). Oxidative stress in multiple sclerosis: Central and peripheral mode of action. *Exp. Neurol.* 277, 58–67.

Okazaki, N., Kikuno, R., Ohara, R., Inamoto, S., Koseki, H., Hiraoka, S., Saga, Y., Nagase, T., Ohara, O., and Koga, H. (2003). Prediction of the coding sequences of mouse homologues of KIAA gene: III. the complete nucleotide sequences of 500 mouse KIAA-homologous cDNAs identified by screening of terminal sequences of cDNA clones randomly sampled from size-fractionated libraries. *DNA Res. Int. J. Rapid Publ. Rep. Genes Genomes* 10, 167–180.

Otsu, N. (1979). A Threshold Selection Method from Gray-Level Histograms. *IEEE Transactions on Systems, Man, and Cybernetics* 9, 62–66.

Pacharra, S., Hanisch, F.-G., and Breloy, I. (2012). Neurofascin 186 Is O-Mannosylated within and Outside of the Mucin Domain. *J. Proteome Res.* 11, 3955–3964.

Palay, S.L., Sotelo, C., Peters, A., and Orkand, P.M. (1968). The axon hillock and the initial segment. *J. Cell Biol.* 38, 193–201.

Palmer, L.M., and Stuart, G.J. (2006). Site of action potential initiation in layer 5 pyramidal neurons. *J. Neurosci. Off. J. Soc. Neurosci.* 26, 1854–1863.

- Pan, Z., Kao, T., Horvath, Z., Lemos, J., Sul, J.-Y., Cranstoun, S.D., Bennett, V., Scherer, S.S., and Cooper, E.C. (2006). A Common Ankyrin-G-Based Mechanism Retains KCNQ and NaV Channels at Electrically Active Domains of the Axon. *J. Neurosci.* 26, 2599–2613.
- Paolicelli, R.C., Bolasco, G., Pagani, F., Maggi, L., Scianni, M., Panzanelli, P., Giustetto, M., Ferreira, T.A., Guiducci, E., Dumas, L., et al. (2011). Synaptic pruning by microglia is necessary for normal brain development. *Science* 333, 1456–1458.
- Pawate, S., Shen, Q., Fan, F., and Bhat, N.R. (2004). Redox regulation of glial inflammatory response to lipopolysaccharide and interferon- γ . *J. Neurosci. Res.* 77, 540–551.
- Pellerin, L., Bouzier-Sore, A.-K., Aubert, A., Serres, S., Merle, M., Costalat, R., and Magistretti, P.J. (2007). Activity-dependent regulation of energy metabolism by astrocytes: an update. *Glia* 55, 1251–1262.
- Peng, T.-I., and Jou, M.-J. (2010). Oxidative stress caused by mitochondrial calcium overload. *Ann. N. Y. Acad. Sci.* 1201, 183–188.
- Pillai, A.M., Thaxton, C., Pribisko, A.L., Cheng, J.-G., Dupree, J.L., and Bhat, M.A. (2009). Spatiotemporal ablation of myelinating glia-specific neurofascin (Nfasc NF155) in mice reveals gradual loss of paranodal axoglial junctions and concomitant disorganization of axonal domains. *J. Neurosci. Res.* 87, 1773–1793.
- Pollock, J.D., Williams, D.A., Gifford, M.A., Li, L.L., Du, X., Fisherman, J., Orkin, S.H., Doerschuk, C.M., and Dinauer, M.C. (1995). Mouse model of X-linked chronic granulomatous disease, an inherited defect in phagocyte superoxide production. *Nat. Genet.* 9, 202–209.
- Pomicter, A.D., Shroff, S.M., Fuss, B., Sato-Bigbee, C., Brophy, P.J., Rasband, M.N., Bhat, M.A., and Dupree, J.L. (2010). Novel forms of neurofascin 155 in the central nervous system: alterations in paranodal disruption models and multiple sclerosis. *Brain J. Neurol.* 133, 389–405.
- Prinz, M., Tay, T.L., Wolf, Y., and Jung, S. (2014). Microglia: unique and common features with other tissue macrophages. *Acta Neuropathol. (Berl.)* 128, 319–331.
- Pruss, T., Niere, M., Kranz, E.U., and Volkmer, H. (2004). Homophilic interactions of chick neurofascin in trans are important for neurite induction. *Eur. J. Neurosci.* 20, 3184–3188.
- Qin, L., Liu, Y., Wang, T., Wei, S.-J., Block, M.L., Wilson, B., Liu, B., and Hong, J.-S. (2004). NADPH oxidase mediates lipopolysaccharide-induced neurotoxicity and proinflammatory gene expression in activated microglia. *J. Biol. Chem.* 279, 1415–1421.

- Qin, L., Wu, X., Block, M.L., Liu, Y., Breese, G.R., Hong, J.-S., Knapp, D.J., and Crews, F.T. (2007). Systemic LPS causes chronic neuroinflammation and progressive neurodegeneration. *Glia* 55, 453–462.
- Qin, L., Liu, Y., Hong, J.-S., and Crews, F.T. (2013). NADPH oxidase and aging drive microglial activation, oxidative stress, and dopaminergic neurodegeneration following systemic LPS administration. *Glia* 61, 855–868.
- Ransohoff, R.M., and Khoury, J.E. (2016). Microglia in Health and Disease. *Cold Spring Harb. Perspect. Biol.* 8, a020560.
- Ransohoff, R.M., and Perry, V.H. (2009). Microglial physiology: unique stimuli, specialized responses. *Annu. Rev. Immunol.* 27, 119–145.
- Rasband, M.N. (2010). The axon initial segment and the maintenance of neuronal polarity. *Nat. Rev. Neurosci.* 11, 552–562.
- Rasband, M.N., and Peles, E. (2015). The Nodes of Ranvier: Molecular Assembly and Maintenance. *Cold Spring Harb. Perspect. Biol.* 8, a020495.
- Rasband, M.N., Tayler, J., Kaga, Y., Yang, Y., Lappe-Siefke, C., Nave, K.-A., and Bansal, R. (2005). CNP is required for maintenance of axon-glia interactions at nodes of Ranvier in the CNS. *Glia* 50, 86–90.
- Ratcliffe, C.F., Westenbroek, R.E., Curtis, R., and Catterall, W.A. (2001). Sodium channel beta1 and beta3 subunits associate with neurofascin through their extracellular immunoglobulin-like domain. *J. Cell Biol.* 154, 427–434.
- Rathjen, F.G., Wolff, J.M., Chang, S., Bonhoeffer, F., and Raper, J.A. (1987). Neurofascin: a novel chick cell-surface glycoprotein involved in neurite-neurite interactions. *Cell* 51, 841–849.
- Ren, Q., and Bennett, V. (1998). Palmitoylation of neurofascin at a site in the membrane-spanning domain highly conserved among the L1 family of cell adhesion molecules. *J. Neurochem.* 70, 1839–1849.
- Rogers, J.T., Morganti, J.M., Bachstetter, A.D., Hudson, C.E., Peters, M.M., Grimmig, B.A., Weeber, E.J., Bickford, P.C., and Gemma, C. (2011). CX3CR1 deficiency leads to impairment of hippocampal cognitive function and synaptic plasticity. *J. Neurosci. Off. J. Soc. Neurosci.* 31, 16241–16250.
- Ruppert, M., Aigner, S., Hubbe, M., Yagita, H., and Altevogt, P. (1995). The L1 adhesion molecule is a cellular ligand for VLA-5. *J. Cell Biol.* 131, 1881–1891.
- Russo, M.V., and McGavern, D.B. (2016). Inflammatory neuroprotection following traumatic brain injury. *Science* 353, 783–785.

- Salter, M.W., and Stevens, B. (2017). Microglia emerge as central players in brain disease. *Nat. Med.* 23, 1018–1027.
- Salton, S.R., Shelanski, M.L., and Greene, L.A. (1983). Biochemical properties of the nerve growth factor-inducible large external (NILE) glycoprotein. *J. Neurosci. Off. J. Soc. Neurosci.* 3, 2420–2430.
- Santello, M., Cali, C., and Bezzi, P. (2012). Gliotransmission and the tripartite synapse. *Adv. Exp. Med. Biol.* 970, 307–331.
- Schafer, D.P., and Stevens, B. (2013). Phagocytic glial cells: sculpting synaptic circuits in the developing nervous system. *Curr. Opin. Neurobiol.* 23, 1034–1040.
- Schafer, D.P., Jha, S., Liu, F., Akella, T., McCullough, L.D., and Rasband, M.N. (2009). Disruption of the axon initial segment cytoskeleton is a new mechanism for neuronal injury. *J. Neurosci. Off. J. Soc. Neurosci.* 29, 13242–13254.
- Schafer, D.P., Lehrman, E.K., Kautzman, A.G., Koyama, R., Mardinly, A.R., Yamasaki, R., Ransohoff, R.M., Greenberg, M.E., Barres, B.A., and Stevens, B. (2012). Microglia sculpt postnatal neural circuits in an activity and complement-dependent manner. *Neuron* 74, 691–705.
- Schousboe, A., Scafidi, S., Bak, L.K., Waagepetersen, H.S., and McKenna, M.C. (2014). Glutamate metabolism in the brain focusing on astrocytes. *Adv. Neurobiol.* 11, 13–30.
- Schürmann, G., Haspel, J., Grumet, M., and Erickson, H.P. (2001). Cell Adhesion Molecule L1 in Folded (Horseshoe) and Extended Conformations. *Mol. Biol. Cell* 12, 1765–1773.
- Shah, K.N., Wilson, E.A., Malla, R., Elford, H.L., and Faridi, J.S. (2015). Targeting Ribonucleotide Reductase M2 and NF- κ B Activation with Didox to Circumvent Tamoxifen Resistance in Breast Cancer. *Mol. Cancer Ther.* 14, 2411–2421.
- Sherman, D.L., Tait, S., Melrose, S., Johnson, R., Zonta, B., Court, F.A., Macklin, W.B., Meek, S., Smith, A.J.H., Cottrell, D.F., et al. (2005). Neurofascins are required to establish axonal domains for saltatory conduction. *Neuron* 48, 737–742.
- Shu, Y., Yu, Y., Yang, J., and McCormick, D.A. (2007). Selective control of cortical axonal spikes by a slowly inactivating K⁺ current. *Proc. Natl. Acad. Sci. U. S. A.* 104, 11453–11458.
- Sierra, A., Abiega, O., Shahraz, A., and Neumann, H. (2013). Janus-faced microglia: beneficial and detrimental consequences of microglial phagocytosis. *Front. Cell. Neurosci.* 7, 6.
- Sierra, A., Tremblay, M.-E., and Wake, H. (2015). Never-resting microglia: physiological roles in the healthy brain and pathological implications (Frontiers E-books).

Silletti, S., Yebra, M., Perez, B., Cirulli, V., McMahon, M., and Montgomery, A.M.P. (2004). Extracellular signal-regulated kinase (ERK)-dependent gene expression contributes to L1 cell adhesion molecule-dependent motility and invasion. *J. Biol. Chem.* *279*, 28880–28888.

Smith, A.W., Das, A., Guyton, M.K., Ray, S.K., Rohrer, B., and Banik, N.L. (2011). Calpain Inhibition Attenuates Apoptosis of Retinal Ganglion Cells in Acute Optic Neuritis. *Invest. Ophthalmol. Vis. Sci.* *52*, 4935–4941.

Sohn, P.D., Tracy, T.E., Son, H.-I., Zhou, Y., Leite, R.E.P., Miller, B.L., Seeley, W.W., Grinberg, L.T., and Gan, L. (2016). Acetylated tau destabilizes the cytoskeleton in the axon initial segment and is mislocalized to the somatodendritic compartment. *Mol. Neurodegener.* *11*, 47.

Song, A.-H., Wang, D., Chen, G., Li, Y., Luo, J., Duan, S., and Poo, M.-M. (2009). A selective filter for cytoplasmic transport at the axon initial segment. *Cell* *136*, 1148–1160.

Squarzoni, P., Oller, G., Hoeffel, G., Pont-Lezica, L., Rostaing, P., Low, D., Bessis, A., Ginhoux, F., and Garel, S. (2014). Microglia Modulate Wiring of the Embryonic Forebrain. *Cell Rep.* *8*, 1271–1279.

Stallcup, W.B., and Beasley, L. (1985). Polymorphism among NILE-related glycoproteins from different types of neurons. *Brain Res.* *346*, 287–293.

Stellwagen, D., and Malenka, R.C. (2006). Synaptic scaling mediated by glial TNF- α . *Nature* *440*, 1054–1059.

Stoler, O., and Fleidervish, I.A. (2016). Functional implications of axon initial segment cytoskeletal disruption in stroke. *Acta Pharmacol. Sin.* *37*, 75–81.

Strausberg, R.L., Feingold, E.A., Grouse, L.H., Derge, J.G., Klausner, R.D., Collins, F.S., Wagner, L., Shenmen, C.M., Schuler, G.D., Altschul, S.F., et al. (2002). Generation and initial analysis of more than 15,000 full-length human and mouse cDNA sequences. *Proc. Natl. Acad. Sci. U. S. A.* *99*, 16899–16903.

Susuki, K., Chang, K.-J., Zollinger, D.R., Liu, Y., Ogawa, Y., Eshed-Eisenbach, Y., Dours-Zimmermann, M.T., Oses-Prieto, J.A., Burlingame, A.L., Seidenbecher, C.I., et al. (2013). Three mechanisms assemble central nervous system nodes of Ranvier. *Neuron* *78*, 469–482.

Taetzsch, T., Levesque, S., McGraw, C., Brookins, S., Luqa, R., Bonini, M.G., Mason, R.P., Oh, U., and Block, M.L. (2015). Redox regulation of NF- κ B p50 and M1 polarization in microglia. *Glia* *63*, 423–440.

Tait, S., Gunn-Moore, F., Collinson, J.M., Huang, J., Lubetzki, C., Pedraza, L., Sherman, D.L., Colman, D.R., and Brophy, P.J. (2000). An oligodendrocyte cell

adhesion molecule at the site of assembly of the paranodal axo-glial junction. *J. Cell Biol.* 150, 657–666.

Takano, T., Tian, G.-F., Peng, W., Lou, N., Libionka, W., Han, X., and Nedergaard, M. (2006). Astrocyte-mediated control of cerebral blood flow. *Nat. Neurosci.* 9, 260–267.

Tay, T.L., Savage, J.C., Hui, C.W., Bisht, K., and Tremblay, M.-È. (2017). Microglia across the lifespan: from origin to function in brain development, plasticity and cognition. *J. Physiol.* 595, 1929–1945.

Thaxton, C., Pillai, A.M., Pribisko, A.L., Labasque, M., Dupree, J.L., Faivre-Sarrailh, C., and Bhat, M.A. (2010). In vivo deletion of immunoglobulin domains 5 and 6 in neurofascin (Nfasc) reveals domain-specific requirements in myelinated axons. *J. Neurosci. Off. J. Soc. Neurosci.* 30, 4868–4876.

Thaxton, C., Pillai, A.M., Pribisko, A.L., Dupree, J.L., and Bhat, M.A. (2011). Nodes of Ranvier Act as Barriers to Restrict Invasion of Flanking Paranodal Domains in Myelinated Axons. *Neuron* 69, 244–257.

Thelen, K., Kedar, V., Panicker, A.K., Schmid, R.-S., Midkiff, B.R., and Maness, P.F. (2002). The neural cell adhesion molecule L1 potentiates integrin-dependent cell migration to extracellular matrix proteins. *J. Neurosci. Off. J. Soc. Neurosci.* 22, 4918–4931.

Trager, N., Smith, A., Wallace IV, G., Azuma, M., Inoue, J., Beeson, C., Haque, A., and Banik, N.L. (2014). Effects of a novel orally administered calpain inhibitor SNJ-1945 on immunomodulation and neurodegeneration in a murine model of multiple sclerosis. *J. Neurochem.* 130, 268–279.

Trapp, B.D., Wujek, J.R., Criste, G.A., Jalabi, W., Yin, X., Kidd, G.J., Stohlman, S., and Ransohoff, R. (2007). Evidence for synaptic stripping by cortical microglia. *Glia* 55, 360–368.

Tremblay, M.-È., Lowery, R.L., and Majewska, A.K. (2010). Microglial Interactions with Synapses Are Modulated by Visual Experience. *PLoS Biol* 8, e1000527.

Tremblay, M.-È., Stevens, B., Sierra, A., Wake, H., Bessis, A., and Nimmerjahn, A. (2011). The Role of Microglia in the Healthy Brain. *J. Neurosci.* 31, 16064–16069.

Turchan, J., Pocernich, C.B., Gairola, C., Chauhan, A., Schifitto, G., Butterfield, D.A., Buch, S., Narayan, O., Sinai, A., Geiger, J., et al. (2003). Oxidative stress in HIV demented patients and protection ex vivo with novel antioxidants. *Neurology* 60, 307–314.

Tuvia, S., Garver, T.D., and Bennett, V. (1997). The phosphorylation state of the FIGQY tyrosine of neurofascin determines ankyrin-binding activity and patterns of cell segregation. *Proc. Natl. Acad. Sci. U. S. A.* 94, 12957–12962.

- Van Wart, A., Trimmer, J.S., and Matthews, G. (2007). Polarized distribution of ion channels within microdomains of the axon initial segment. *J. Comp. Neurol.* *500*, 339–352.
- Vascak, M., Sun, J., Baer, M., Jacobs, K.M., and Povlishock, J.T. (2017). Mild Traumatic Brain Injury Evokes Pyramidal Neuron Axon Initial Segment Plasticity and Diffuse Presynaptic Inhibitory Terminal Loss. *Front. Cell. Neurosci.* *11*, 157.
- Volkmer, H., Hassel, B., Wolff, J.M., Frank, R., and Rathjen, F.G. (1992). Structure of the axonal surface recognition molecule neurofascin and its relationship to a neural subgroup of the immunoglobulin superfamily. *J. Cell Biol.* *118*, 149–161.
- Volkmer, H., Leuschner, R., Zacharias, U., and Rathjen, F.G. (1996). Neurofascin induces neurites by heterophilic interactions with axonal NrCAM while NrCAM requires F11 on the axonal surface to extend neurites. *J. Cell Biol.* *135*, 1059–1069.
- Volkmer, H., Zacharias, U., Nörenberg, U., and Rathjen, F.G. (1998). Dissection of complex molecular interactions of neurofascin with axonin-1, F11, and tenascin-R, which promote attachment and neurite formation of tectal cells. *J. Cell Biol.* *142*, 1083–1093.
- Wake, H., Moorhouse, A.J., Jinno, S., Kohsaka, S., and Nabekura, J. (2009). Resting microglia directly monitor the functional state of synapses in vivo and determine the fate of ischemic terminals. *J. Neurosci. Off. J. Soc. Neurosci.* *29*, 3974–3980.
- Wallraff, A., Köhling, R., Heinemann, U., Theis, M., Willecke, K., and Steinhäuser, C. (2006). The impact of astrocytic gap junctional coupling on potassium buffering in the hippocampus. *J. Neurosci. Off. J. Soc. Neurosci.* *26*, 5438–5447.
- Wang, X., Pinto-Duarte, A., Sejnowski, T.J., and Behrens, M.M. (2013a). How Nox2-containing NADPH oxidase affects cortical circuits in the NMDA receptor antagonist model of schizophrenia. *Antioxid. Redox Signal.* *18*, 1444–1462.
- Wang, Z., Wei, X., Liu, K., Zhang, X., Yang, F., Zhang, H., He, Y., Zhu, T., Li, F., Shi, W., et al. (2013b). NOX2 deficiency ameliorates cerebral injury through reduction of complexin II-mediated glutamate excitotoxicity in experimental stroke. *Free Radic. Biol. Med.* *65*, 942–951.
- Warren, H.S., Fitting, C., Hoff, E., Adib-Conquy, M., Beasley-Topliffe, L., Tesini, B., Liang, X., Valentine, C., Hellman, J., Hayden, D., et al. (2010). Resilience to bacterial infection: difference between species could be due to proteins in serum. *J. Infect. Dis.* *201*, 223–232.
- Wefelmeyer, W., Cattaert, D., and Burrone, J. (2015). Activity-dependent mismatch between axo-axonic synapses and the axon initial segment controls neuronal output. *Proc. Natl. Acad. Sci. U. S. A.* *112*, 9757–9762.

Wefelmeyer, W., Puhl, C.J., and Burrone, J. (2016). Homeostatic Plasticity of Subcellular Neuronal Structures: From Inputs to Outputs. *Trends Neurosci.* 39, 656–667.

Wehage, E., Eisfeld, J., Heiner, I., Jüngling, E., Zitt, C., and Lückhoff, A. (2002). Activation of the cation channel long transient receptor potential channel 2 (LTRPC2) by hydrogen peroxide. A splice variant reveals a mode of activation independent of ADP-ribose. *J. Biol. Chem.* 277, 23150–23156.

Wei, C.H., and Ryu, S.E. (2012). Homophilic interaction of the L1 family of cell adhesion molecules. *Exp. Mol. Med.* 44, 413–423.

Wilkins, A., Majed, H., Layfield, R., Compston, A., and Chandran, S. (2003). Oligodendrocytes promote neuronal survival and axonal length by distinct intracellular mechanisms: a novel role for oligodendrocyte-derived glial cell line-derived neurotrophic factor. *J. Neurosci. Off. J. Soc. Neurosci.* 23, 4967–4974.

Wolf, S.A., Boddeke, H.W.G.M., and Kettenmann, H. (2017). Microglia in Physiology and Disease. *Annu. Rev. Physiol.* 79, 619–643.

Wong, W.T. (2013). Microglial aging in the healthy CNS: phenotypes, drivers, and rejuvenation. *Front. Cell. Neurosci.* 7, 22.

Xu, K., and Terakawa, S. (1999). Fenestration nodes and the wide submyelinic space form the basis for the unusually fast impulse conduction of shrimp myelinated axons. *J. Exp. Biol.* 202, 1979–1989.

Yamada, R., and Kuba, H. (2016). Structural and Functional Plasticity at the Axon Initial Segment. *Front. Cell. Neurosci.* 10.

Yamasaki, R., Lu, H., Butovsky, O., Ohno, N., Rietsch, A.M., Cialic, R., Wu, P.M., Doykan, C.E., Lin, J., Cotleur, A.C., et al. (2014). Differential roles of microglia and monocytes in the inflamed central nervous system. *J. Exp. Med.* 211, 1533–1549.

Yang, Y., Ogawa, Y., Hedstrom, K.L., and Rasband, M.N. (2007). betaIV spectrin is recruited to axon initial segments and nodes of Ranvier by ankyrinG. *J. Cell Biol.* 176, 509–519.

Ye, J., Coulouris, G., Zaretskaya, I., Cutcutache, I., Rozen, S., and Madden, T.L. (2012). Primer-BLAST: a tool to design target-specific primers for polymerase chain reaction. *BMC Bioinformatics* 13, 134.

Yin, L., Rasch, M.J., He, Q., Wu, S., Dou, F., and Shu, Y. (2017). Selective Modulation of Axonal Sodium Channel Subtypes by 5-HT_{1A} Receptor in Cortical Pyramidal Neuron. *Cereb. Cortex N. Y. N 1991* 27, 509–521.

Yip, P.M., Zhao, X., Montgomery, A.M., and Siu, C.H. (1998). The Arg-Gly-Asp motif in the cell adhesion molecule L1 promotes neurite outgrowth via interaction with the α 5 β 3 integrin. *Mol. Biol. Cell* 9, 277–290.

Yona, S., Kim, K.-W., Wolf, Y., Mildner, A., Varol, D., Breker, M., Strauss-Ayali, D., Viukov, S., Williams, M., Misharin, A., et al. (2013). Fate mapping reveals origins and dynamics of monocytes and tissue macrophages under homeostasis. *Immunity* 38, 79–91.

Yoshimura, T., and Rasband, M.N. (2014). Axon initial segments: diverse and dynamic neuronal compartments. *Curr. Opin. Neurobiol.* 27, 96–102.

Zhan, Y., Paolicelli, R.C., Sforzini, F., Weinhard, L., Bolasco, G., Pagani, F., Vyssotski, A.L., Bifone, A., Gozzi, A., Ragozzino, D., et al. (2014). Deficient neuron-microglia signaling results in impaired functional brain connectivity and social behavior. *Nat. Neurosci.* 17, 400–406.

Zhang, A., Desmazieres, A., Zonta, B., Melrose, S., Campbell, G., Mahad, D., Li, Q., Sherman, D.L., Reynolds, R., and Brophy, P.J. (2015). Neurofascin 140 is an embryonic neuronal neurofascin isoform that promotes the assembly of the node of Ranvier. *J. Neurosci. Off. J. Soc. Neurosci.* 35, 2246–2254.

Zhang, C., Hou, L., Yang, J., Che, Y., Sun, F., Li, H., and Wang, Q. (2018). 2,5-Hexanedione induces dopaminergic neurodegeneration through integrin α 5 β 2/NADPH oxidase axis-mediated microglial activation. *Cell Death Dis.* 9, 60.

Zhang, X., Davis, J.Q., Carpenter, S., and Bennett, V. (1998). Structural requirements for association of neurofascin with ankyrin. *J. Biol. Chem.* 273, 30785–30794.

Zhou, D., Lambert, S., Malen, P.L., Carpenter, S., Boland, L.M., and Bennett, V. (1998). AnkyrinG is required for clustering of voltage-gated Na channels at axon initial segments and for normal action potential firing. *J. Cell Biol.* 143, 1295–1304.

Zonta, B., Tait, S., Melrose, S., Anderson, H., Harroch, S., Higginson, J., Sherman, D.L., and Brophy, P.J. (2008). Glial and neuronal isoforms of Neurofascin have distinct roles in the assembly of nodes of Ranvier in the central nervous system. *J. Cell Biol.* 181, 1169–1177.

Zonta, M., Angulo, M.C., Gobbo, S., Rosengarten, B., Hossmann, K.-A., Pozzan, T., and Carmignoto, G. (2003). Neuron-to-astrocyte signaling is central to the dynamic control of brain microcirculation. *Nat. Neurosci.* 6, 43–50.

VITA

Savannah (Brookins) Benusa was born in Lancaster, CA in March 1990 and was raised in Lone Oak, Texas. She graduated from Lone Oak High School in 2008. Savannah continued her education at Texas A&M University in Commerce, Texas, where she received a Bachelor of Science in Biological Sciences in 2012. In the Fall of 2012, Savannah entered the Neuroscience program at Virginia Commonwealth University and joined the laboratory of Michelle Block, PhD in the Department of Anatomy and Neurobiology in the Spring of 2013. In the laboratory of Dr. Block, she investigated the combined effects of peripheral infection and pesticide exposure in the pathogenesis of Gulf War Illness. In the Summer of 2014, Dr. Block relocated to Indiana University and Savannah joined the laboratory of Jeff Dupree, PhD where she investigated the role that inflammation plays in disrupting axon initial segment stability. Savannah completed her neuroscience graduate training under the mentorship of Jeff Dupree, PhD.